System identification and seismic analysis of a residential RC building in Kathmandu, Nepal

Rajan Dhakal

Faculty of Civil Engineering
University of Iceland
2020

System identification and seismic analysis of a residential RC building in Kathmandu, Nepal

Rajan Dhakal

30 ECTS thesis submitted in partial fulfillment of a
Magister Scientiarum degree in Civil Engineering

MS Committee
Rajesh Rupakhety
Dipendra Gautam
Said Elias Rahimi

Master's Examiner
Sigurbjörn Bárðarson

Faculty of Civil Engineering
School of Engineering and Natural Sciences
University of Iceland
Reykjavik, February 2020

System identification and seismic analysis of residential RC building in Kathmandu, Nepal
30 ECTS thesis submitted in partial fulfillment of a *Magister Scientiarum* degree in Civil Engineering

Faculty of Civil Engineering
School of Engineering and Natural Sciences
University of Iceland
Hjarðarhagi 6
107, Reykjavik
Iceland

Telephone: 525 4000

Bibliographic information:
Rajan Dhakal, 2020, *System identification and seismic analysis of a residential RC building in Kathmandu, Nepal*, Master's thesis, Faculty of civil Engineering, University of Iceland

Printing: Háskólaprent
Reykjavik, Iceland, February 2020

Abstract

This study focuses on experimental system identification, numerical modelling and seismic analysis of an existing reinforced concrete frame building located in Kathmandu, Nepal. System identification is performed with basic theoretical background along with brief introduction to different methods. Demonstrations of the different methods are depicted using response simulated from known simple single degree of freedom (SDOF) and multi degree of freedom (MDOF) systems which are then used for system identification. As a case study, system identification of a four-storied reinforced concrete building located in Kathmandu, Nepal is considered. Two methods of system identification techniques--Welch spectral method and N4SID method--are used for estimation of modal properties. The estimated natural periods of the building are 0.264s and 0.266s for the two fundamental modes of vibration in the two principal directions. The corresponding damping ratios are estimated to be 6.3% and 6.9%. Finite element models with and without soil flexibility are created on ETABS 2017 to study overall differences in the model properties compared to results from system identification. The estimated natural periods are 0.226s and 0.207s for model with rigid soil and 0.275s and 0.259s for model with flexible soil for the first two fundamental modes of vibration in the two principal directions. Study finds that the natural periods of the structure, estimated by finite element model, significantly depend on supporting conditions. When the structure is assumed to be built on rigid soil, the estimated vibration periods are lower than those identified from ambient vibration. While, estimated natural periods for model with flexible soil support are very close to those identified from ambient vibration. This shows the importance of modelling soil flexibility for accurate dynamic characterization of buildings using finite element model.

Seismic analysis of the building was conducted with strong ground motion recorded during the 25 April 2015 Gorkha Earthquake. Along with recorded ground motion, peak ground acceleration (PGA) scaled elastic response spectra from Eurocode 8 and Indian standards IS 1893 (part 1): 2002 are used for analysis. The structural response of the building with brick infills in terms of base shear, story drift, and structural integrity are checked. The result shows that base shear demand from ground motion is met by code specified response spectra at soft site. However, base shear demand at rock site is considerably higher than that from the soft sites which is underestimated by code specified spectra. Similarly, drift ratio analysis shows that the drift demand when considering soft site ground motion is well within the recommended limits. However, the drift ratio caused by the ground motion recorded at stiff site is two time higher than that depicted by ground motion recorded at soft soil site. Structural verification of selected cross sections was performed using moment curvature diagram (for beam) and P-M interaction diagram (for column). Result of this checking shows that some of the columns on structure were overstressed while the beams performed well during the 25 April Gorkha Earthquake although the ground shaking was not intense.

Table of contents

List of Figures

List of Tables

Acknowledgements

It is a pleasure, delight and happiness to show gratefulness to individual who contributed to this thesis.

First, I would like to acknowledge University of Iceland for providing the opportunity to carry out this study as partial fulfilment of the requirement of master´s program.

I am obliged to my supervisor Prof. Rajesh Rupakhety for his guidance and valuable suggestions as well as continuous advice, encouragement and inspiration throughout the whole study.

I am very thankful to Mr. Dipendra Gautam who helped me to set up instrument and record data from Nepal, and also helped by reading and editing the thesis. I also thank the owner of the case-study building, Mrs. Pragya Acharya Dhakal, for allowing us to install the instrument in her house to collect data used in this thesis. I would like to acknowledge Sunrise Homes (p) Ltd., Nepal, for providing the SPT test results.

I also want to express my gratitude to Dr. Said Elias for valuable recommendations on the thesis.

I am thankful to the examiner, Mr. Sigurbjörn Bárðarson, for taking the time to read and examine my thesis, and for his valuable comments and suggestions for improvement.

My sincere gratitude goes to my parents for supporting my education and for their unconditional love an encouragement. I dedicate this thesis to them.

1 Introduction

1.1 Background

Civil engineering structures are susceptible to dynamic loads. Environmental actions such as earthquake and strong winds induce damage and that can accumulate over time and make structure more vulnerable to future environmental actions. Also, repeated actions on the structure leads to fatigue failure. Consequences of failure of civil engineering structures such as buildings and bridges are extremely high. Identification of such damages while they are not visible from outside is important for timely remedial actions against such disasters. Structural system identification and health monitoring is therefore a very important and growing field of research in civil engineering.

Structural health monitoring (SHM) relies on vibration measurements to detect and identify changes in dynamic properties of a structure. System Identification or experimental modal analysis is a mathematical framework to identify dynamic properties of a structure (or a system) from measured vibration and potentially excitation forces. SHM is a broad field which consists of several methods such as visual inspections, destructive testing, ultrasonic testing, etc. System identification using vibration measurement at different times can reveal potential damage accumulation in the structure manifested in the form of change in its dynamic properties. This method has specific advantages over the other methods; they are non-destructive and able to identify damage that are invisible. Moreover, structure can remain operational during the test which itself can be installed as a continuous system. Also, no artificial excitation is needed, for example ambient vibration from traffic or wind loading can be used as system excitation to record system response. System identification based on response only without any consideration of the excitation is known as blind system identification.

Apart from experimental methods, numerical modelling of structure such as finite element model is a popular tool to estimate system parameters. Finite element modelling based on mechanical properties and geometry of the structural systems can be used to estimate modal parameters of system. Reliability of the numerical results depends on assumption made to create model. There are several uncertainties involved in such modelling, for example in material properties, rigidity of connections, conditions of the soil supporting the foundation, etc., which introduce simplifying assumptions and engineering judgements in finite element modelling. These uncertainties translate to uncertainties in the estimated dynamic behavior of the structure. In addition, as the structure ages, its dynamic properties change. If the structure is subjected to strong loading or repeated moderate loading, it can lose part of its stiffness, which results in change of its dynamic behavior. System identification can be used to identify such changes and calibrate/update finite element models of the structure, which can then be used for analyzing its safety and/or designing retrofitting schemes.

1.2 Aims and objectives

The main objectives of this study are the following.

1. To explore the theoretical background of structural system identification using ambient vibration measurement.

2. To estimate modal parameters of an existing structure using ambient vibration measurements.

3. To construct and update a finite element model of the building.

5. To study the seismic performance of the calibrated model.

1.3 Research methodology

The research methodology used in this study comprises both theoretical and experimental. The theoretical aspects are related to different methods of system identification which includes parametric and non-parametric methods. The other theoretical aspects are related to finite element analysis of a building structure. In this aspect of study, creating a three-dimensional finite element model of the building structure being studied is created. This theoretical model is used for modal and dynamic response analysis using strong ground motions. Modal analysis includes estimation of natural frequencies and mode shapes of the structure. The experimental method used in this study relies on the case study of residential building located in Kathmandu, Nepal. Ambient vibration records measured at different stories of the case study building are used for structural system identification. The results obtained from experimental system identification method and those obtained from theoretical finite element model are compared and used to update the finite element model.

1.4 Organization of the thesis

This thesis is divided into the following seven chapters

Chapter 1: This chapter introduces work done in this thesis

Chapter 2: This chapter presents different mathematical models of system identification. Their practical application is illustrated using single degree of freedom (SDOF) and multi degree of freedom (MDOF) systems.

Chapter 3: This chapter deals with the case study of this thesis. It introduces the studied building, its structural system along with mechanical properties of different elements and topics related to soil-structure interaction.

Chapter 4: This chapter presents the results of system identification of the case study building.

Chapter 5: This chapter comprises numerical modelling of the case study building using finite element program ETABS 2017.

Chapter 6: This chapter presents earthquake analysis of the case study building

Chapter 7: This chapter contains the main findings and conclusions deducted from the results.

2 System Identification

2.1 Introduction

System identification in structural dynamics refers to estimation of dynamic characteristics of structure based on known excitation and response. In other words, structural identification is a process to estimate the dynamic properties of a structure based on measured response to known excitation. The main dynamic characteristics that can be estimated using methods of system identification are mode shapes, natural frequencies, damping ratios and participation factors. Dynamic structural properties such as natural frequencies and damping ratio are important parameters for structural assessment of the building. **Error! Not a valid bookmark self-reference.** illustrates system identification process schematically.

.

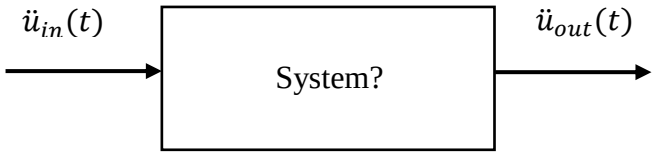

Figure 2.1 Schematic of the system identification problem.

There are mainly two classes of mathematical models for system identification; parametric methods and non-parametric methods. Both the methods are described in following sections with illustration of some popular models. To illustrate the application of various models described below, a single degree of freedom (SDOF) system is considered. The system is assigned a natural vibration period and damping ratio of 1sec and 5%, respectively. The system is excited by a white noise used as ground acceleration. Figure 2.2 shows acceleration time history used as a white noise excitation. The simulated response is then used in different system identification models to back calculate the properties of the system.

2.2 Non-parametric methods

On this method resulting models are represented visually using curves or characterized by weighting functions. Such functions are not given with finite-dimensional parameter vector. Hence, visual comparisons and curve fitting technique are often used. The system properties are calculated from the fitted curves. Popular mathematical models for non-parametric method of system identification are described in the following sub chapters.

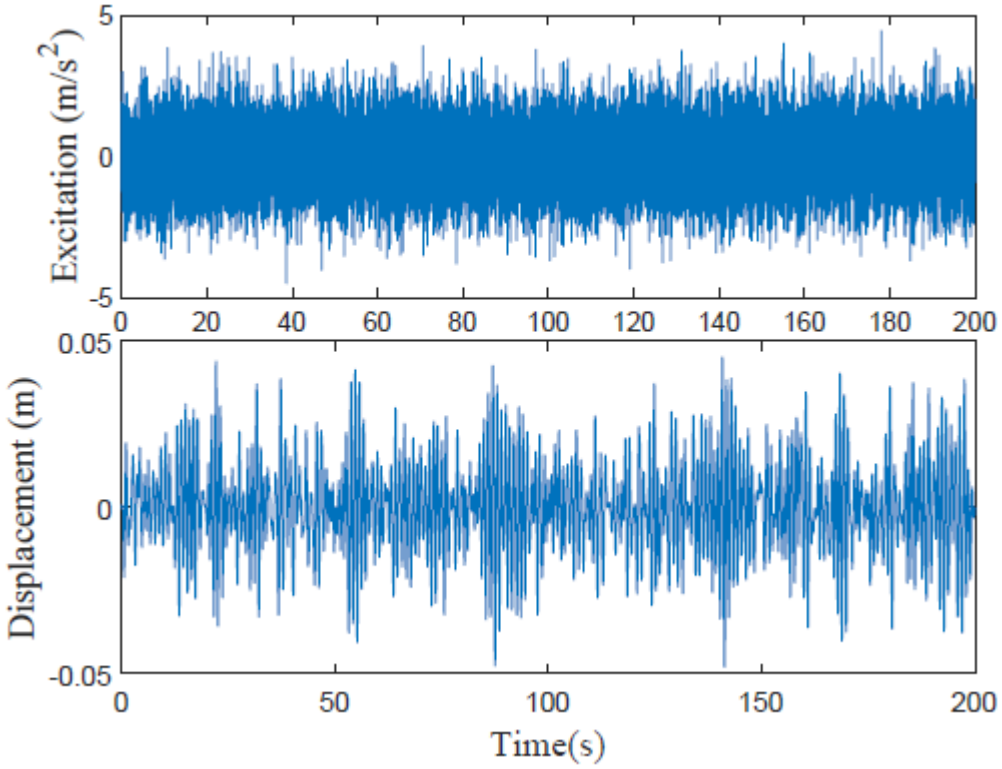

Figure 2.2 White noise as excitation and simulated displacement response of a SDOF system with vibration period of 1s and damping ratio of 5%.

2.2.1 Transient analysis

This method relies on estimation of unit impulse response function of the structure. Natural period of vibration and damping ratio are then estimated from the unit impulse response function. Response function oscillates with the frequency of the SDOF system and period of vibration of the system can therefore be computed by counting the time between two distinct peaks. Similarly, damping ratio can be estimated using exponential decay of unit impulse response function.

2.2.2 Correlation analysis

In this method, modal response equation is used to find the unit impulse response function. To do this correlation between the corresponding modal response and the measured output are maximized. Once unit impulse response function is known system can be identified using transient analysis.

2.2.3 Spectral analysis

Spectral analysis is done in frequency domain. The input excitation and the output response are transformed to frequency domain using Fourier transform. Fourier transform of input excitation and output response for discrete time signals can be written as:

$$Y_N(\omega) = \sum_{k=1}^{N} y(k)e^{-ik\omega} \tag{2.1}$$

$$U_N(\omega) = \sum_{k=1}^{N} u(k)e^{-ik\omega} \tag{2.2}$$

Where,

y(k) is the response of the system

u(k) is the excitation to the system

$Y_N(\omega)$ and $U_N(\omega)$ are the Fourier transformations of the output and input respectively

For SDOF system an empirical estimate of complex frequency response function, $H(\omega)$ can be obtained as,

$$\hat{H}(\omega) = \frac{Y_N(\omega)}{U_N(\omega)} \tag{2.3}$$

This function can be transformed back to time domain using inverse Fourier transformation to obtain an estimate of unit impulse response function. Once, unit impulse response function is known, the system can be identified using transient analysis. However, estimated $\hat{H}(\omega)$ can also be used directly for system identification. The natural frequencies can be obtained from the plot of squared amplitude of the complex frequency response function by picking the peaks. It is notable that, for system with small damping values, up to 10% of the critical damping, the peak of the plot occurs close to the natural frequency of the system. The frequencies and most of the power of the response gets concentrated in a narrow band of the frequency around peak frequency. If the damping ratio of the system is higher, the peak lies away from the natural frequency of the system and the power spectrum becomes wider. Response of a lightly damped structure excited with white noise process can be modelled as a narrow band process. For narrow band process the critical damping ratio is estimated from the half power point method, which is based on the following equations (Papagiannopoulos and Hatzigeorgiou 2011) ,

$$\xi = \frac{\omega_2 - \omega_1}{2\omega_n} = \frac{f_2 - f_1}{2f_n} \tag{2.4}$$

$$\Delta f = f_2 - f_1 = 2\xi f_n \tag{2.5}$$

Where, Δf is the half-power bandwidth defined in the frequency band where the power density of the response reduces to half its value. f_1 and f_2 are frequencies at corners of half power and f_n is the frequency where power density is maximum and is approximately equal to the undamped natural frequency of lightly damped systems. This method is straightforward when power spectral density function contains one peak. This can be observed on lightly damped SDOF systems. For MDOF systems, multiple peaks can be observed. The peaks near the frequencies of different natural modes of the structure. When

the natural frequencies of the structure are closely spaced, it becomes difficult to identify clear peaks on the power spectral density of the response.

Figure 2.3 shows the normalized (by the maximum amplitude) squared amplitude of the complex frequency response function of the SDOF system being considered here. When the excitation is a white noise process, the squared amplitude of the complex frequency response function is the power spectral density function of the response scaled by a constant. Half-power level is represented by red dashed line in the figure. The frequency associated with the peak represents the natural frequency of the system. The estimated parameters are,

Natural period of the system, T = 0.999sec.

Critical damping ratio, ξ = 4.92%

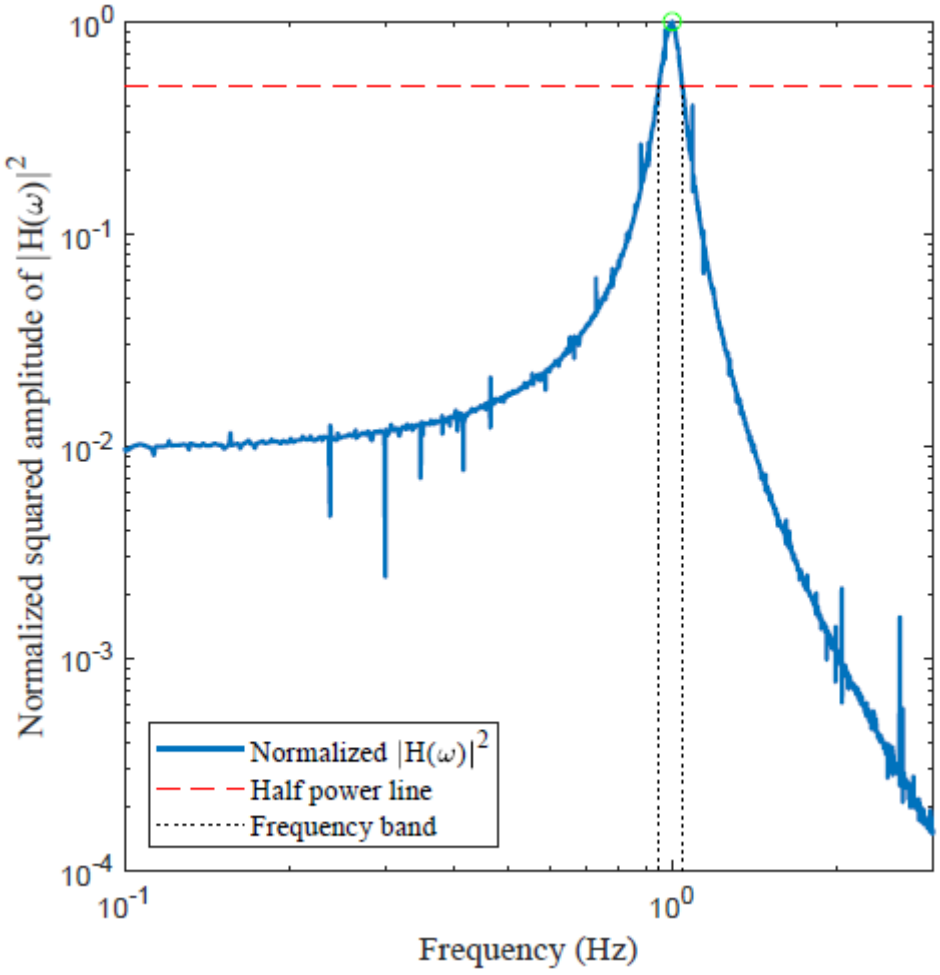

Figure 2.3 Normalized squared amplitude of the complex frequency function, $|H(w)|^2$ for SDOF system using spectral method.

The results suggest identified parameters are close to the actual system parameters. The accuracy of the results depends upon various parameters like number of data samples, frequency resolution and bandwidth of the signal. This result was based on the Fourier transform. Since this is a simulated response, it lacks noise commonly associated with

measured response. When measured response and the excitation can be approximated as a white noise, the squared amplitude of complex frequency response function can be obtained from the power spectral density (PSD) of the measured response. Periodogram estimates of the PSD are associated with high variances, which can be reduced by smoothing. Several smoothing algorithms are available, among which, the Welch's averaged periodogram is very popular.

In this method the measured signals are divided up into many overlapping segments. The overlapping segments are windowed and periodogram estimates of the different segments are averaged to estimate the PSD. Figure 2.4 shows the plot of PSD of input excitation and simulated displacement response of SDOF system using Welch´s method.

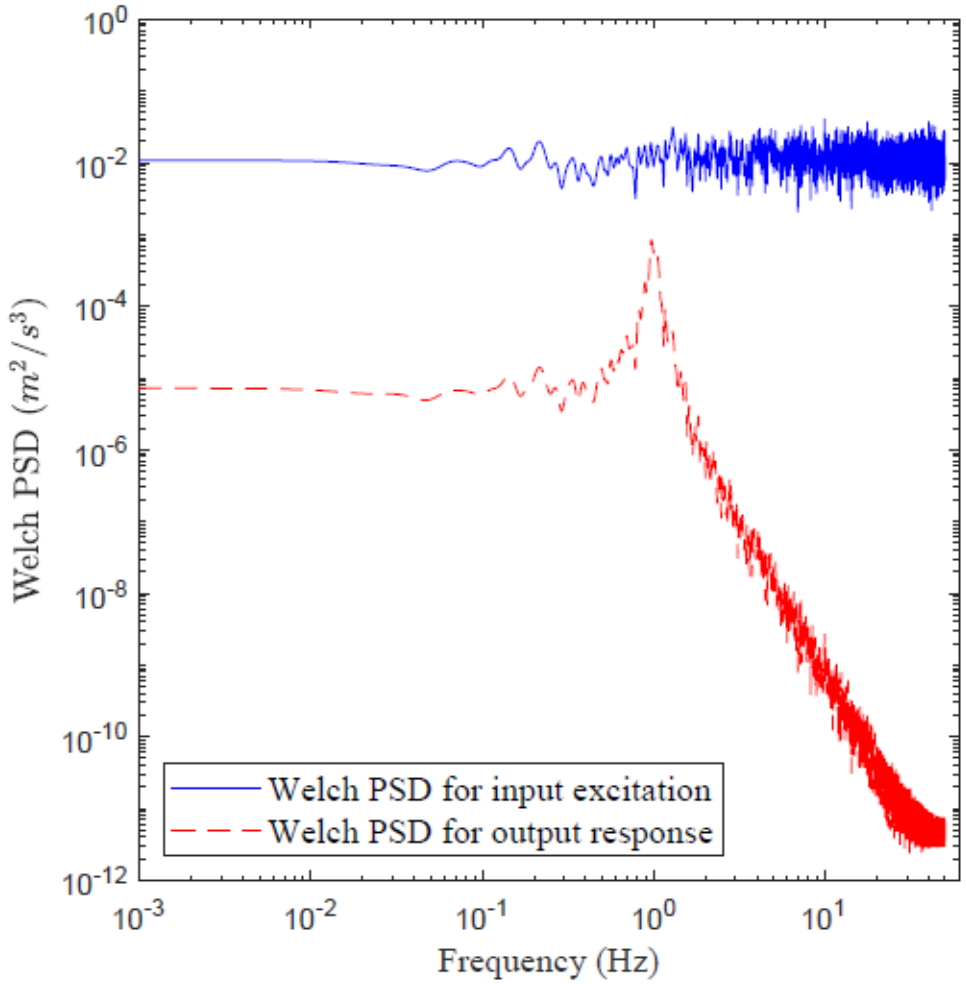

Figure 2.4 Welch PSD for input excitation and output response of the SDOF system.

Figure 2.5 shows the plot of normalized PSD using Welch´s method. Also, normalized squared amplitude of theoretical complex frequency response function $|H(\omega)|^2$ is plotted in the figure. The theoretical complex frequency function of a SDOF system is given by equation 2.6.

$$H(\Omega) = \frac{1}{-\Omega^2 m + i\Omega c + k} \tag{2.6}$$

where, m, c, and k, are the mass, damping coefficient, and stiffness of the system and i is the imaginary unit.

The results confirm that the Welch's PSD provides a good approximation of the complex frequency response function of the system. The estimated system parameters using Welch´s PSD are,

Natural period of the system, T= 1.01sec.

Critical damping ratio, ξ= 5.1%

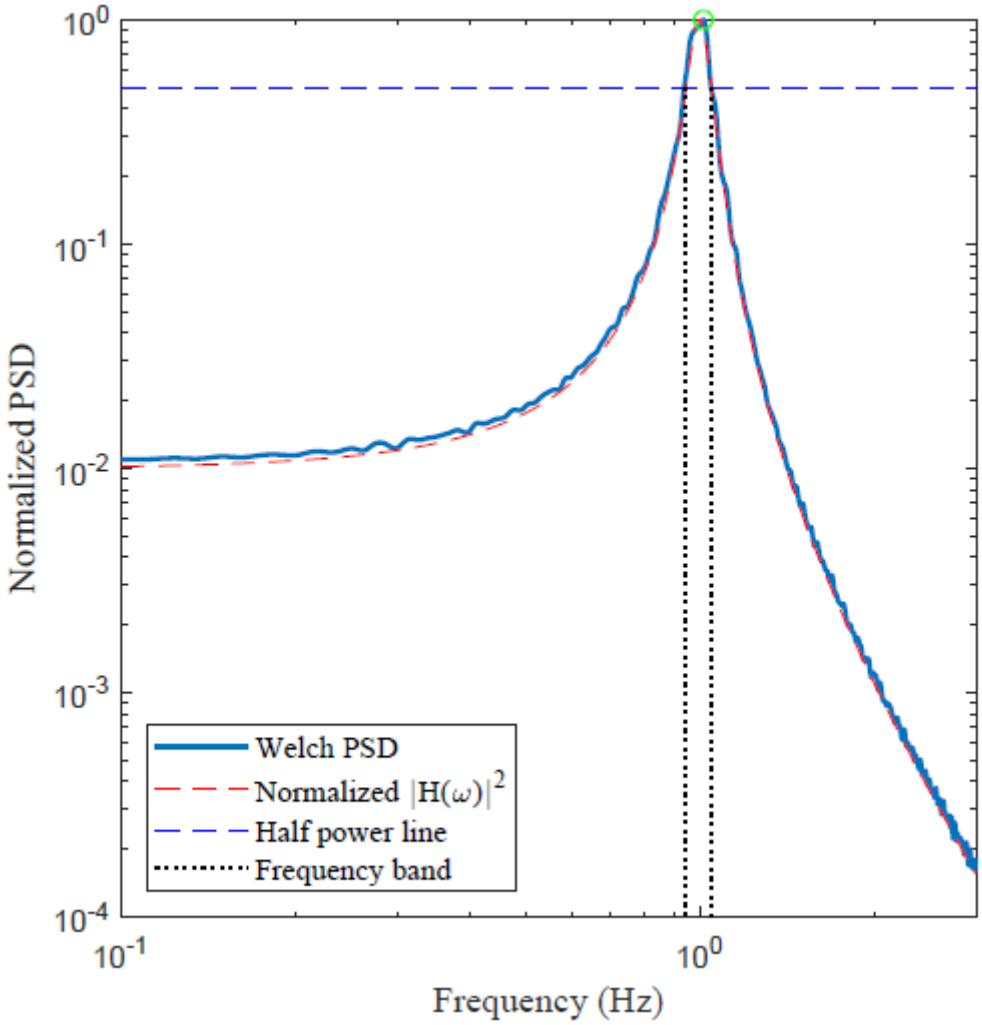

Figure 2.5 Normalized squared amplitude of the complex frequency function, $|H(w)|^2$ and normalized PSD using Welch´s method.

2.3 Parametric methods

This section will introduce some of the popular parametric methods of system identification with the help of SDOF system. Mainly regression models and state-space

model will be discussed here. Additional details can be found in, for example Box et al. (2015) and Jenkins and Watt (1969). Generally, regression models can be represented as,

$$y(t) = \{\phi(t)\}^T \{\theta\} \tag{2.7}$$

Where, y(t) is the output of the system and $\phi(t)$ is a column vector containing measured values at discrete time $t = \Delta k$. Where, Δ is sampling interval and k represents finite integer k=1,2,3.... Similarly, θ represents a column vector containing regression parameters.

2.3.1 ARMA model

Autoregressive moving average or ARMA model is a parametric model of system identification resulting from combination of autoregressive process or AR-model and moving average process or MA-model. AR-models are defined as,

$$e(t) = y(t) + a_1 y(t-1) + a_2 y(t-2) + ... + a_n y(t-n) \tag{2.8}$$

Where, e(t) is the white noise input and t stands for integer values and $\{a_1, a_2, a_{3, ..., } a_n\}$ are unknown regression parameters. Similarly, MA-models are defined as,

$$y(t) = e(t) + c_1 e(t-1) + ... + c_j e(t-j) \tag{2.9}$$

From combination of AR-model and MA-model ARMA model can be written as,

$$y(t) = -a_1 y(t-1) - a_2 y(t-2) - a_n y(t-n) + c_1 e(t-1) + ... + c_j e(t-j) \tag{2.10}$$

When the input is also known, ARMA model of Equation (2.10) can be modified into a ARMAX model. Parameters of these models can be estimated from statistical methods. For example, least squares regression and maximum likelihood methods are popular. More details on these methods are explained in Jenkins and Watt (1969). For this method, apart from the estimation of the model parameters, an analyst needs to decide model order for system. Higher model orders are required for complex systems. However, model order should be parsimonious. In other words, model order should be optimally selected. Various mathematical criteria for example least prediction error method have been developed to help select optimal model order.

To demonstrate the relationship between model parameters and system parameters, an example of SDOF system is as,

$$\ddot{y}(t) + \frac{c}{m}\dot{y}(t) + \frac{k}{m}y(t) = u(t) \tag{2.11}$$

Where y(t) is the displacement response of the system u(t) is the force acting on the system normalized by the mass of the system. Single and double dots over a variable are used for its first and second derivatives respectively. Defining the undamped angular frequency $\omega = \sqrt{\frac{k}{m}}$ and expressing damping coefficient in terms of critical damping ratio ξ as $c=2\xi m\omega$, the equation of motion can be written as

$$\ddot{y}(t) + 2\xi m\omega \dot{y}(t) + \omega^2 y(t) = u(t) \tag{2.12}$$

General solution to the homogeneous part can be written as $y(t) = e^{rt}$, which leads to a characteristics equation with the following roots for underdamped systems

$$\left.\begin{matrix} r1 \\ r2 \end{matrix}\right\} = -\xi\omega \pm i\omega_d \tag{2.13}$$

Where, $\omega_d = \omega\sqrt{1-\xi^2}$

SDOF systems can be described with two system parameters, the damping ratio and frequency. Hence, a second order AR model can be used to describe the free vibration response of the system. For the forced vibration response ARX model would be required.

The second order AR model is given by,

$$y[k] + a_1 y[k-1] + a_2 y[k-2] = e[k] \tag{2.14}$$

The solution to the equation can be found by assuming $y[k] = s^k$, which gives characteristics equation as,

$$s^2 - a_1 s - a_2 = 0 \tag{2.15}$$

The roots of the characteristic's equation are given by

$$\left| \frac{a_1}{2} \pm \sqrt{\frac{a_1^{\,2} + 4a_2}{4}} \right| < 1 \tag{2.16}$$

Let us consider the continuous and discrete time representation of the system response

$$y(t) = e^{rt} \tag{2.17}$$

$$y[k] = s^k = e^{\ln(s)k} \tag{2.18}$$

Assuming that the sampling interval is Δ, and for an integer k, the equivalence of the two-representation reduces to

$$\ln(s)k = rk\Delta \Rightarrow s = e^{r\Delta} \tag{2.19}$$

Furthermore, we have the following equations from Equation 2.15

$$s_1 + s_2 = a_1 \tag{2.20}$$

$$s_1 s_2 = -a_2 \tag{2.21}$$

The parameters of Equation (2.10) can be related to system parameters by combining the above equations, resulting in the following equations.

$$\omega = \frac{1}{\Delta}\sqrt{\frac{\{\ln(-a_2)\}^2}{4} + \left\{\cos^{-1}\left(\frac{a_1}{2\sqrt{-a_2}}\right)\right\}^2} \tag{2.22}$$

$$\xi = \sqrt{\frac{\{\ln(-a_2)\}^2}{\{\ln(-a_2)\}^2 + 4\left\{\cos^{-1}\left(\frac{a_1}{2\sqrt{-a_2}}\right)\right\}^2}} \tag{2.23}$$

Similar equivalence can be established for multiple degree of freedom system (MDOF).

Figure 2.6 shows the plot of predicted displacement response of the assumed SDOF system using ARMA model. The figure also shows the plot of simulated displacement response of the system using Newmark's method. The correlation between the two is 0.999. The estimated system parameters are,

Natural period of the system, T= 0.996sec.

Critical damping ratio, ξ= 4.899%

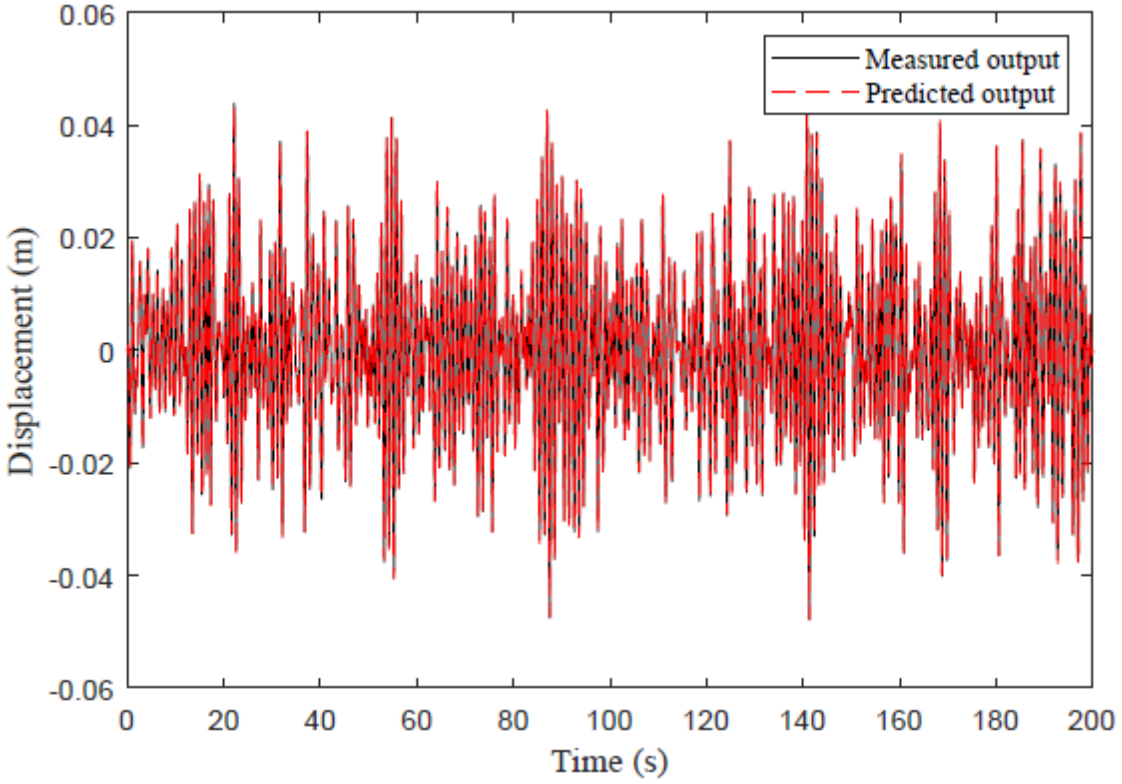

Figure 2.6 Plot of simulated displacement response using Newmark method and predicted displacement response of the system using ARMA model.

2.3.2 N4SID method

N4SID stands for Numerical algorithms for subspace state space system identification. This method is based on mathematical model called state-space model which consist of a set of input, output and state variables linked together by first order differential equations. Following equation represents a state space model in continuous time,

$$\left\{\dot{x}(t)\right\} = [A]\{x(t)\} + \{B\}u(t) \tag{2.24}$$

$$\{y(t)\} = \{C\}\{x(t)\} \tag{2.25}$$

Where, [A] is a parametric system matrix, {B} and {C} are parametric vectors. The vector {x(t)} is called the state of the structure. The number of elements of x(t), n, is called the model order. When state space model ([A], {B} and {C}) is known the model parameters can be identified. During the process the model order n has to be chosen by the analyst. The results obtained are generally sensitive to the selected model order. For assumed SDOF system selected model order is two.

The system parameters estimated using this method are,

Natural period of the system, T= 1.000sec.

Critical damping ratio, ξ= 4.996%

2.4 System Identification of MDOF systems

To illustrate the use of various methods of system identification on MDOF systems an example is taken. A 5-story frame is modelled as shown in Figure 2.7. The lateral stiffness and lumped mass of each story is shown in the figure. Where, m=350kNsec^2/m and k=100000kN/m.

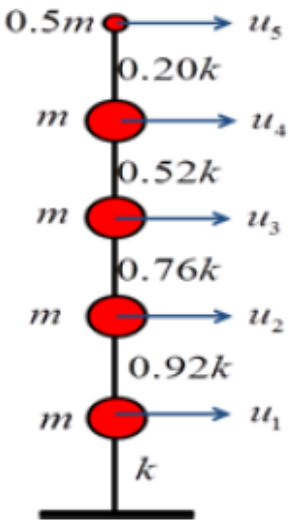

Figure 2.7 A 5-storey frame with masses and stiffness.

The MDOF system has five degrees of freedom as shown in the figure and therefore five modes of natural vibration. For example, floor mass on first floor has one translation degree of freedom and hereafter will be stated as DOF-1 (degree of freedom one). Similarly, for floor mass on second floor as DOF-2 and so on. Steady state vibration at any of those frequencies takes place in the form of special oscillatory shape, known as the corresponding mode shape $\{\phi_n\}$. In other word, $\{\phi_n\}$ represents the deflected shape of the system which does not change with time. Mode shapes of a MDOF system can be obtained by solving eigenvalue or characteristics value problem of free vibration.

To make assumed system more realistic, damping is assigned. It is assumed that damping comes from the structural elements which also contribute to the mass and stiffness to the system. This means, damping can be assumed to be proportional to the mass and stiffness. Such damping model is called Rayleigh damping and can be represented in a matrix form as,

$$[C] = a_0[M] + a_1[K] \tag{2.26}$$

Where a_0 and a_1 are the mass and stiffness proportionality constants. Equation can be solved by specifying the damping ratios and frequencies of any two modes. For assumed system, damping ratios for the first and fifth mode are assumed to be 5% and 7% respectively. Natural frequencies, time periods and Rayleigh damping ratios for MDOF system obtained by solving eigenvalue problem for free vibration can be listed as,

$$w = \begin{bmatrix} 4.780 \\ 10.877 \\ 15.857 \\ 22.114 \\ 28.855 \end{bmatrix} rad/\sec \qquad T = \begin{bmatrix} 1.314 \\ 0.577 \\ 0.396 \\ 0.284 \\ 0.217 \end{bmatrix} \sec \qquad \xi = \begin{bmatrix} 0.050 \\ 0.041 \\ 0.046 \\ 0.057 \\ 0.070 \end{bmatrix}$$

Similarly, mode shapes $\{\phi_n\}$ of the system is,

$$\{\varphi\} = \begin{bmatrix} 1st & 2nd & 3rd & 4th & 5th \\ 0.134 & 0.223 & -0.378 & 0.572 & 0.634 \\ 0.269 & 0.366 & -0.427 & 0.129 & -0.686 \\ 0.404 & 0.339 & 0.007 & -0.698 & 0.345 \\ 0.539 & 0.029 & 0.630 & 0.390 & -0.083 \\ 0.674 & -0.836 & -0.525 & -0.119 & 0.013 \end{bmatrix}$$

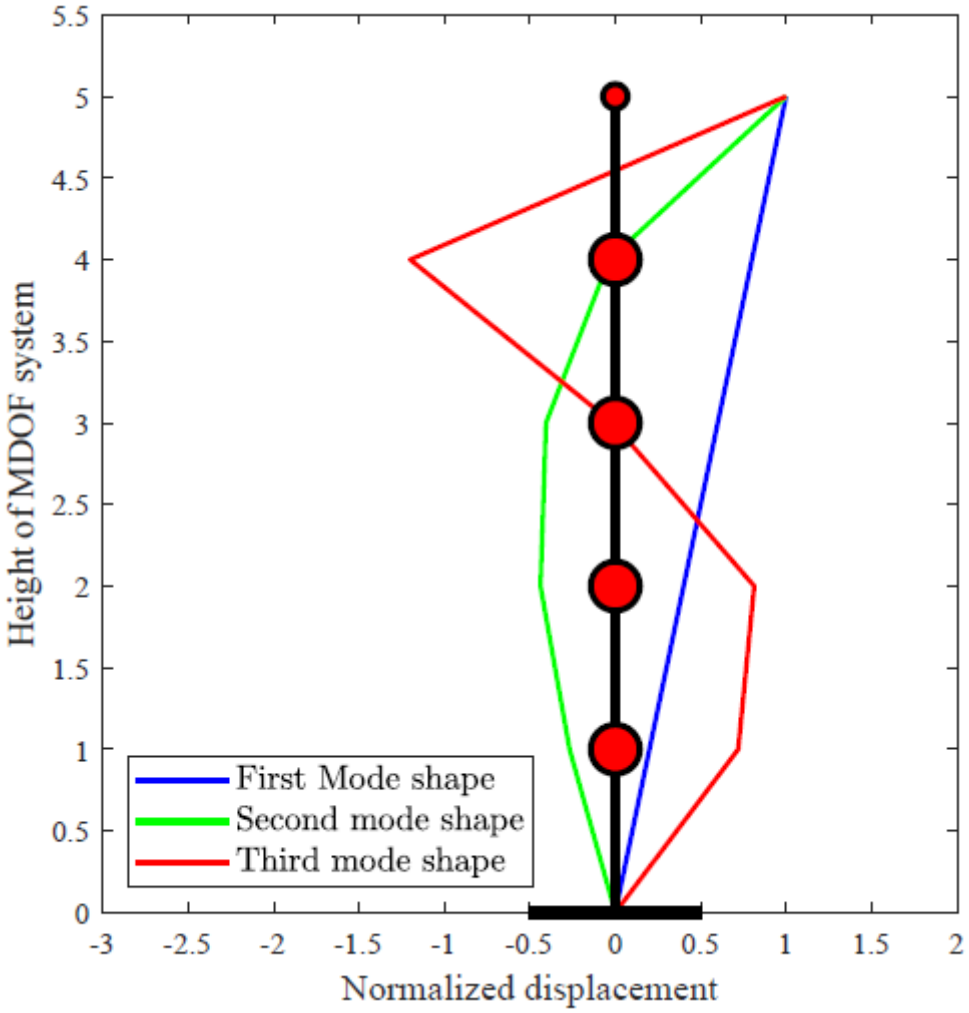

Figure 2.8 Plot of first three mode shapes.

Figure 2.8 shows the plot of first three mode shapes of the MDOF system. The modes shapes are normalized in such a way that the displacement at the roof is equal to 1. It is observed that the displacements of all the floors are in the same direction (right) in the first mode. In the second mode mass at roof has displacement in right direction and first three masses from bottom has displacement in opposite direction. The system is subjected to base acceleration modelled as a white noise and the response of the structure is calculated by using Newmark's integration method. The simulated response is treated as measurements and used in system identification in the following. The excitation and simulated response are shown in Figure 2.9.

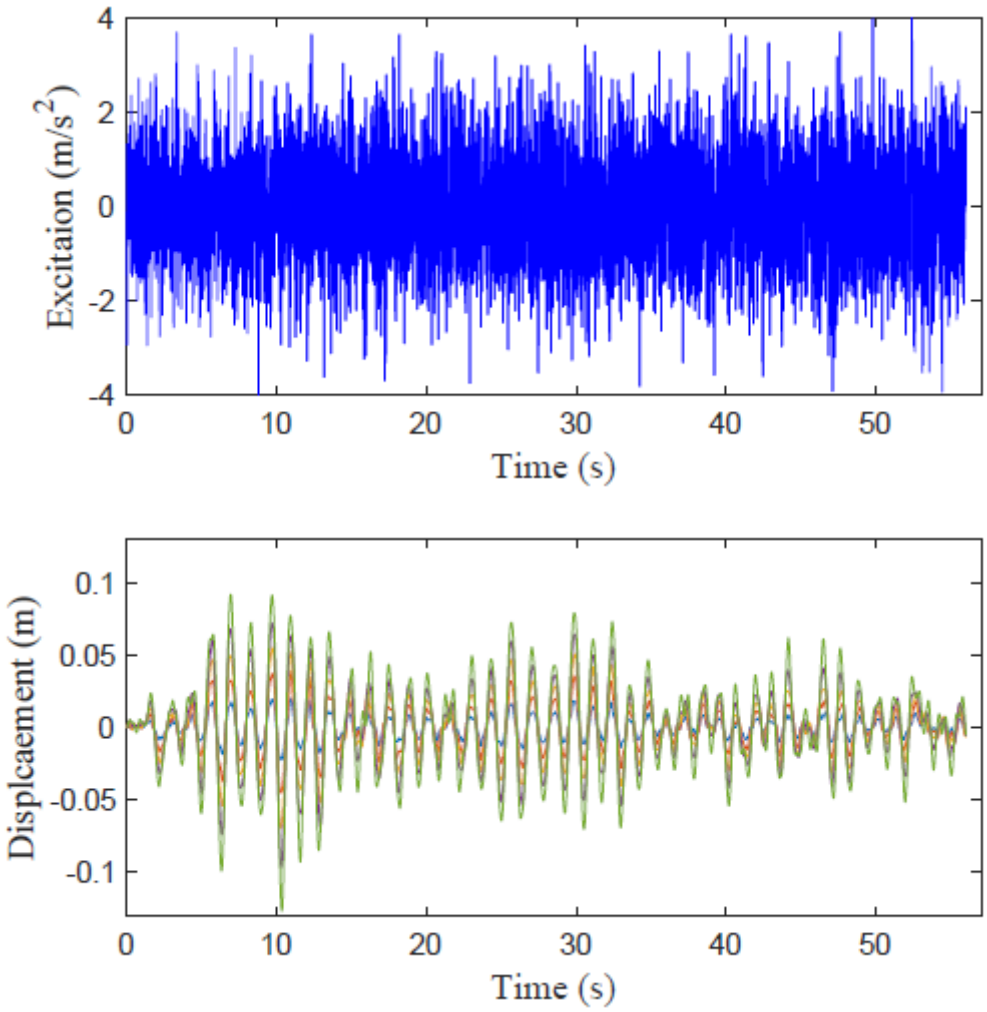

Figure 2.9 White noise as excitation and simulated displacement response (of the 5 masses) of MDOF system calculated using Newmark's integration method.

As explained earlier, in spectral analysis PSD curve consists of several peaks for each mode for MDOF system. Each peak on the curve represents natural frequency of the corresponding mode of the system. If the peaks are spaced closely interference might occur between the peaks which might give inaccurate estimates of the system properties. Figure 2.10 shows the plot of normalized squared amplitude of the complex frequency response function, $|H(w)|^2$ for DOF-5 of MDOF system, estimated from the simulated response. The first peak of this function represents the first mode of the system. The estimated vibration period and damping ratio of the first mode of the system is 1.316s and 4.1% respectively. Similarly, the estimated period of the second mode of vibration is 0.58s.

Similar to the SDOF system, Welch´s algorithm can be used to identify system parameters. Figure 2.11 shows the plot of estimated Welch´s PSD for all five DOFs of the MDOF system. Blue solid line on the figure represents the mean PSD. As explained earlier, frequencies at corners of half power can be used for damping ratio identification. The estimated mean vibration period and damping ratio for first mode are 1.317s and 6.9% respectively. Results obtained from two different methods of spectral analysis shows that the identified vibration periods are very close to that of the actual system. However, the estimated damping ratios are slightly different.

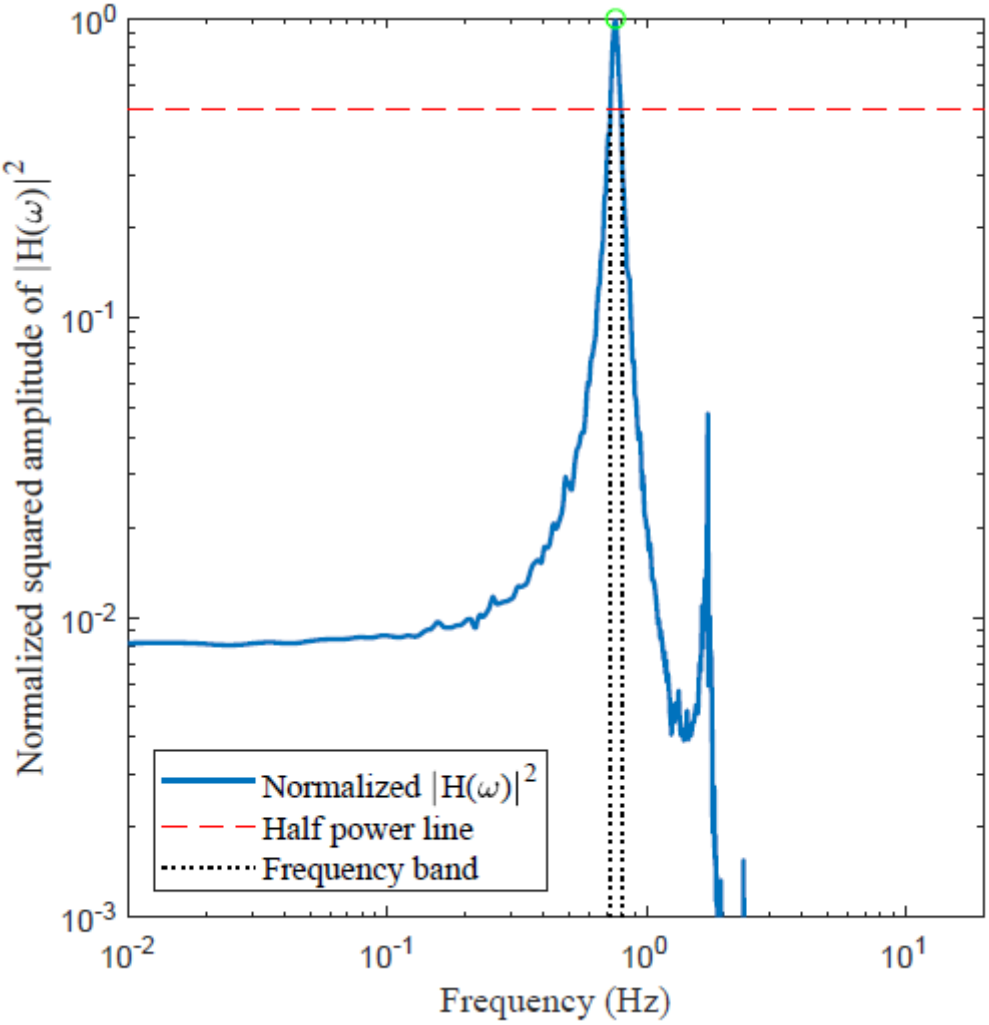

Figure 2.10 Normalized squared amplitude of the complex frequency function, $|H(w)|^2$ for DOF-5 for MDOF system using spectral method.

Similarly, parametric ARMA and N4SID models were used for system identification of the MDOF system. The difference between SDOF systems and MDOF systems lies in selecting a proper higher model order. Since there are two parameters for each mode, time period and damping ratio, the order of the model used must be twice the number of modes. However, this can be lowered if interesting modes are fewer than total numbers of modes. The identified system parameters using both models with actual system parameters are listed on Table 2.1. The identified periods using both models correspond nicely with the actual periods of the system for all modes. Similarly, identified damping ratios match nicely to the actual damping ratios of the system.

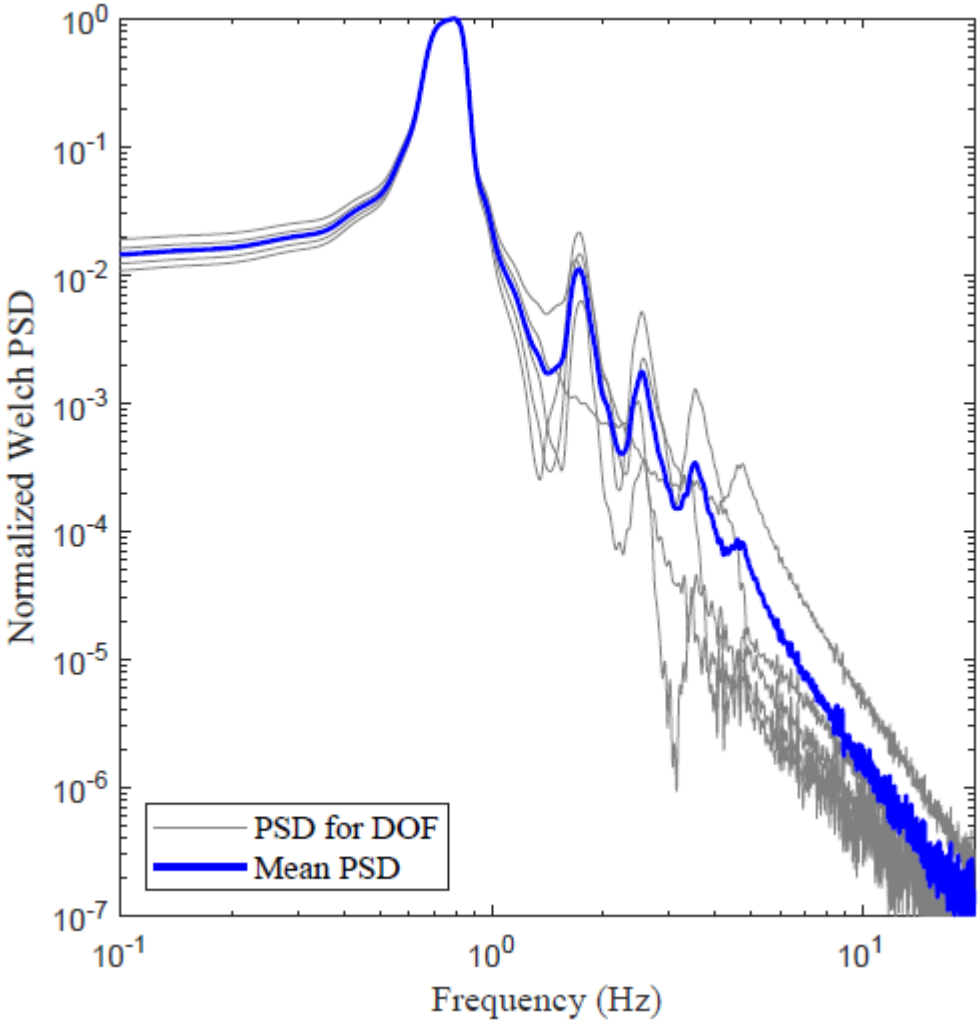

Figure 2.11 Plot of PSD for different modes of vibration for degree of freedom one of MDOF system.

Table 2.1 Results of system identification using ARMA model and N4SID model with actual system parameters.

Mode	Actual system parameters		ARMA model		N4SID model	
	T	ξ	T	ξ	T	ξ
1	1.314	0.050	1.300	0.045	1.315	0.050
2	0.577	0.041	0.579	0.038	0.578	0.041
3	0.396	0.046	0.399	0.042	0.397	0.046
4	0.284	0.057	0.287	0.054	0.285	0.056
5	0.217	0.070	0.221	0.067	0.219	0.069

3 Case study

3.1 Introduction

This chapter represents a case study of a residential building located in Lalitpur, Nepal.

The study building is a four-story residential building. The building was constructed in 2013. The location of the building is shown on the map in Figure 3.1. The building is located in a densely populated area of Kathmandu valley at the bank of river Bagmati. Most of the buildings in the neighborhood are medium rise 2 to 5 floors residential buildings. It is noteworthy that case study building represents the typical RC frame building in Kathmandu valley. Figure 3.2 shows the architectural floor plans of the building with vertical cross section. A picture of the building is shown in Figure 3.3. The total plinth area of building is approximately 220m^2. Dimensions used on architectural floor plans and sections are based on Imperial system as provided by the house owner. These dimensions are converted into equivalent international system of units (SI units).

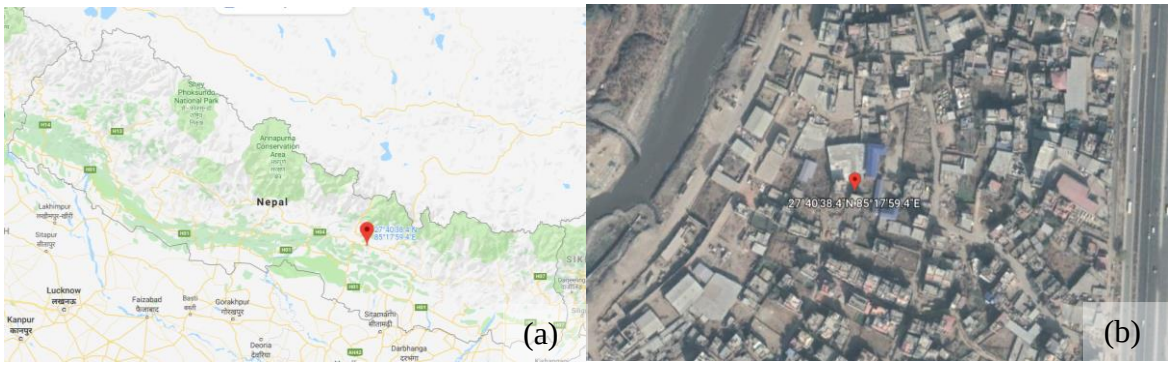

Figure 3.1 (a) Location of building on map of Nepal. (b) satellite map of building site (modified from: google map, 2019).

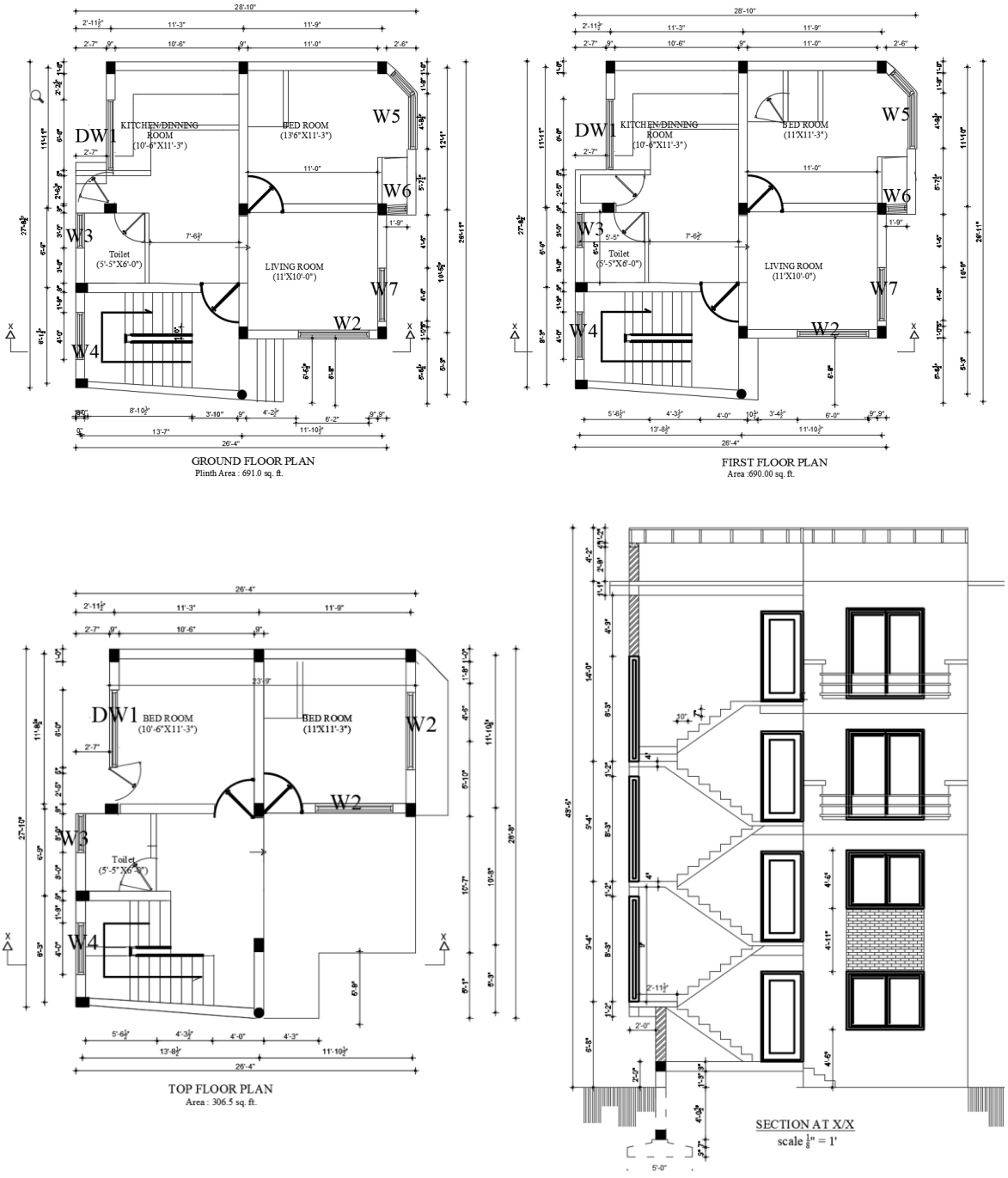

Figure 3.2 Architectural plan view and cross section of the building (Drawing provided by: house owner Pragya Acharya Dhakal).

Figure 3.3: (a) South elevation of the building. (b) West elevation of the building.

3.2 Structural configuration of the building

The structural configuration of the building is a reinforced concrete frame building with brick infill walls. Primarily, structural system of moment resisting frame structure consists of concrete columns, beams and floor slabs. Locally made brick with cement-sand mortar; as brick masonry is used as infill walls on the building, this possess significant contribution to the overall stiffness of the building (see, for example, Varum et al. 2015 and Furtado et al. 2019). That is why, this study includes brick masonry infill wall as a structural element of the building.

Figure 3.4 shows the structural layout of the building showing location of beams and columns. The building is asymmetrical in plan with off grid location of columns and beams. All the rectangular columns have section size of 300×230mm except the circular column which has diameter of 230mm. All the beams have section size of 230×355mm including uniform slab thickness of 100mm. Two types of brick masonry walls were used, external walls are of 230mm thickness (same as the width of the column); whereas, the internal walls are of 110mm thickness.

Figure 3.4 also shows the typical cross section for columns and beams with detailed information about reinforcement. All the rectangular columns having size 300×230mm consist 4-16ϕ and 2-12ϕ reinforcement bars as shown in Fig. 3.4. Similarly, circular column consists of 4-12ϕ reinforcement bars. Stirrups used in all columns are 8ϕ reinforcement bars with spacing of 150mm c/c as shown in Fig. 3.4. All the beams shown in the figure have the dimension of 230×355mm and consist of 2-16ϕ bars at the bottom and 2- 12ϕ bars at the top. Alike the columns, stirrups used in beams are 8ϕ bars at the spacing of 150mm c/c. All the beams are casted monolithically with 100mm thick concrete floor slab. Reinforcements used in slab are 10ϕ bars at the spacing of 150mm c/c for the

bottom mesh and 8ϕ bars at the spacing of 150mm c/c for the top mesh. Clear cover provided for both top and the bottom reinforcement mesh is 20mm.

Figure 3.5 shows typical cross section of a footing at the base of the columns. At the base of each column, isolated spread concrete footing is provided to transfer load from super structure to the soil. This type of footing is most common for residential RC construction in Nepal. Size of most of the column footings at the base is 1.5×1.5m except for the column at grid intersections D3 and F3. Two columns at grid intersections D3 and F3 are close to each other and have common footing of size 3.1×1.5m. Depth of footing from top of ground floor tie beam to the base of footing is 2.26m. All the footings are tied together by tie beams at ground level and top of footing as shown in Fig. 3.5. Tie beam provided at two locations have size of 230×230mm size with 2-16ϕ bars at the bottom and 2-12ϕ bars at the top. Single mesh of reinforcement is provided at the base of footing with 12ϕ bars at 150 c/c spacing.

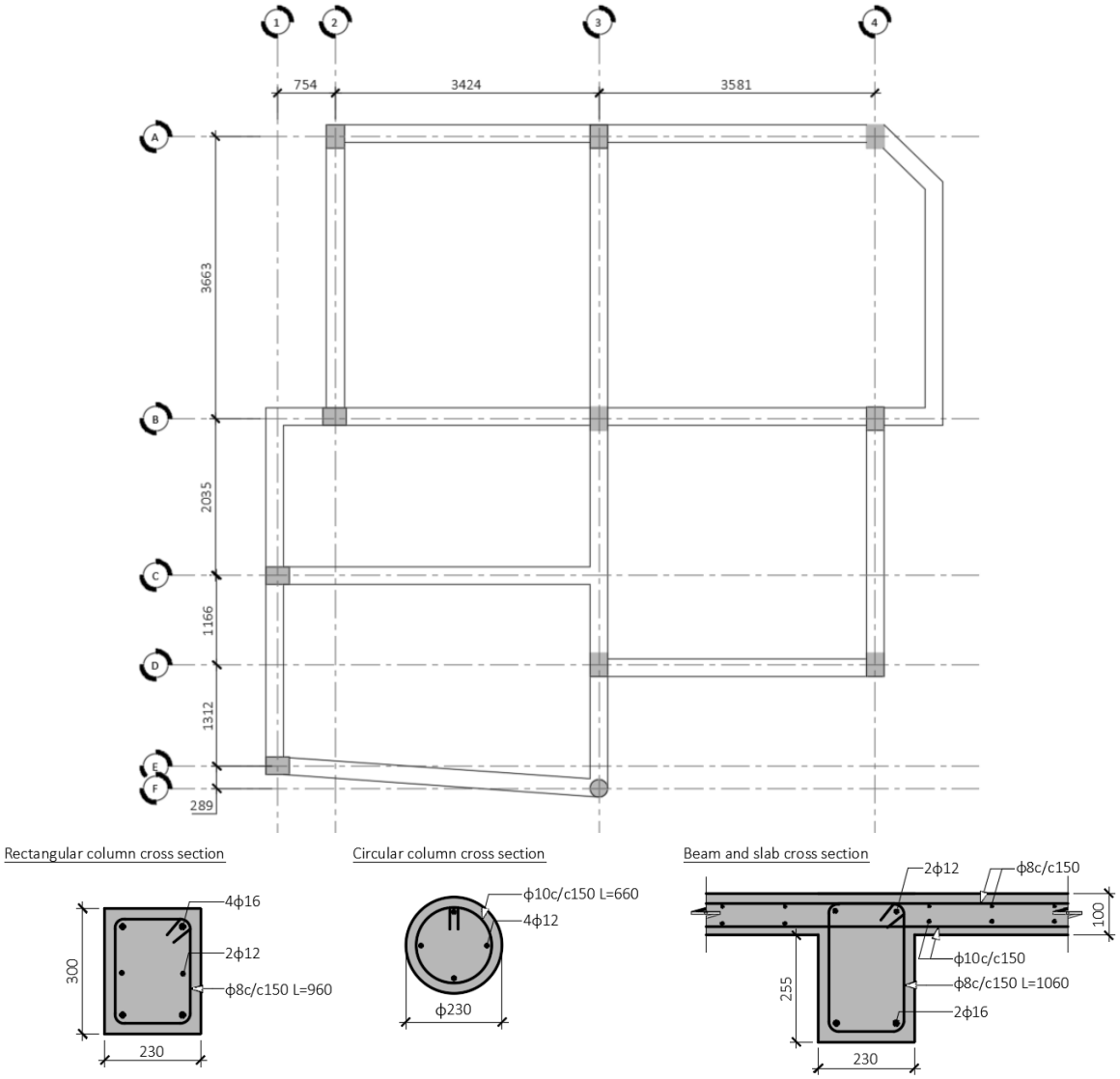

Figure 3.4 Structural layout of the building showing beams and columns and their cross sections with detailed information about reinforcement.

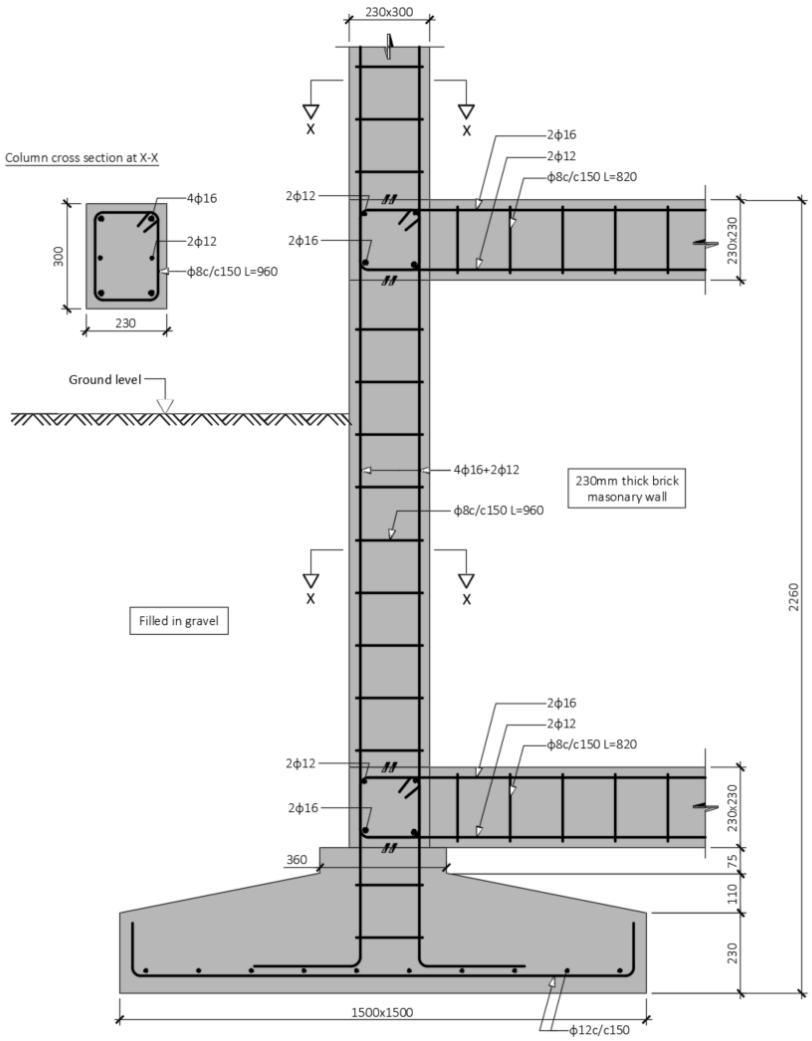

Figure 3.5 Typical foundation detail at base of column with tie beams.

3.3 Mechanical properties of reinforced concrete

Concrete used in the building is ordinary concrete with mix proportions of 1:2:4 (cement: sand: aggregate) equivalent to grade M15 which is obtained from back projection approach considering the state-of-the-art practices. The best estimated unit weight of the concrete is 24.5kN/m^3. Specified characteristic compressive strength of a cube [150mm] in 28days for M15 concrete is 15MPa. Thus, the modulus of elasticity of concrete can be estimated as:

$$E_c = 5000\sqrt{f_{ck}} \approx 19365 \text{ MPa} \quad (3.1)$$

Where, f_{ck} is the characteristic compressive strength of concrete cube in 28 days. Actual measured values may differ by ±20% from the above obtained value using IS 456:2000.

Structural reinforcement used in the building are deformed steel bars of strength grade Fe415. The specified minimum 0.2% proof stress or yield strength of corresponding grade steel is 415N/ mm^2 (IS 1786-1985). The modulus of elasticity of steel is taken as 200GPa.

3.4 Mechanical properties of masonry wall

The masonry walls in different parts of the world are different and unique in terms of strength, quality, size, workmanship of construction, etc. Study of mechanical properties of masonry walls is therefore an interesting research field. Various researchers have suggested the Young's modulus of elasticity of brick masonry variably. The range of values is reported to be varying significantly as reported by several researchers (see, for example, Phaiju and Pradhan 2018). However, it is essential to obtain correct mechanical properties of brick masonry wall in order to depict the contribution of its stiffness to overall structural performance of the building.

Based on the discussion with the owner of building, bricks used in building were the first-class hand-made bricks and mortar used has 1:5 cement to sand ratio by volume. The estimated unit weight of the such masonry wall is 18.85KN/m^3 (IS 875 (Part 1)- 1987). According to NBC 109:1994 some of the commonly-used mortars in Nepal and their mix proportions, along with their strength, are listed in Table 3.1. This constitutes mortar of type M1 with minimum compressive strength at 28 days around 5MPa. For commonly used mortars conforming to above the optimum mortar mixes from a brick strength consideration are given in Table 3.1. The mechanical properties of locally available handmade brick of Kathmandu may be considered to have compressive strength of around 11MPa (Phaiju and Pradhan 2018).

Table 3.1 Optimum mortar mixes for maximum masonry strength with masonry units of various strengths (NBC 109:1994).

Masonry unit strength (N/mm^2)	**Mortar type**
Below 5	M2
5 to 14.9	M1
15 to 24.9	H2
25 or above	H1

Hendry (2003) suggests a relationship between brick crushing strength and brickwork strength for various mortar strengths which is shown in Figure 3.6. The estimated strength for the brickwork of the case study building is 2.5MPa. Various formulae have been suggested for determination of Young´s modulus of elasticity based on masonry strength. Most of the empirical expressions suggested by various researchers fall within the range Em = 400*fm to 1000*fm, where fm is the compressive strength of masonry panel and Em is the Young's modulus of elasticity of Masonry wall (Hendry 2003). Hendry (2003) suggests, Em=700fm.

Based on this equation, the estimated Young's modulus is $E_m=700f_m=1750MPa$

Table 3.2 Mix proportions and strength of commonly used mortars for masonry (NBC 109:1994).

Serial No.	Mix (by volume)			Compressive strength at 28days (N/mm^2)	Mortar type
	Cement	Lime	Sand		
1	1	0 to 0.25C	3	10.0	H1
2(a)	1	0	4	7.5	H2
2(b)	1	0.5C	4.5	6.0	H2
3(a)	1	0	5	5.0	M1
3(b)	1	1C	6	3.0	M1
4(a)	1	0	6	3.0	M2
4(b)	1	2C	9	2.0	M2
4(c)	0	1A	2 to 3	2.0	M2
5(a)	1	0	8	0.7	L1
5(b)	1	3C	12	0.7	L1
6	0	1B or C	2 to 3	0.5	L2

According to Phaiju and Pradhan (2018) compressive strength, Young´s modulus of elasticity and shear modulus of elasticity for masonry wall are 2.5MPa, 2703.2MPa and 915.1MPa respectively. Similarly, poisons ratio is 0.32. However, the author suggests many factors which affect the strength and quality of brick masonry. Hence, the estimated value for compressive strength and Young's modulus of elasticity for brick masonry is taken as 2.5MPa and 1750MPa respectively.

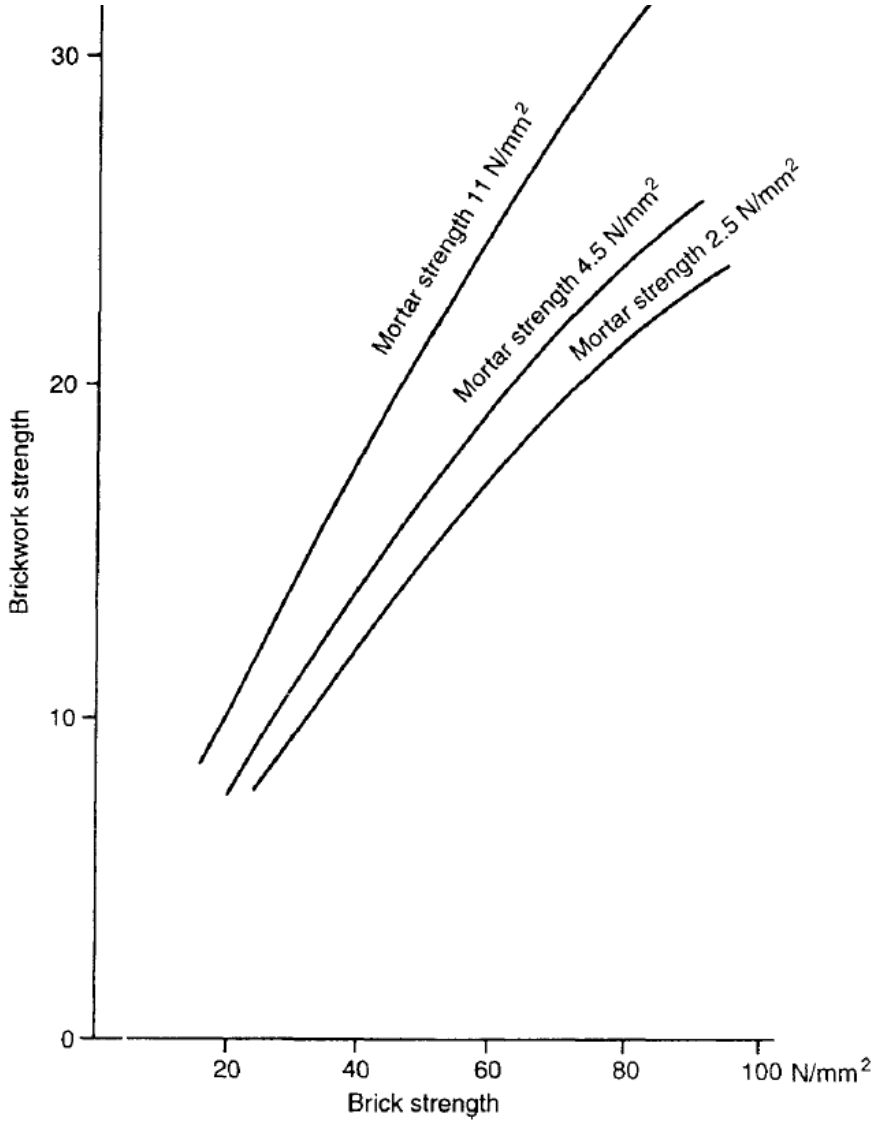

Figure 3.6 Relationship between brick crushing strength and brickwork strength for various mortar strengths (Hendry 2003).

3.5 Mechanical properties of soil and structural soil interaction

Almost all structures are founded on ground in one way or another. Dynamic properties of the engineering structure depend, to an extent, on the underlying soil properties. When engineering structure with certain dynamic properties is founded on material which has different dynamic properties, the overall response depends upon the coupling between two systems. This process where response of the soil influences the motion of the structure and the response of the structure influences the motion of the soil is called soil structure interaction (SSI). If a lightweight flexible structure rests on a very stiff soil material (for example rock) the response of the coupling system is less influenced compared to stiff and heavy structure resting on flexible soil material.

Estimation of correct soil properties depends upon several parameters. The seismic shear wave velocity (V_s) of the upper layer of the soil is a governing parameter for estimation of soil properties. In most of the ground response analyses, maximum shear modulus of soil (G_{max}) is used to evaluate the dynamic response of soils and is estimated from shear wave velocity. The most reliable means of evaluating G_{max} from shear wave velocity and soil mass density (ρ) can be represented as,

$$G_{max} = \rho V_s^2 \quad (3.2)$$

There are many empirical correlations between the geotechnical properties of soil and V_s. A power equation model in the form of $V_s = AN^B$ is widely used model for determination of V_s from geotechnical parameters, where N equation represents the standard penetration resistance from standard SPT test and A and B are empirical constants. In case of Kathmandu, geotechnical observation (SPT-N value) for shallow depth are accomplished in most of the commercial and government constructions (Gautam 2016). However, measuring the shear wave velocity V_s is not common. Since, empirical equation V_s-N is a good approach to estimate V_s. Gautam (2016) developed three equations for Kathmandu valley soil with correlations given by,

All soil conditions $V_s = 115.8N^{0.251}$ ($R^2 = 0.623$) (3.3)

Silty soil conditions $V_s = 102.4N^{0.274}$ ($R^2 = 0.355$) (3.4)

Sandy soil conditions $V_s = 78.7N^{0.352}$ ($R^2 = 0.441$) (3.5)

SPT test results conducted near the building location are presented in appendix A. Test results consist of N value for every 1.5m depth for total of 20m deep borehole at three locations. First few meters of the soil show comparatively low N values which represents loosely compacted soil. As the depth increases N values of soil also increases. Estimated shear wave velocity at the three test locations are tabulated in Table 3.3. Mean estimated shear wave velocity for top 20m of soil is 230m/s. The mass density of the soil material is estimated to be 1800kg/m^3 and the Poisson´s ratio is 0.35.

Table 3.3Estimation of shear wave velocity for 20m soil at three boreholes.

Depth (m)	Borehole no. 1 (m/s)	Borehole no. 2 (m/s)	Borehole no. 3 (m/s)
1.5m	229	249	153
3.0m	175	198	124
4.5m	167	0	124
6.0m	202	207	215
7.5m	207	215	223
9.0m	226	223	226
10.5m	233	226	233

12.0m	242	239	239
13.5m	239	262	253
15.0m	247	258	255
16.5m	253	271	247
18.0m	277	292	253
20.0m	285	296	253
Mean	229	245	215
Mean of the three boreholes		230m/s	

Once mechanical properties of the soil material are known stiffness and damping coefficients for foundation can be computed. The stiffness and damping are contributed by both the structure and soil material. The soil components can be derived from the frequency dependent impedance function of the soil. These functions are readily available for circular footing (Datta 2010). For other type of footing, for example rectangle and square, impedance function can be estimated from the area of an equivalent circular footing. In actual conditions the stiffness and damping coefficients of the foundation are frequency dependent. However, to illustrate the effect of structural soil interaction frequency independent approximate expression are nowadays popular. This assumption allows the soil to be replaced by a spring and dashpot. Expressions available for estimation of stiffness and damping are tabulated in Table 3.4. Estimated spring constants for undamped soil using formulas listed on Table 3.4 are listed on Table 3.5. These estimated spring constants will be used in the finite element model of the building in chapter 5 for modelling of structure soil interaction.

Table 3.4 Stiffness and damping coefficients for circular rigid foundation (Datta 2010).

Component	**Stiffness parameter**	**Damping parameter**
Vertical	$K_{vert} = \frac{4Gr}{1-\upsilon}$	$C_{vert} = \frac{3}{1-\upsilon}\rho V_s r^2$
Horizontal	$K_h = \frac{8Gr}{2-\upsilon}$	$C_h = \frac{4.6}{2-\upsilon}\rho V_s r^2$
Rocking	$K_\theta = \frac{8Gr^3}{3(1-\upsilon)}$	$C_\theta = \frac{0.4}{1-\upsilon}\rho V_s r^4$
Torsional	$K_\varphi = 5.3Gr^3$	$C_\varphi = 0.8\rho V_s r^4$

V_s is the shear wave velocity; r is the radius of the circular footing; G is the shear modulus; υ is the Poisson´s ratio; ρ is the mass density of the soil material.

Table 3.5 Input parameters and estimated stiffness of springs.

Parameter	Symbol	Value
Shear modulus	G_{max}	95.22MPa
Mass density of soil	ρ	1800kg/m^3
Effective radius for footing	r	0.85m
Shear wave velocity	Vs	230m/s
Vertical stiffness	K_{vert}	$4.96x10^8$ N/m
Horizontal stiffness	K_h	$3.99x10^8$ N/m
Rocking rotation	K_θ	$2.37x10^8$Nm

4 System identification of the case-study building

4.1 Ambient vibration measurement

Three digital accelerometers were installed on three different floors to record ambient vibration of the building. The instruments were located on the first second and the third floor. Figure 4.1 shows the location of instruments (red rectangle) on the first floor of the building. Other two instruments on higher floors aligned vertically with the instrument on the first floor. The accelerometers used are ETNA2 units manufactured by Kinemetrics Inc. All the instruments were clamped to the floor slab which is one of the structural systems of the building. Direction of the measurement with respect to accelerometer sensors is indicated by co-ordinate axis in the figure. Measurement of the vibration along X-axis of instrument will be referred to as channel 1 and denoted as ch-1, and that along Y-axis will be referred to as channel 2, denoted by ch-2 hereafter. Measurement of vibration along Z-axis or perpendicular to plan view will be referred to as channel 3 and denoted by ch-3.

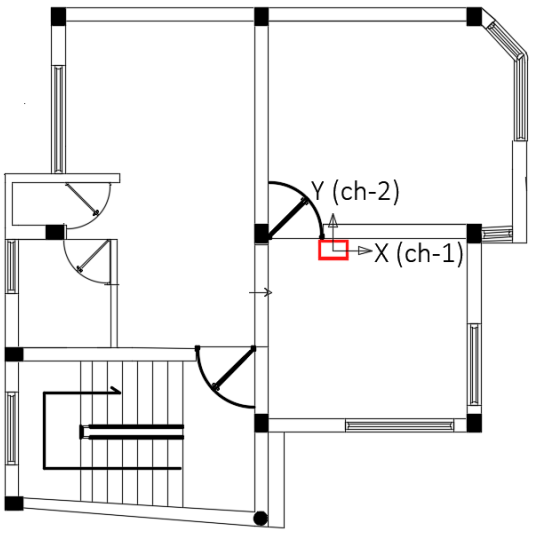

Figure 4.1 Location of instrument on first floor of the building with the orientation of the instrument sensor axis.

Ambient vibration was recorded on 13 February 2019. The total length of the record is 60 minutes with data sampling interval of 0.01s. Figure 4.2 shows the time series recorded by the instrument on the first floor along channel 1 and 2.

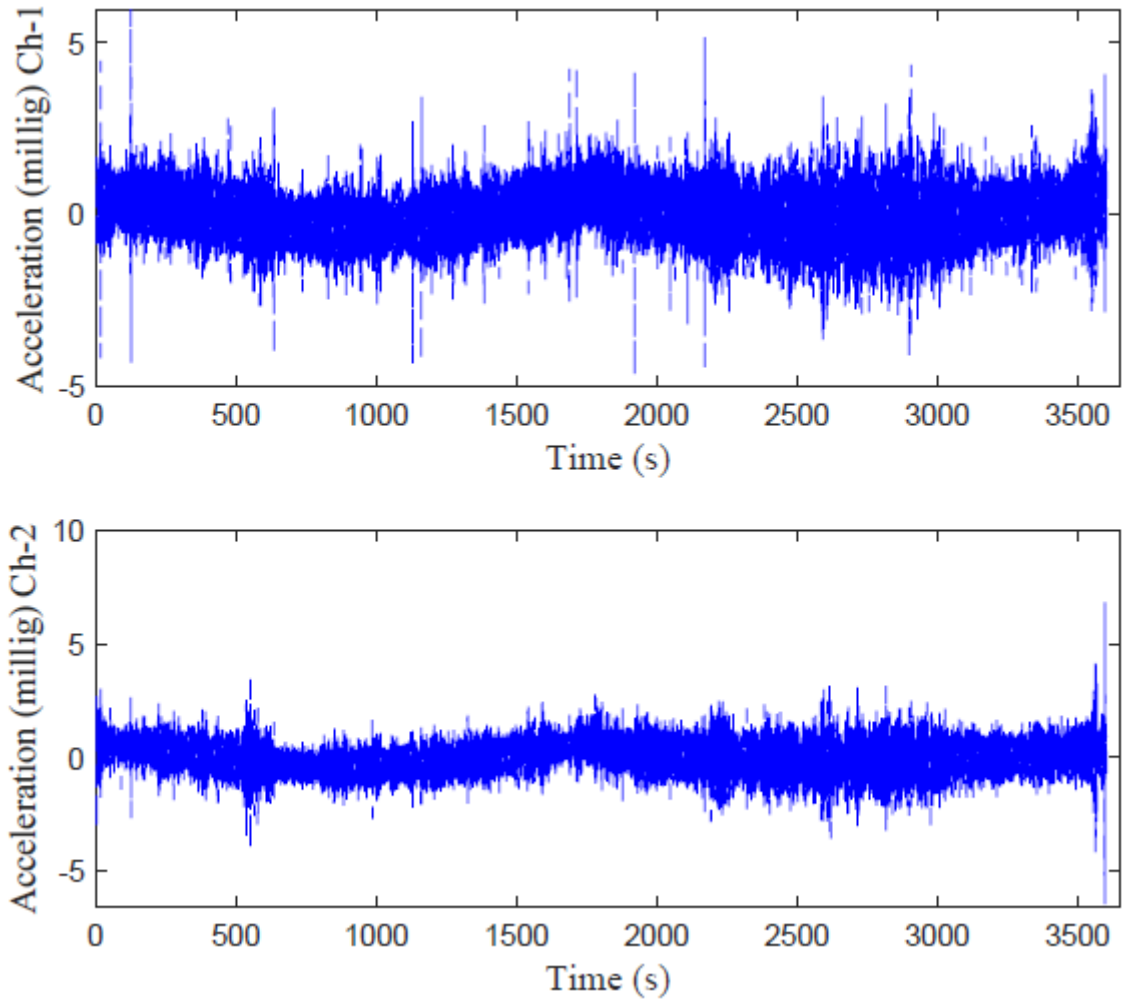

Figure 4.2 Ambient vibration recorded on the first floor along channel 1 and 2.

4.2 Welch spectral analysis

Recorded time series from all three floors from channel 1 and channel 2 were divided into twenty equal segments. Then the signals were filtered using fourth order Butterworth filter to get rid of noise. The frequency band chosen for the filter was 0.5Hz (T=2sec) to 20Hz (0.05sec). Each segment of time series was windowed and tapered with a Tukey window. Power spectral density (PSD) of the filtered signals was estimated using Welch´s algorithm. As stated in previous chapter, first peak of the estimated PSD gives fundamental frequency of the system. Similarly, half power of the PSD is used to estimate damping ratio of the system.

Figure 4.3 shows the plot of estimated PSD of the twenty segments with mean PSD for both channels. Six different plots in logarithmic scale are generated. Figure 4.3 on the left (figure (a), (c) and (e)) shows plot of PSD from first floor to third floor data of channel 1 with estimated mean PSD. Similarly, right figures (figure (b), (d) and (f)) shows plot of PSD from first floor to third floor of channel 2. All figures show clear peak which represents the fundamental frequency of the system along the corresponding direction.

Results obtained from the twenty segments of data recorded at the first floor along channel 1 and channel 2 is tabulated in Table 4.1 and Table 4.2 respectively. Mean fundamental vibration period obtained from first floor data of channel 1 is 0.290s with standard deviation 0.017s. Similarly, fundamental vibration period obtained from channel 2 is 0.289s with standard deviation 0.028s. Results obtained from second floor and third floor data are tabulated in Table 4.3 and Table 4.4 respectively. Mean natural period obtained from the second floor and third floor along channel 1 is 0.288s and 0.289s respectively. Mean natural period obtained from second floor and third floor along channel 2 is 0.296s and 0.291s respectively. Therefore, it can be concluded that the mean estimated fundamental period of the building along channel 1 is 0.289 and along channel 2 is 0.292s. This concludes that the fundamental periods of the building on both the directions are almost similar.

Mean damping ratios estimated from first floor along channel 1 and channel 2 are 8.1% and 11.4%, respectively. Standard deviation calculated for both the channels shows wide variety of estimated results. Similarly, mean damping ratios estimated from second floor and third floor data are shown on Table 4.3 and Table 4.4, respectively. These variable results obtained for damping ratio is directly related to the smoothing, window selection and overlap of data during PSD estimation. For example, Smoothing of PSD leads to flattening of the peaks which results in inaccurate estimates of damping ratios (Peeters and De Roeck 2001). Therefore, estimated damping ratios from this method will not be considered for further discussion.

In summary, the estimated mean vibration period of the building using data recorded from three floors along channel 1 is 0.289s. Similarly, estimated mean vibration period of the building along channel 2 is 0.292s.

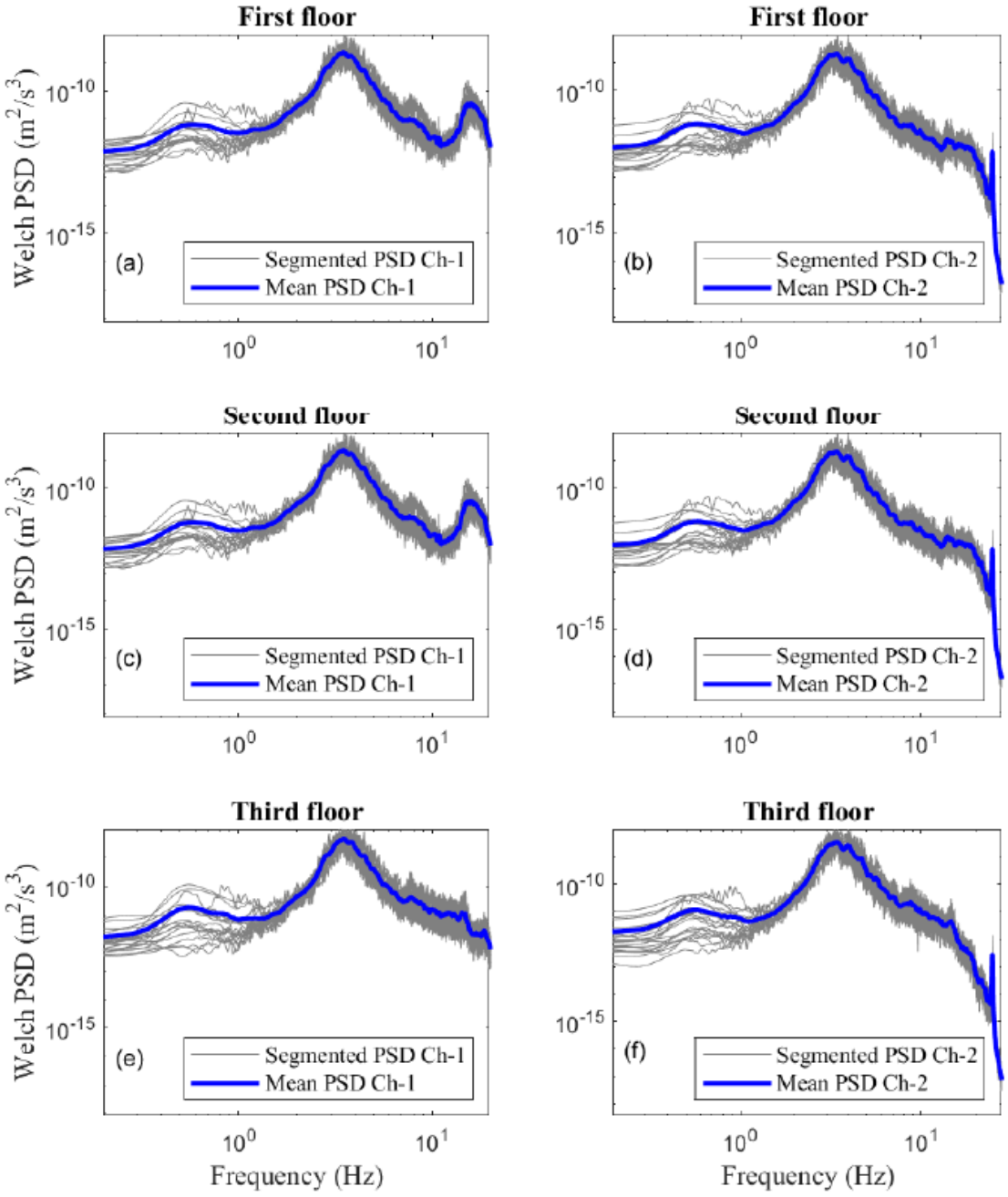

Figure 4.3 Plot of Welch´s PSD from recorded ambient vibration : (a) and (b) Welch´s PSD for twenty segment of data recorded on first floor along channel 1 and channel 2 respectively. The solid blue line represents mean of the twenty PSDs. (c) and (d) Welch´s PSD for twenty segments of data recorded on second floor along channel 1 and channel 2 respectively. The solid blue line represents mean of the twenty PSDs. (e) and (f) Welch´s PSD for twenty segments of data recorded on third floor along channel 1 and channel 2 respectively. The solid blue line represents mean of twenty PSD.

Table 4.1 Fundamental vibration period, fundamental frequency, damping ratio and standard deviation estimates from first floor data of channel 1.

Data	Fundamental period (s)	Fundamental frequency (Hz)	Damping ratio (%)
Segment 1	0.282	3.540	2.958
2	0.303	3.302	0.453
3	0.324	3.087	6.290
4	0.292	3.427	12.138
5	0.315	3.171	8.463
6	0.276	3.628	4.533
7	0.281	3.565	6.285
8	0.261	3.826	8.960
9	0.306	3.264	7.317
10	0.286	3.494	10.227
11	0.316	3.167	9.874
12	0.298	3.356	14.558
13	0.280	3.569	3.771
14	0.297	3.362	13.234
15	0.283	3.528	8.873
16	0.286	3.494	10.227
17	0.295	3.391	13.556
18	0.286	3.500	8.096
19	0.278	3.595	6.232
20	0.255	3.923	6.472
Mean	0.290	3.459	8.126
SD	0.017	0.209	3.681

Table 4.2 Fundamental vibration period, fundamental frequency, damping ratio and standard deviation estimates from first floor data of channel 2.

Data	Fundamental period (s)	Fundamental frequency (Hz)	Damping ratio (%)
Segment 1	0.277	3.615	9.477
2	0.326	3.072	11.612
3	0.324	3.086	6.774
4	0.290	3.452	0.867
5	0.298	3.355	19.678
6	0.281	3.564	14.542
7	0.302	3.306	12.574
8	0.288	3.470	8.166
9	0.345	2.895	11.300
10	0.316	3.169	9.404
11	0.295	3.388	5.294
12	0.320	3.127	12.816
13	0.279	3.585	16.070
14	0.263	3.801	18.942
15	0.254	3.945	9.067
16	0.257	3.887	14.847
17	0.249	4.017	12.930
18	0.287	3.488	17.323
19	0.285	3.509	3.835
20	0.240	4.164	13.182
Mean	0.289	3.495	11.435
SD	0.028	0.341	4.939

Table 4.3 Mean fundamental vibration period, fundamental frequency, damping ratio and standard deviation estimates from second floor data of channel 1 and channel 2.

Description	Fundamental period (s)	Fundamental frequency (Hz)	Damping ratio (%)
Mean - Second floor channel -1	0.288	3.480	8.389
Standard deviation	0.017	0.211	3.901
Mean - Second floor channel -2	0.296	3.403	9.165
Standard deviation	0.023	0.267	4.713

Table 4.4 Mean fundamental vibration period, fundamental frequency, damping ratio and standard deviation estimates from third floor data of channel 1 and channel 2.

Description	Fundamental period (s)	Fundamental frequency (Hz)	Damping ratio (%)
Mean - Third floor channel -1	0.289	3.461	9.148
Standard deviation	0.016	0.196	4.303
Mean - Third floor channel -2	0.291	3.457	11.655
Standard deviation	0.027	0.320	6.211

4.3 N4SID Method

4.3.1 Model order selection

Selection of suitable model order is important for this algorithm. Selection of suitable model number helps to remove spurious modes and bias of the modes. Spurious modes are either noise modes, that arise due to physical reasons, e.g., excitation and noise or mathematical modes that arise due to over-estimation of the model order. Similarly, bias of the modes can be defined as the combination of different modes (true mode and noise mode) on identified mode which is due to under estimation of model order. The selection of suitable model order can be decided from stabilization diagram. A stabilization diagram is made by selecting a wide range of model orders for the identification and by plotting all identified modes in a frequency verses model order diagram. Figure 4.4 and Figure 4.5 shows the stabilization diagrams for data segment 5 for channel 2 and channel 1 respectively. Both the plots show the estimated natural frequencies and damping ratios from 1 to 20 modes using least square rational function (LSRF) algorithm. In the figure, if the modal frequency, the damping ratio and related mode shape differences are within limit, the pole is labelled as stable. Frequency range selected for the plot is 0.5Hz to 20Hz. Some of the true modes, such as mode 3 on Figure 4.4, is initially unstable, while it is

stable from mode order 4. Similarly, on Figure 4.5 some of the true mode only appears after model order 4. If model order was chosen less than 4, some of the true mode might not appear on result and bias errors as explained above appears on the results. On both the figures, model order higher than 4 has stable frequency and damping at different modes. Hence the model order is selected as 6.

4.3.2 System Identification result

The measured signals from all three floors are aligned in time. The aligned signals from channel 1 and channel 2 were than divided into twenty segments. Signals were filtered using fourth order Butterworth filter to get rid of noise. The frequency band chosen for the filter was 0.5Hz (T=2s) to 20Hz (0.05s). Then N4SID algorithm in MATLAB is used to estimate state-space model with the model order of six. The system identification results are shown in Table 4.5 and Table 4.6.

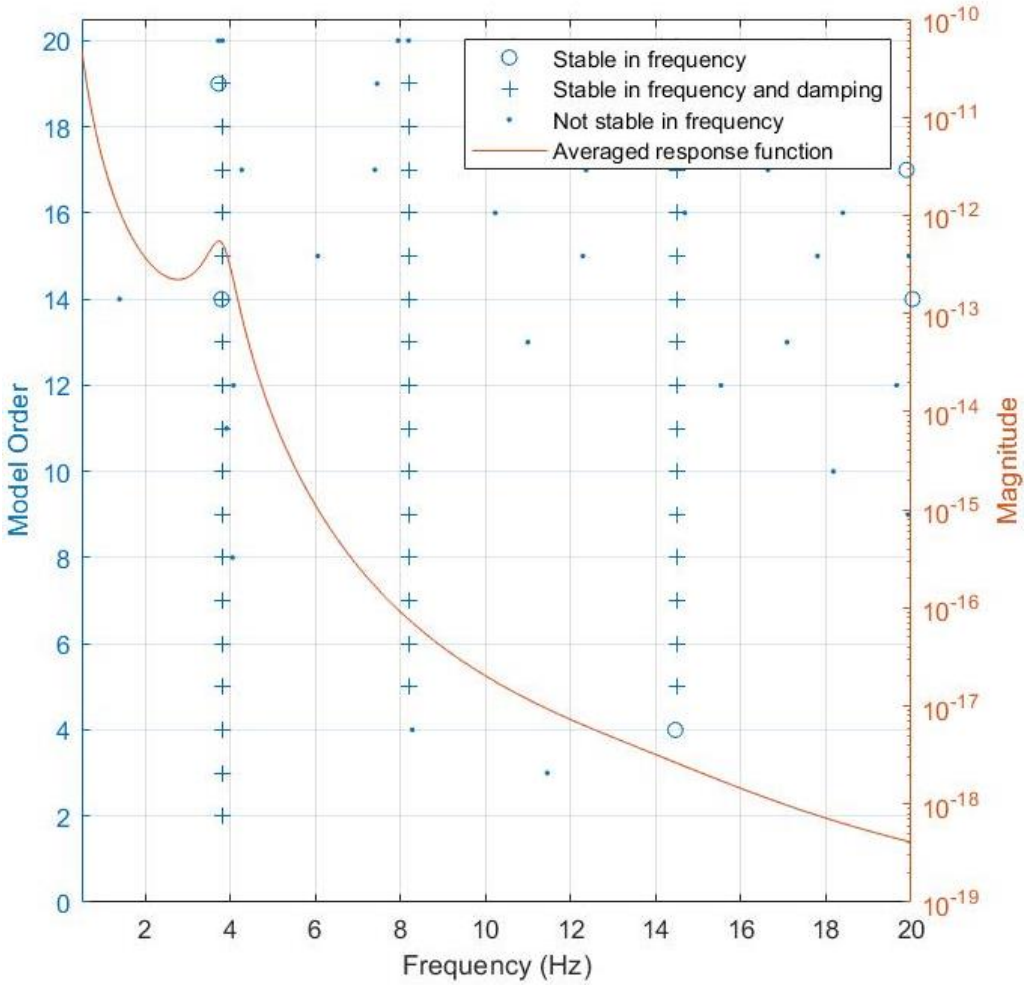

Figure 4.4 Stabilization diagram showing stable modes and averaged frequency response function for data segment 5 channel -2.

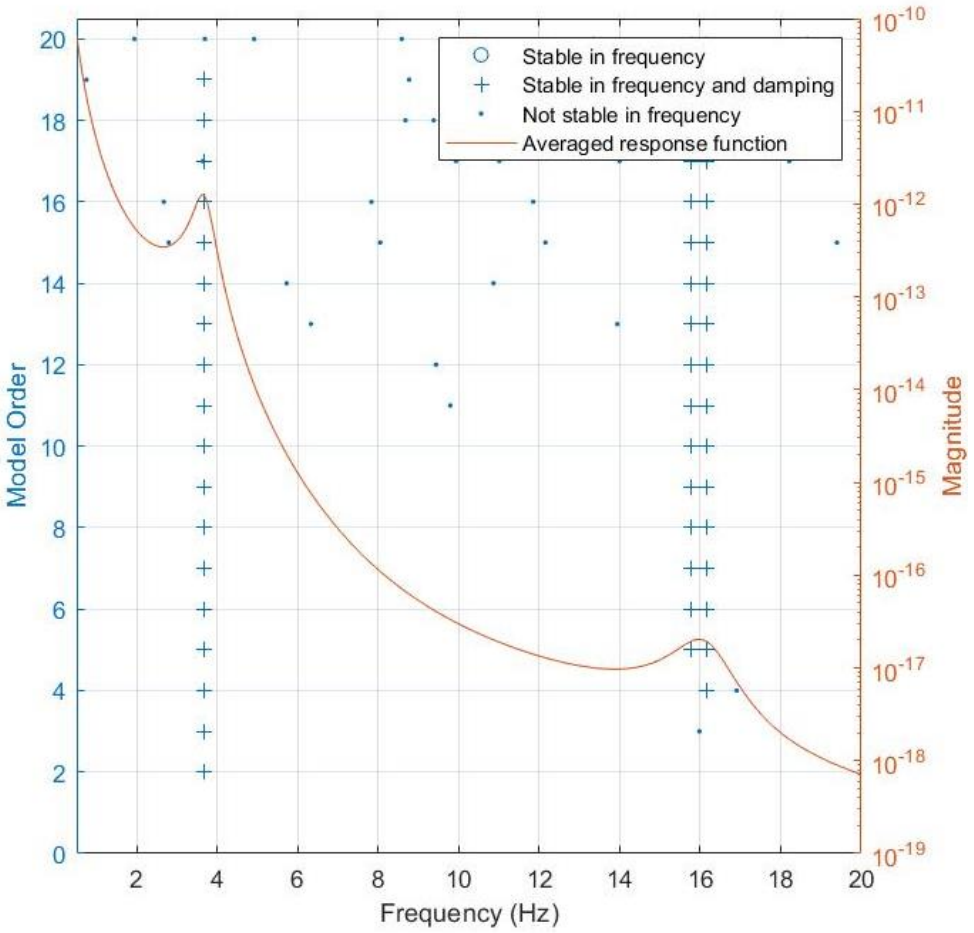

Figure 4.5 Stabilization diagram showing stable modes and averaged frequency response function for data segment 5 channel -1.

The mean vibration period for first and second mode obtained from channel 1 data is 0.266s and 0.078s with standard deviation of 0.009s and 0.031s. Similarly, the mean vibration period for first and second mode obtained from channel 2 data is 0.264s and 0.143s with standard deviation of 0.012s and 0.035s respectively. This shows that the variance of period obtained for second mode is higher than that for the first mode. In general, the errors for the estimation of first pair of modes are lower compared to higher modes. Also, for some segments (example; segment 1 mode 2 for ch-1 and ch-2), there is significant difference in estimated vibration period, indicating less accurate estimate. However, for most of the segments, the estimated fundamental vibration periods are consistent.

Mean damping ratio obtained from channel 1 data is about 6.3% with standard deviation of 1.3%. Similarly, mean damping ratio obtained from channel 2 data is about 7% and standard deviation of 1.1%. From these results, it can be said that the estimated damping ratio varies less compared to non-parametric spectral method.

Table 4.5 Fundamental vibration period, fundamental frequency and damping ratios obtained for first 2 modes from N4SID algorithm for channel 1.

Data	Fundamental period (s)		Fundamental frequency (Hz)		Damping ratio (%)
	Mode 1	**Mode 2**	**Mode 1**	**Mode 2**	**Mode 1**
Segment 1	0.265	0.206	3.771	4.862	4.863
2	0.276	0.070	3.628	14.266	5.234
3	0.275	0.067	3.639	15.032	6.494
4	0.259	0.065	3.859	15.416	6.112
5	0.271	0.063	3.692	15.780	6.751
6	0.270	0.064	3.702	15.621	5.791
7	0.273	0.065	3.661	15.430	7.614
8	0.266	0.068	3.766	14.802	5.194
9	0.269	0.070	3.713	14.259	6.667
10	0.271	0.065	3.689	15.348	5.607
11	0.276	0.066	3.621	15.087	5.919
12	0.271	0.074	3.693	13.488	7.096
13	0.273	0.063	3.670	15.949	5.148
14	0.268	0.091	3.731	11.028	3.840
15	0.252	0.079	3.962	12.622	8.659
16	0.251	0.087	3.978	11.508	8.270
17	0.249	0.082	4.008	12.192	7.518
18	0.247	0.070	4.053	14.190	8.213
19	0.268	0.070	3.727	14.361	5.742
20	0.267	0.070	3.742	14.278	6.071
Mean	**0.266**	**0.078**	**3.765**	**13.776**	**6.340**
SD	**0.009**	**0.031**	**0.133**	**2.531**	**1.265**

Table 4.6 Fundamental time period, fundamental frequency and damping ratios obtained for first 2 modes from N4SID algorithm for channel 2.

Data	**Fundamental period (s)**		**Fundamental frequency (Hz)**		**Damping ratio (%)**
	Mode 1	**Mode 2**	**Mode 1**	**Mode 2**	**Mode 1**
Segment 1	0.279	0.264	3.581	3.788	5.420
2	0.276	0.125	3.622	8.015	6.207
3	0.276	0.121	3.622	8.245	6.391
4	0.255	0.111	3.916	9.008	6.132
5	0.262	0.122	3.819	8.192	8.404
6	0.270	0.130	3.706	7.685	6.001
7	0.272	0.116	3.682	8.637	7.192
8	0.257	0.150	3.886	6.658	7.720
9	0.271	0.150	3.694	6.666	7.496
10	0.279	0.170	3.589	5.866	4.899
11	0.276	0.138	3.622	7.221	6.748
12	0.275	0.160	3.633	6.248	6.326
13	0.265	0.117	3.777	8.577	7.510
14	0.261	0.178	3.832	5.625	5.415
15	0.250	0.138	4.005	7.225	7.212
16	0.250	0.123	4.002	8.144	6.600
17	0.247	0.139	4.042	7.196	8.252
18	0.241	0.108	4.151	9.299	7.979
19	0.262	0.156	3.816	6.393	9.123
20	0.259	0.146	3.864	6.849	8.329
Mean	**0.264**	**0.143**	**3.793**	**7.277**	**6.968**
SD	**0.012**	**0.035**	**0.169**	**1.329**	**1.140**

5 Finite Element Modelling

5.1 The Finite element model

A finite element model of the building is created using the software ETABS 2017 Ultimate, version 17.0.1 (CSI 2018). ETABS is a sophisticated, yet user friendly, special purpose analysis and design program developed specifically for building systems (CSI 2018). The software is capable of handling complex building models, including a wide range of nonlinear behaviors. The modelled building on this software can be idealized as an assemblage of shell, frame, link, tendon and joint objects. Those objects represent the physical members of building like columns, beams, floors, walls etc.

A three-dimensional (3D) finite element model (FEM) of the building is created using this software to investigate its dynamic behavior. The FEM model (see Figure 5.1) consists of three-dimensional beam column elements to model the moment resisting reinforced concrete frame and shell elements to model the brick masonry wall of building.

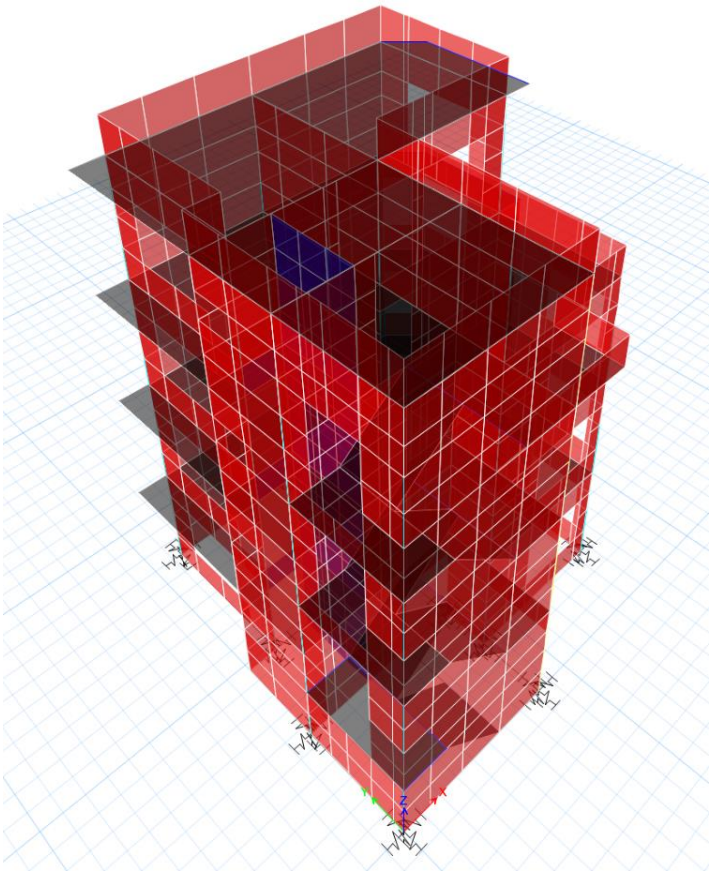

Figure 5.1 ETABS 2017 finite element model of the building

The shell element is used to model the brick masonry wall of the existing building. The main purpose of using shell element is to see the contribution of masonry wall in overall structural stiffness of the building. Also, shell elements are area objects which collect distributed loading and transfer forces to frame system. Figure 5.1 shows the 3D FEM model created on ETABS 2017.

5.2 Material properties

The finite element model is created based on available architectural and structural drawings provided by the house owner. The model consists of columns, beams, slabs and shell elements which are the main structural elements of the existing building.

As described in chapter 3, the mechanical properties of structural elements used on model are listed in Table 5.1. Size of the structural element follows the size shown on architectural drawings.

Table 5.1Mechanical properties of structural components

Structural Element	Material	Density (kN/m^3)	Modulus of Elasticity (MPa)	Poisson's Ratio
Beam	RC	24.5	19365	0.20
Column	RC	24.5	19365	0.20
Shell	Brick masonry	18.85	1750	0.32

Dead load and 25% of imposed live loads are considered for modal analysis per the codal provisions (IS 1893 (Part 1)- 2002). This reflects realistic load distribution for normal condition. Imposed loads on floors are applied based on IS 875 (part 2)- 1987, Table 1 and Table 2. For example, recommended imposed loads on all rooms and kitchens are $2kN/m^2$ for residential buildings. Similarly, uniform area load (additional dead load) of $1.5kN/m^2$ is applied on all floors to accommodate 60mm thick floor finishing materials, which includes screed, marbles and ceramics tiles. Since, model mass of the building consists of summation of loads from structural elements, additional dead load applied on floors for floor finishing materials and 25% of the imposed live load.

5.3 Eigen modes and frequencies

Eigen analysis was conducted to estimate the modal frequencies and mode shapes of the building. It was found that the first 12 modes of vibration constitute to more than 90% of total mass of the building.

Two different finite element models were created with different boundary conditions. For first model, boundary conditions of the structure were defined as a semi-fixed support or

pinned support at the base of structure allowing only rotation but no translation. For second model, it is assumed that the building is not actually fixed for translation degree of freedom at the base. Rather, spring elements were introduced to model soil flexibility. The parameters of the spring elements are as listed in Table 3.5.

5.3.1 Model with pinned support

Table 5.2 shows the results of modal analysis for the first twelve modes of the building with semi-fixed or pinned support. The first mode period is 0.226s with mass participation factor of 83.1% along Y-axis of the model (direction of ch-2). Similarly, the second mode period is 0.207s with mass participation of 79.3% along X-axis of model (direction of ch-1). The first two modes of the building have largest mass participation. Only few modes after the first and second mode have mass participation more than 10%. Hence most of the modes shown in Table 5.2 are insignificant or have less contribution to the overall structural response. The first four mode shapes of the building are shown in Figure 5.2. Coordinate axis shown on figure represents original undeformed nearest corner of the building. First mode shape of the building shows Y-axis as the dominant direction of movement. Similarly, second mode has largest mass participation along X-axis which is displayed in the figure. Third mode shape shows torsion on the building however, mass participation on this mode is insignificant or very low.

Table 5.2 Modal properties of the model with pinned support.

Case	Mode	Period	UX	UY	Sum UX	Sum UY
Modal	1	0.226	0.010	0.831	0.010	0.831
Modal	2	0.207	0.793	0.009	0.802	0.841
Modal	3	0.160	0.007	0.000	0.810	0.841
Modal	4	0.074	0.002	0.121	0.812	0.962
Modal	5	0.070	0.136	0.001	0.948	0.962
Modal	6	0.056	0.008	0.001	0.956	0.963
Modal	7	0.046	0.001	0.024	0.957	0.987
Modal	8	0.043	0.029	0.002	0.985	0.988
Modal	9	0.037	0.000	0.006	0.985	0.995
Modal	10	0.036	0.003	0.001	0.988	0.996
Modal	11	0.033	0.002	0.000	0.990	0.996
Modal	12	0.033	0.005	0.000	0.995	0.996

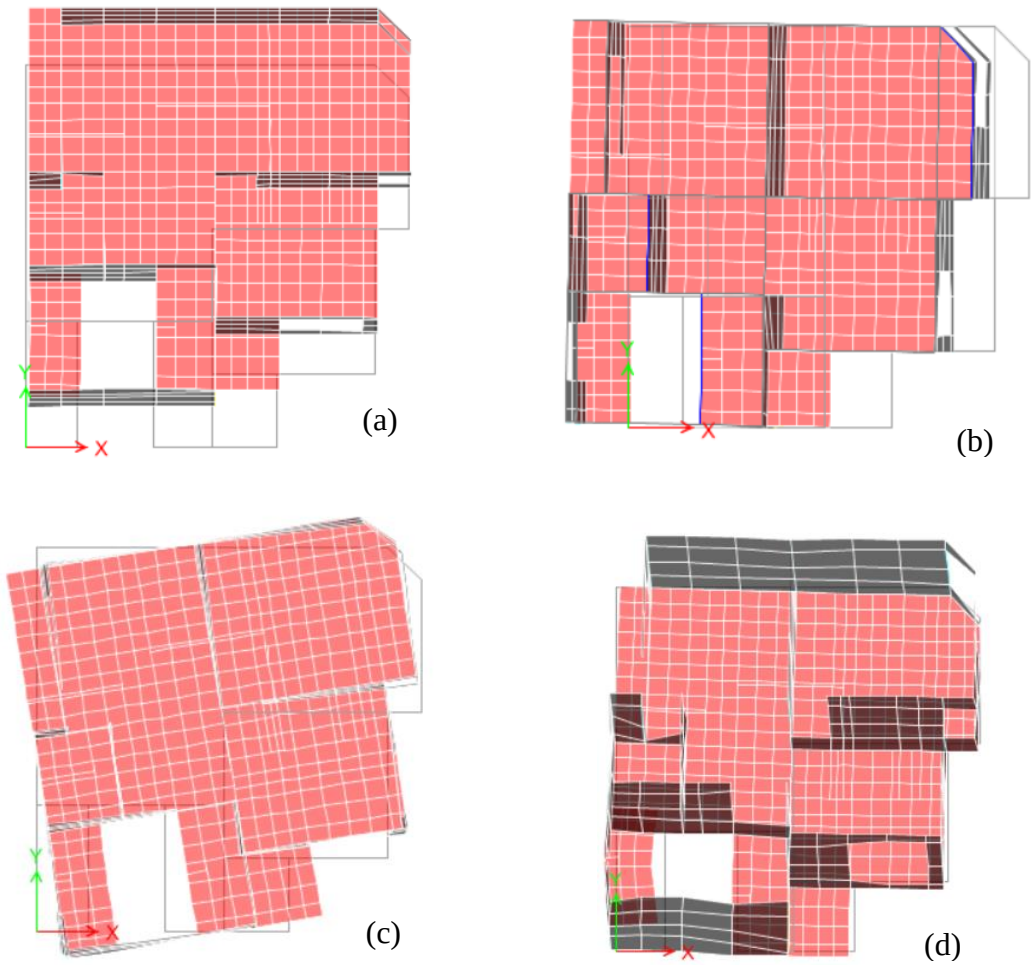

Figure 5.2 Plan views of first four mode shapes of the finite element model of the building obtained from ETABS 2017 with pinned support at base. (a) First mode shape of the building dominant on direction along y-axis. (b) Second mode of the building dominant on direction along X-axis. (c) Third mode shape of the building in torsion. (d) Fourth mode shape of the building dominant on direction along Y-axis.

5.3.2 Model with spring support

Table 5.3 shows the results of modal analysis for first twelve modes of the building with soil springs introduced at the supports. the first mode has period of 0.275s with mass participation of 78.5% along Y-axis of model (direction of Ch-2). Second mode has a period of 0.259s with mass participation of 75.8% along X-axis of model (direction of Ch-1). First five modes of the building have cumulative mass participation of about 90%. Mode shape for first four modes are shown in Figure 5.3. Mode shapes shown in figure are very similar to mode shapes obtained from model with pinned support. However, period and mass participation for significant modes are different.

Table 5.3 Modal properties of the first 12 modes with soil springs introduced in the finite element model.

Case	Mode	Period	UX	UY	Sum UX	Sum UY
Modal	1	0.275	0.002	0.785	0.002	0.785
Modal	2	0.259	0.758	0.002	0.760	0.787
Modal	3	0.180	0.002	0.001	0.762	0.787
Modal	4	0.080	0.002	0.120	0.764	0.907
Modal	5	0.075	0.127	0.001	0.891	0.907
Modal	6	0.063	0.001	0.000	0.892	0.907
Modal	7	0.060	0.007	0.000	0.899	0.908
Modal	8	0.048	0.000	0.021	0.899	0.928
Modal	9	0.045	0.024	0.001	0.923	0.929
Modal	10	0.038	0.001	0.006	0.924	0.935
Modal	11	0.037	0.002	0.000	0.926	0.935
Modal	12	0.035	0.001	0.002	0.927	0.937

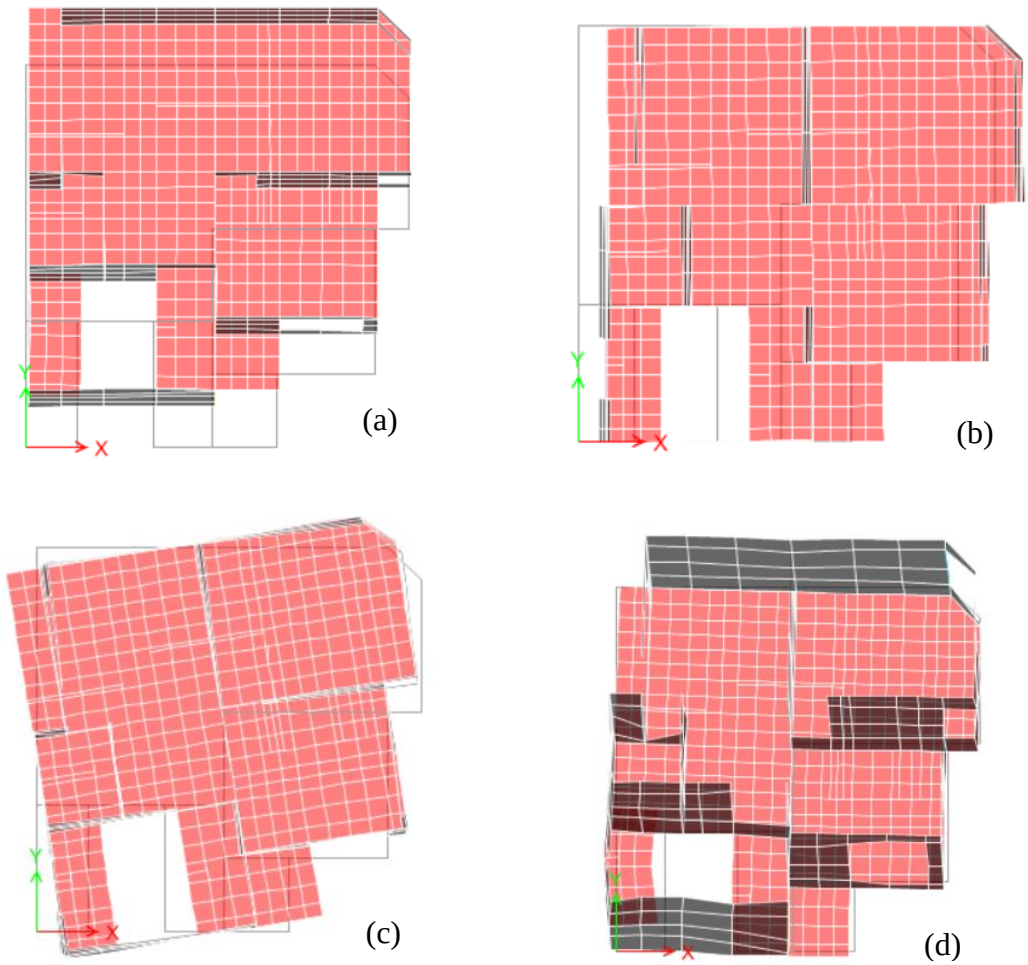

Figure 5.3 Plan views of first four mode shapes of the finite element model of the building obtained from ETABS 2017 with spring support at base. (a) First mode shape of the building dominant on direction along y-axis. (b) Second mode of the building dominant on direction along X-axis. (c) Third mode shape of the building in torsion. (d) Fourth mode shape of the building dominant on direction along Y-axis.

5.4 Results

The results of the modal analysis obtained from two different models show that there is substantial difference between the natural period and mass participation. Frequencies of the first four major modes of the building (two on each direction) model with and without soil springs are compared with those obtained from the Welch spectral method and the N4SID method in Table 5.4. Mode number and direction on table represents corresponding number of mode and period of the building along corresponding direction. For example, 0.226s (Mode 1, ch-2) on table represents period obtained from finite element model for first mode of vibration along direction Y-axis (direction of channel 2) for model with boundary condition pinned at support. Mode 1 and mode 4 of both the models have major mass contribution along direction Y-axis which is compared with result obtained for N4SID method for mode 1 and mode 2 for data measured along channel 2. Similarly, periods of mode 2 and mode 5 of both finite element model is compared with result

obtained for N4SID method for mode 1 and mode 2 for data measured along channel 1. Third mode of the finite element model is torsional in nature and has mass participation less than 1% in both the direction. Hence, this mode is insignificant and is ignored. Welch spectral method was used to identify only the first mode of vibration and the results from this method is compared with the finite element mode that has highest mass participation along the corresponding direction.

As seen from Table 5.4, there is a substantial difference between the natural periods evaluated from the two finite element models. When the structure is assumed to be built on rigid soil, the estimated vibration periods are lower than those identified from ambient measurements. This is a result of a FEM that is stiffer than the actual structure by virtue of ignoring the flexibility of the soil. After properly modelling the soil flexibility, the vibration periods of the FEM are very close to those identified from ambient measurements. This shows that modelling soil flexibility is very important for accurate dynamic characterization of buildings built on alluvial deposits. When the properties of the underlying soil are available, such modelling is relatively straightforward. However, relevant geotechnical information is often lacking, in which cases, modelling the soil becomes challenging. In such cases, system identification using ambient measurements can be used to calibrate the finite element model.

Table 5.4 Natural periods estimated from ambient vibration measurement and finite element model using ETABS 2017.

FEM rigid soil	FEM flexible soil	Welch spectral method	N4SID method
0.226s (Mode 1, ch-2)	0.275s (Mode 1, ch-2)	0.292s (ch-2)	0.264s (Mode 1, ch-2)
0.207s (Mode 2, ch-1)	0.259s (Mode 2, ch-1)	0.289s (ch-1)	0.266s (Mode 1, ch-1)
0.074s (Mode 4, ch-2)	0.080s (Mode 4, ch-2)		0.143s (Mode 2, ch-2)
0.070s (Mode 5, ch-1)	0.075s (Mode 5, ch-1)		0.078s (Mode 2, ch-1)

6 Seismic analysis

This chapter discusses the main results obtained from seismic analysis performed on the case study building. Finite element model created in ETABS 2017 from chapter 5 will be used for analysis. Response of the building to strong ground motion recorded in Kathmandu Valley during the 25th April 2015 Gorkha Earthquake is evaluated using numerical methods. In addition, properly scaled response spectra from Indian standards IS 1893 (part 1): 2002 and Eurocode 8 are also used to represent seismic action on the building.

6.1 Ground motion data

Nepal lies in the Himalayan region and is ranked as 11th most vulnerable country in terms of earthquake related hazards (UNDP 2004). The territory of Nepal spans about one third of the length of the Himalayan range. Because of its location in one of the most active tectonic zones, climate, topography, fragile geological structures and intense rainfall, Nepal is vulnerable to various types of natural disasters like earthquakes, landslides, mass movement, floods, etc. Among all the natural hazards, earthquakes are the most disastrous since their impacts can cover large areas causing deaths, injuries and destruction on massive scale. Out of 21 cities all over the world that lie in similar seismic hazard zones, Kathmandu city, the capital city of Nepal, is the first ranked in terms of earthquake impact on people.

The Gorkha earthquake of 25 April 2015 is the most recent devastating earthquake in Nepal since 1934 in terms of casualties and damage to properties in most of the country. The size of the earthquake was estimated to be magnitude 7.8 by USGS (USGS 2015) and local magnitude 7.6 by National Seismological Centre (NSC 2015). The epicenter of the earthquake is located about 77km North-West of Kathmandu, near Barpak village in the Gorkha district (USGS 2015). Several strong aftershocks followed the earthquake for months, four having magnitude higher than 6 which also included one with 7.3 magnitude. In this study, strong ground motion data recorded in Kathmandu valley during the mainshock will be presented and used as input for earthquake analysis for the case study building.

Figure 6.1 shows the location of five stations where the mainshock of 25 April Gorkha Earthquake was recorded. Four continuous recording accelerometers were installed in the Kathmandu Valley in 2011 as a collaborative study between Tribhuvan University and Hokkaido University (Takai et al. 2016). Those stations are marked with yellow triangles in the figure. The fifth station was installed by USGS (KATNP station) marked with black triangle. The station at KTP lies on rock site and all other stations lie on soft lake sediment of the valley (Takai et al. 2016). Figure 6.2 shows the plot of the acceleration data recorded at KATNP station. Baseline correction method is applied on raw data as stated in Rupakhety et. al (2010). Peak ground acceleration values for horizontal and vertical accelerations are marked in the figure.

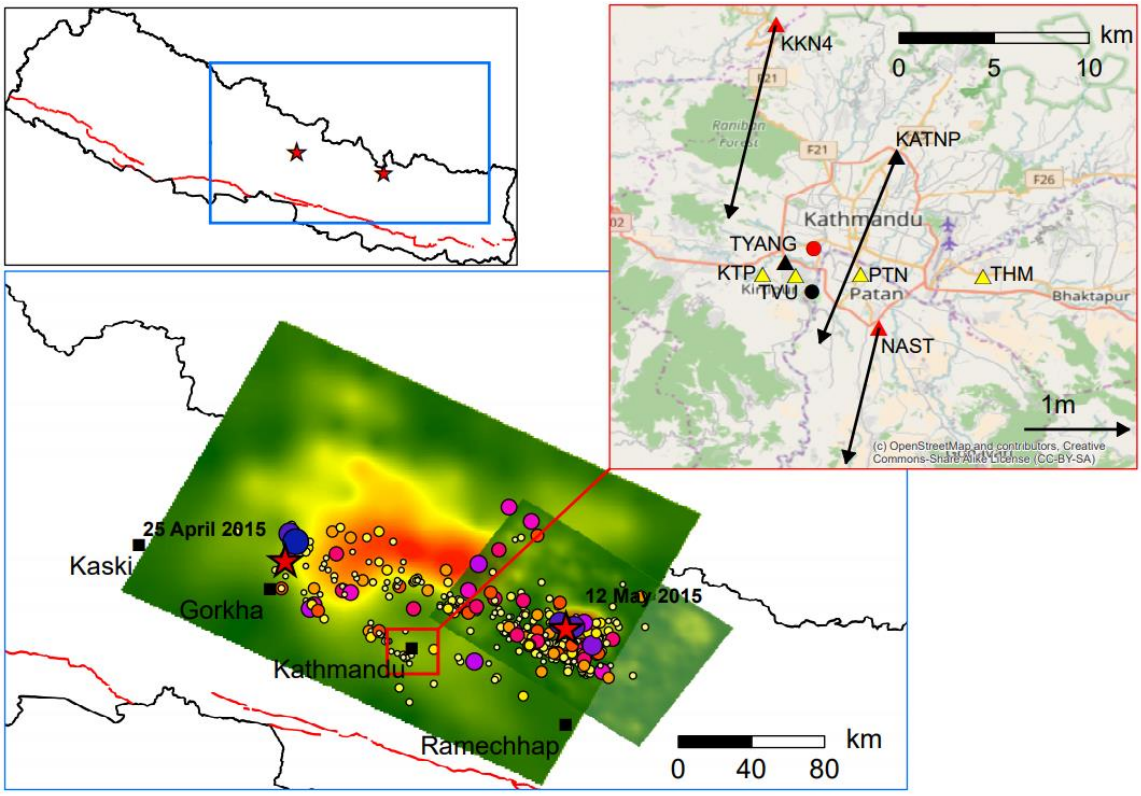

Figure 6.1 Top left map of Nepal showing the epicenter of the 25 April mainshock and the 12 May aftershock, the blue rectangle locates the area shown in the main figure. Main figure shows the epicentral area of the Gorkha Earthquake and its aftershocks. The circles represent aftershocks between 25 April and 18 June taken from NSC, their size is scaled with earthquake magnitude. The red rectangle represents the area around Kathmandu Valley, which is shown in detail in the insert map on top right. Top right area around Kathmandu showing the strong-motion station of USGS (KATNP) and the ones reported in Takai et al. 2016. (Source Rupakhety et al. 2017).

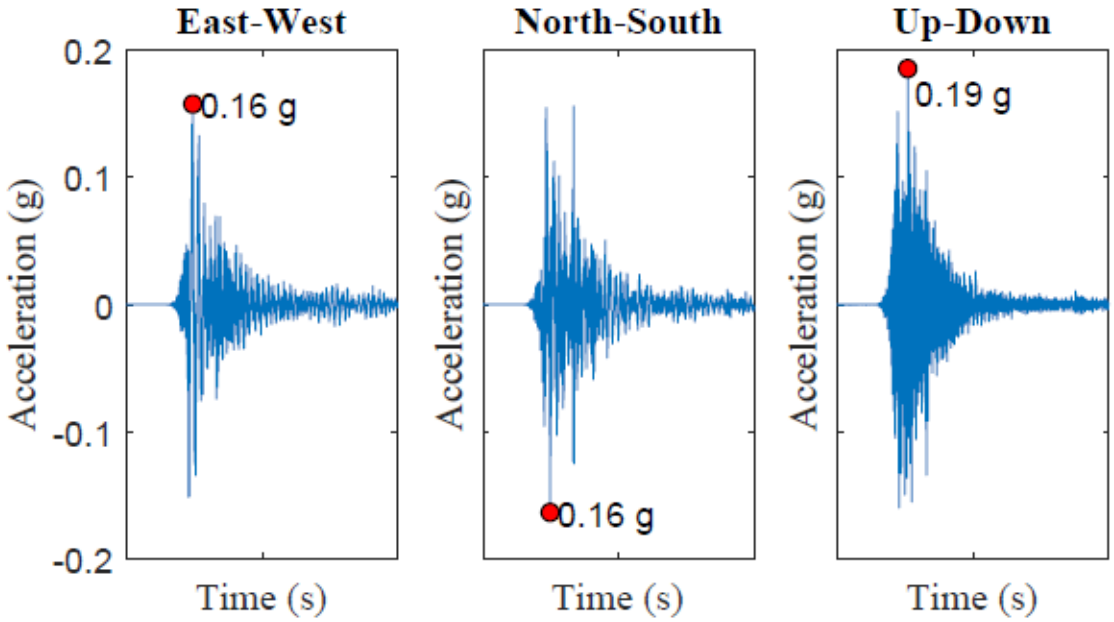

Figure 6.2 Acceleration time histories of mainshock ground motion recorded at KATNP station during the 25 April Gorkha Earthquake.

The 5% damped elastic response spectra of the mainshock horizontal motion recorded at the five different stations in the Kathmandu valley are presented in Figure 6.3. Vertical response of the recorded motion is not included in this study. Response spectra at KTP site, which lies on bedrock site, is very different from spectra at other sites on alluvial deposits or soft site. The horizontal response spectra from softer sites (THM, TVU, PTN and KATNP) are fairly similar in both directions. However, the response spectrum at TVU station has higher and border plateau compared to other three soft sites. The shape of the response spectra on soft sites contains unusually high amplitudes at longer period (around 5s). This can be seen on both directions. It shows that at soft site high frequency motion got damped and long period motion got amplified. In contrary to this, at rock site, spectra peaks around a period of ~0.25s (see PSA for KTP in E-W direction). It is to be noted that the fundamental period of the case study building is around close to 0.25s.

Peak ground acceleration or PGA for both horizontal direction motion is tabulated in Table 6.1. The horizontal PGA values at the soft sites are smaller compared to rock site. TVU station which is also located near the south-western edge of the valley closer to rock site has higher PGA for horizontal ground motion. Three stations at soft site (THM, PTN and KATNP) have similar values of PGA for both horizontal directions.

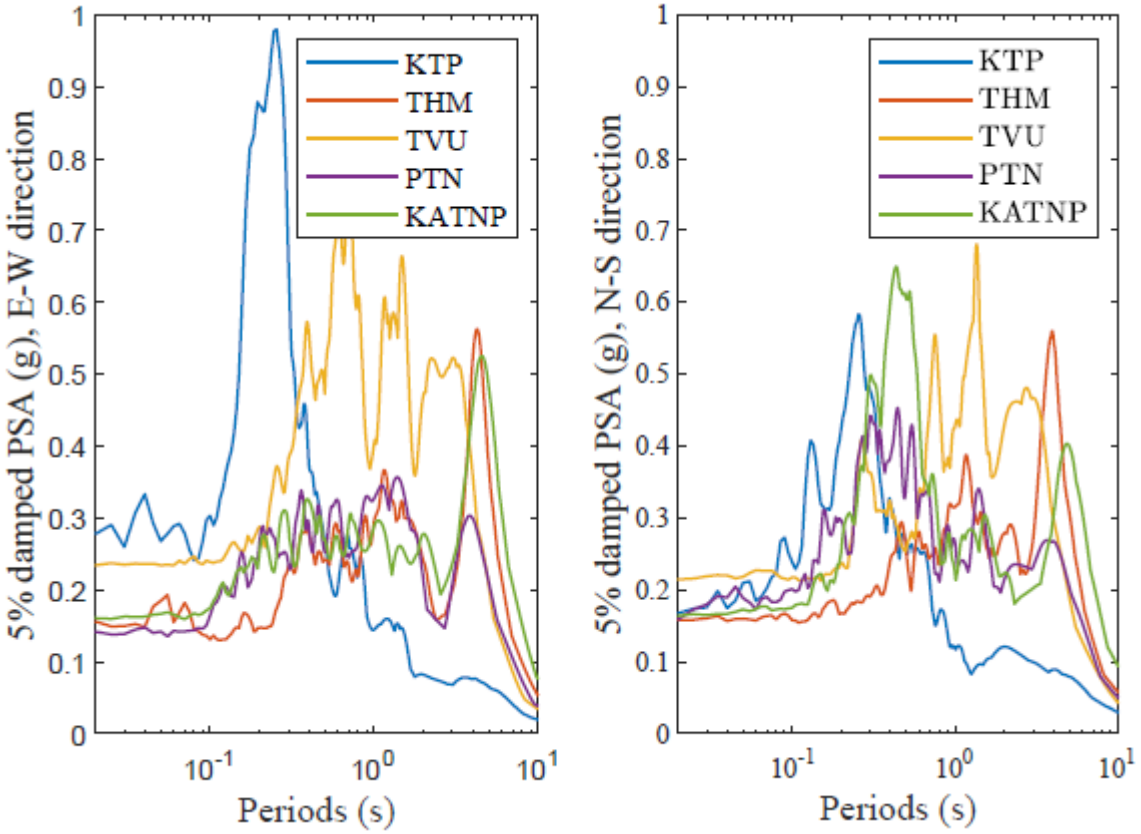

Figure 6.3 Five percent damped pseudo-spectral acceleration of mainshock motion of 25th April Gorkha earthquake at five stations in Kathmandu valley.

Table 6.1Peak ground acceleration of the mainshock ground motion on horizontal direction recorded at five different stations in Kathmandu valley.

Station	PGA (g) E-W	PGA (g) N-S
KTP	0.27	O.16
THM	0.15	0.15
TVU	0.23	0.21
PTN	0.14	0.15
KATNP	0.16	0.16

6.2 Input strong ground motion

For seismic analysis of the case study building ground motion is divided into two categories based on site. Ground motion recorded at stations THM, PTN and KATNP are categorized as ground motion representing soft site similar to the site of the case study building. Horizontal ground acceleration recorded from these three stations are used as input ground motion for time history analysis. For response spectra analysis mean of 5% damped pseudo-spectral acceleration is selected. As a comparative analysis, response spectra from Eurocode 8 (EC8) and Indian standards IS 1893 (part 1): 2002, hereafter called as IS, are used. EC8 elastic response spectrum corresponding to site class D (similar to soft soil site), scaled with mean PGA of the recorded ground motions and response spectrum from Indian standards IS for soft soil site scaled with mean PGA of recorded ground motion are also used for response spectral analysis. The response spectra are shown in Figure 6.4. The figure shows that scaled response spectrum from EC8 and IS captures the overall shape of response spectra of the horizontal motion of mainshock for lower vibration periods (less than 1s). However, response at longer periods which was recorded to be unusually high due to soft soil conditions is underestimated by the EC8 and the IS models.

Ground motion recorded at station KTP and TVU are categorized as rock site motion. Even though these ground motions do not represent the site condition of the case study building, they are selected as an illustrative analysis to see performance of similar buildings at rock site for a similar earthquake. To make illustrative analysis simpler, only ground motion recorded at KTP station is used. For this analysis response spectrum computed from EC8 and IS are categorized as rock site with the same PGA as that recorded at the KTP station. All three-response spectra are plotted in Figure 6.5. The figure shows that the scaled response spectra from EC8 and IS do not capture the shape of response spectra for lower periods.

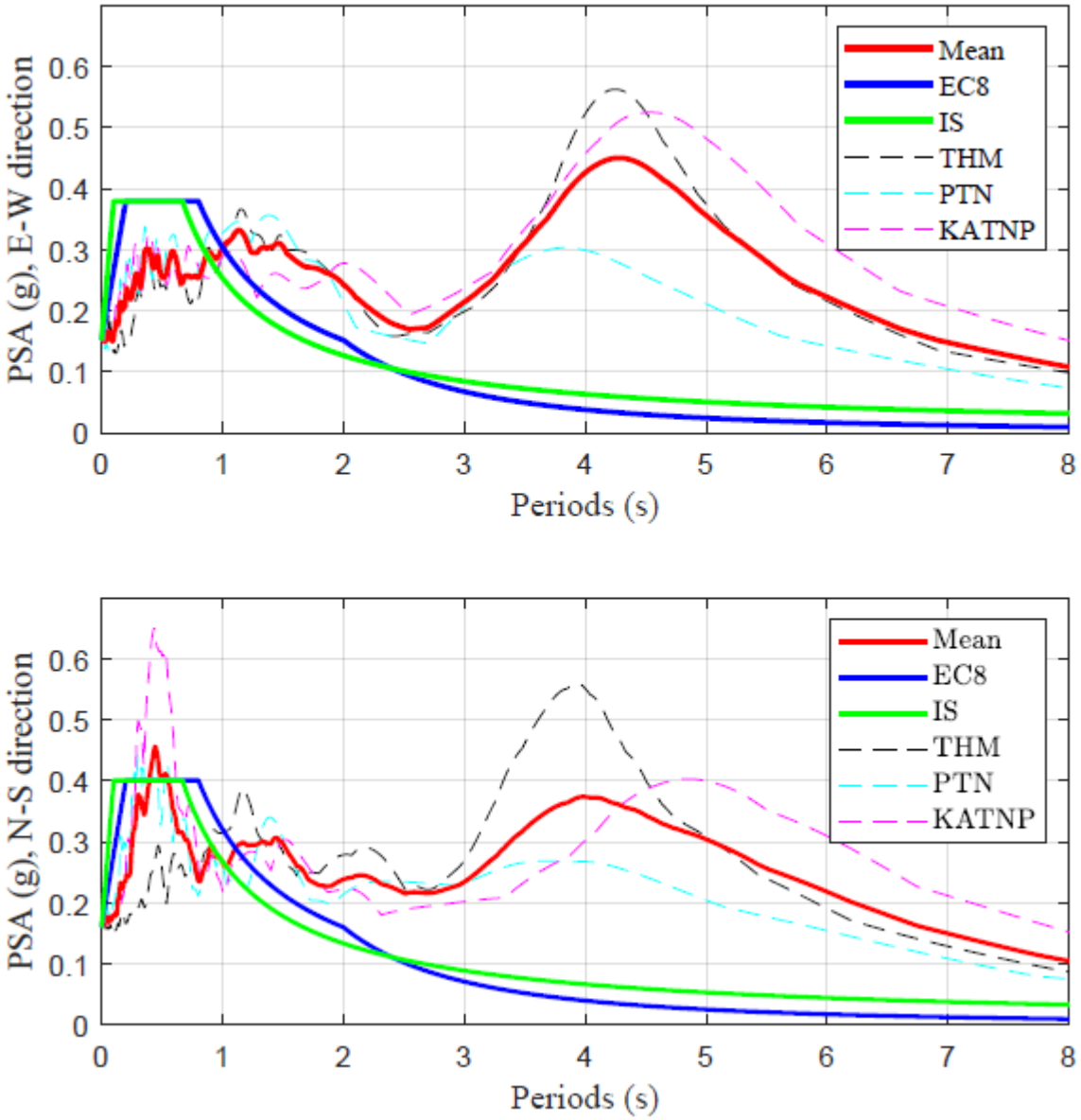

Figure 6.4 Five percent damped pseudo-spectral acceleration of mainshock motion of 25th April Gorkha earthquake recorded at stations THM, PTN and KATNP with mean spectrum (red line) with PGA scaled response spectrum from Eurocode8 and Indian standard IS 1893 (part 1): 2002.

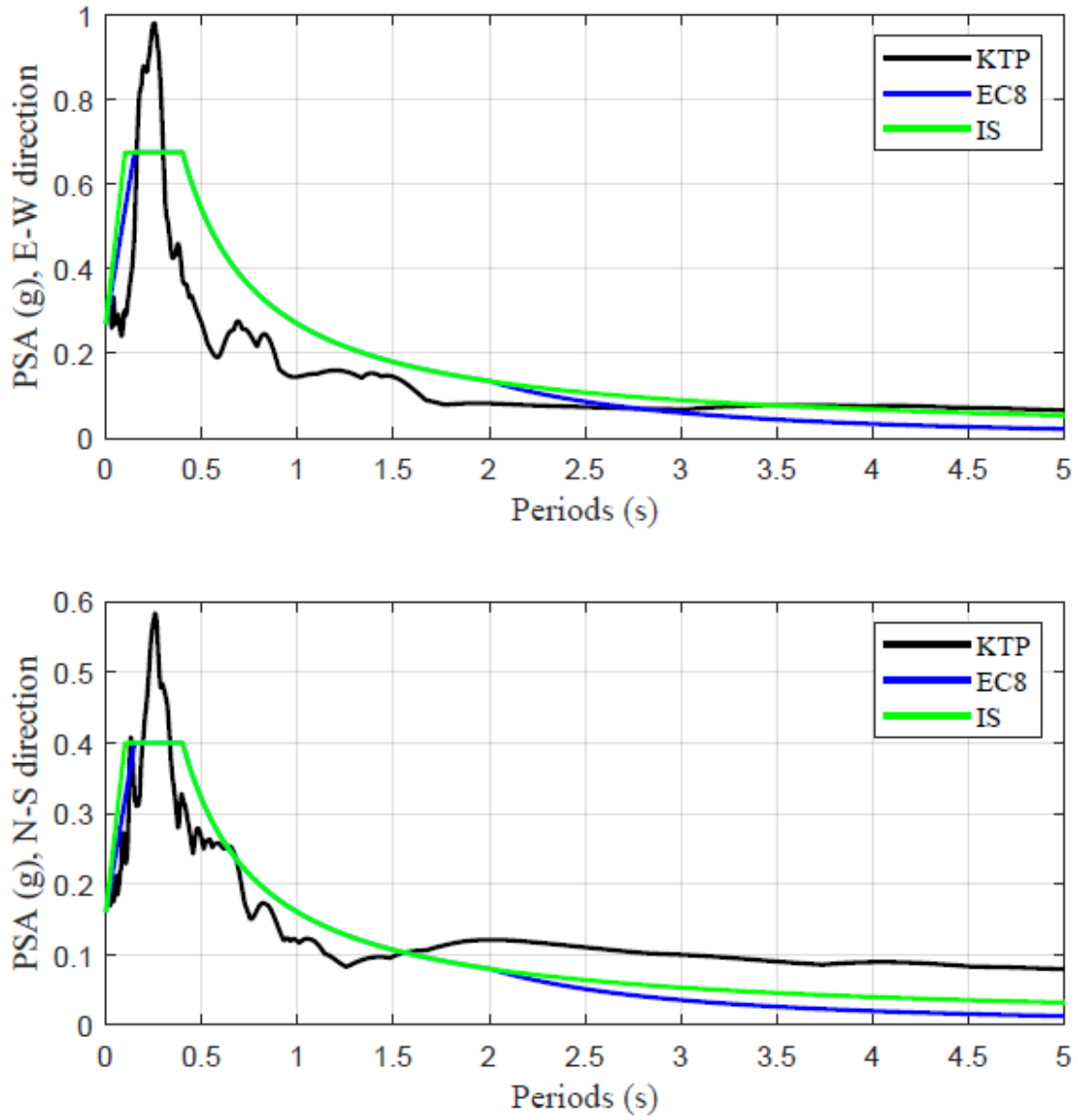

Figure 6.5 Five percent damped pseudo-spectral acceleration of mainshock motion of 25th April Gorkha Earthquake recorded at station KTP with PGA scaled response spectrum from Eurocode 8 and IS 1893 (part 1): 2002.

6.3 Results

Both time history analysis and response spectral analysis are performed in ETABS 2017 using bidirectional excitation. The seismic actions are represented by either the recorded ground motions or the response spectral models from the EC8 and IS. The east-west and north-south motion are applied along the X and Y axis of the FEM, respectively.

6.3.1 Base shear

Base shear and moment demand caused by ground motion recorded in soft sites are tabulated in Table 6.2. Base shear calculated from the response spectra of EC8 and IS are the highest in both the horizontal directions. The mean recorded spectra results in lower base shear than that from the EC8 and IS spectra. The mean of the maximum base shear obtained from time history analysis using the three ground motions is 706 kN, which is relatively close to that obtained from response spectral analysis using the mean PSA. The over-estimation of response by the EC8 and IS models can be justified as the plateau of their spectra is higher than that of all recorded ground motion in the X direction. At the fundamental period of the building (~0.26s) with 76% mass participation, the spectral ordinates of all the four records is smaller than that predicted by the EC8 and IS models. The same applies for the Y direction.

Table 6.2 Base shear and moment demand of the case study building estimated using finite element model on ETABS 2017 . Earthquake actions applied for this analysis are categorized as soft site.

Load case	Fx (kN)	Fy (kN)	Fz (kN)	Mx (kNm)	My (kNm)	Mz (kNm)
Dead	0	0	3668	16631	-13558	0
Live	0	0	516	2213	-1887	0
Time history PTN	727	1188	0	9340	5617	3813
Time history THM	524	612	0	4065	3647	4039
Time history KATNP	867	1152	0	8451	6212	5398
Mean of TH analysis	706	984	0	7285	5159	4417
Mean PSA	670	964	0	7636	5382	4477
EC8 PSA	1100	1202	0	9523	8867	6467
IS PSA	1107	1209	0	9526	8869	6503

Results obtained by using seismic action on buildings located at rock sites is presented next. For this, the ground motion recorded at KTP was used for time history analysis. In addition, response spectra of the ground motion as well as the spectral models of EC8 and IS codes scaled to the PGA of recorded motion at KTP were used. Base shear and moments calculated from time history analysis and response spectral analysis are shown in Table 6.3. Base shear demand from the ground motion at rock site is considerably higher than that from the soft sites presented above. This is because the ground motion at the rock site has a peak at a relatively low period (~0.25s) which is similar to the natural period of the building. For this case, the EC8 and IS code spectral models under-estimate the base shear demand caused by the recorded ground motion. It then appears that the recorded

ground motion had unexpectedly high energy at low periods (around 0.25s). However, one should be careful in making such interpretation based on a single record of ground motion.

Table 6.3 Base shear and moment estimated from response spectrum analysis for case study building using finite element model on ETABS 2017.

Load case	Fx (kN)	Fy (kN)	Fz (kN)	Mx (kNm)	My (kNm)	Mz (kNm)
Time history KTP Max	2281	1387	0	10741	19022	14371
KTP PSA	2777	1550	0	12309	22453	13698
EC8 PSA	1958	1207	0	9545	15738	9804
IS PSA	1965	1211	0	9546	15738	9828

6.3.2 Story drifts

Drift or lateral displacements of a structure are functions of various factors such as stiffness, applied external loads whether shear or flexure, confinement and shear span etcetera. It can be used for design and check of structure and can be correlated to the damage. Different code has specified damage limitations requirement based on inter story drift ratio. For example, inter story drift limitation specified on IS 1893 (part 1): 2002 (2002) is 0.004 times the storey height. Similarly, limitation specified on Eurocode 8 can be expressed as,

$$\frac{dr}{h} \leq \frac{\alpha}{\upsilon} \qquad (6.1)$$

Where, d_r is the difference of lateral displacements between two adjacent floors and h is the height of the floor. Damage limitation criteria based on structure type is given by three categories of α. For buildings having non-structural elements of brittle material (similar to masonry wall) attached to the structure has α value of 0.005. Similarly, υ is the reduction factor which considers the lower return period of the seismic action associated with the damage limitation requirement. For this analysis this value is assumed to be 1. Many researchers have published relation between inter story drift and various damage states on structures. Ghobarah (2004) presented maximum inter story drift limits corresponding to various damage states for ductile moment resisting frame (MRF) which is presented in Table 6.4. These limits are used as reference values for inter story drifts to study the performance of the case study building.

Figure 6.6 shows the plot of inter story drift ratio of the case study building in both horizontal directions. The first row corresponds to response spectral analysis and the second one to time history analysis. Red and blue line on each plot represents drift on direction east-west (along X-axis of model) and north-south (along Y-axis of model) respectively. Black dashed line on the plot is 0.2% drift ratio line for light reparable damage for MRF with infills (Ghobarah 2004). Green and cyan color dashed line on plot represents the damage limitation requirement specified on EC8 and IS 1893 (part 1): 2002 respectively. The results show that the drift demand on the structure during the 2015

Gorkha Earthquake was well within the specified limits. This shows that the structure should not suffer damage when excited by similar levels of ground motion, which was the case during the 2015 Gorkha Earthquake.

Table 6.4 Drift ratio (%) limits associated with various damage levels (Source: Ghobarah (2004))

State of damage	Ductile MRF	Nonductile MRF	MRF with infills	Ductile walls	Squat walls
No damage	<0.2	<0.1	<0.1	<0.2	<0.1
Repairable damage					
a) Light damage	0.4	0.2	0.2	0.4	0.2
b) Moderate damage	<1.0	<0.5	<0.4	<0.8	<0.4

A notable characteristic of inter story drift distribution is that a well-designed moment resisting frame building should have a uniform inter story drift distribution along its height. Which means, the inter story drift for each story should be similar. For example, poorly designed structures with soft stories shows higher drift on such stories and vulnerable for damage. Inter story drift distribution of the case study building shows similar drift ratio on all floors with minor differences.

Figure 6.7 shows the inter story drift ratio from earthquake actions categorized at rock site. Top two plot on figure shows the inter story drift ratio obtained from time history analysis and 5% damped response spectra estimated from horizontal ground motion recorded at KTP station. The drift ratios caused by rock ground motion are about twice that caused by ground motion recorded on soft soil and is close to the light repairable damage state specified in Ghobarah (2004). Hence it can be concluded that low-rise buildings of similar structural characteristics, which are abundant in Kathmandu and located at rock sites might have suffered more damage than similar buildings located in soft sites. This conclusion, however, does not take into consideration secondary effects caused by foundation failure.

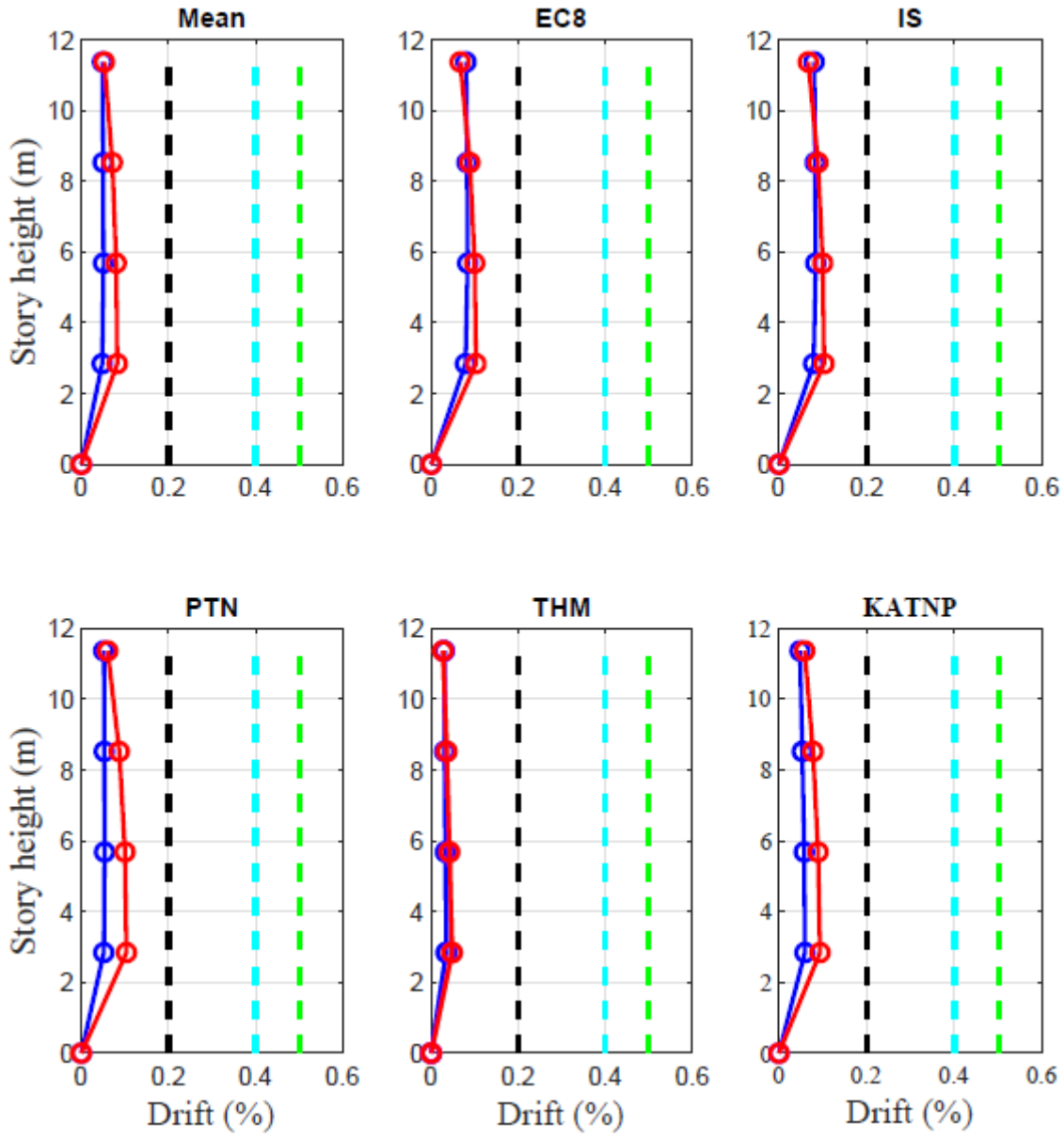

Figure 6.6 Story drift for each earthquake action in both horizontal directions. Blue and red lines correspond to X and Y directions, respectively. Green and cyan dashed lines represent story drift limitation specified by EC8 and IS 1893 (part 1): 2002 (2002), respectively. Black dashed line represents drift limit for repairable damage state specified by Ghobarah (2004).

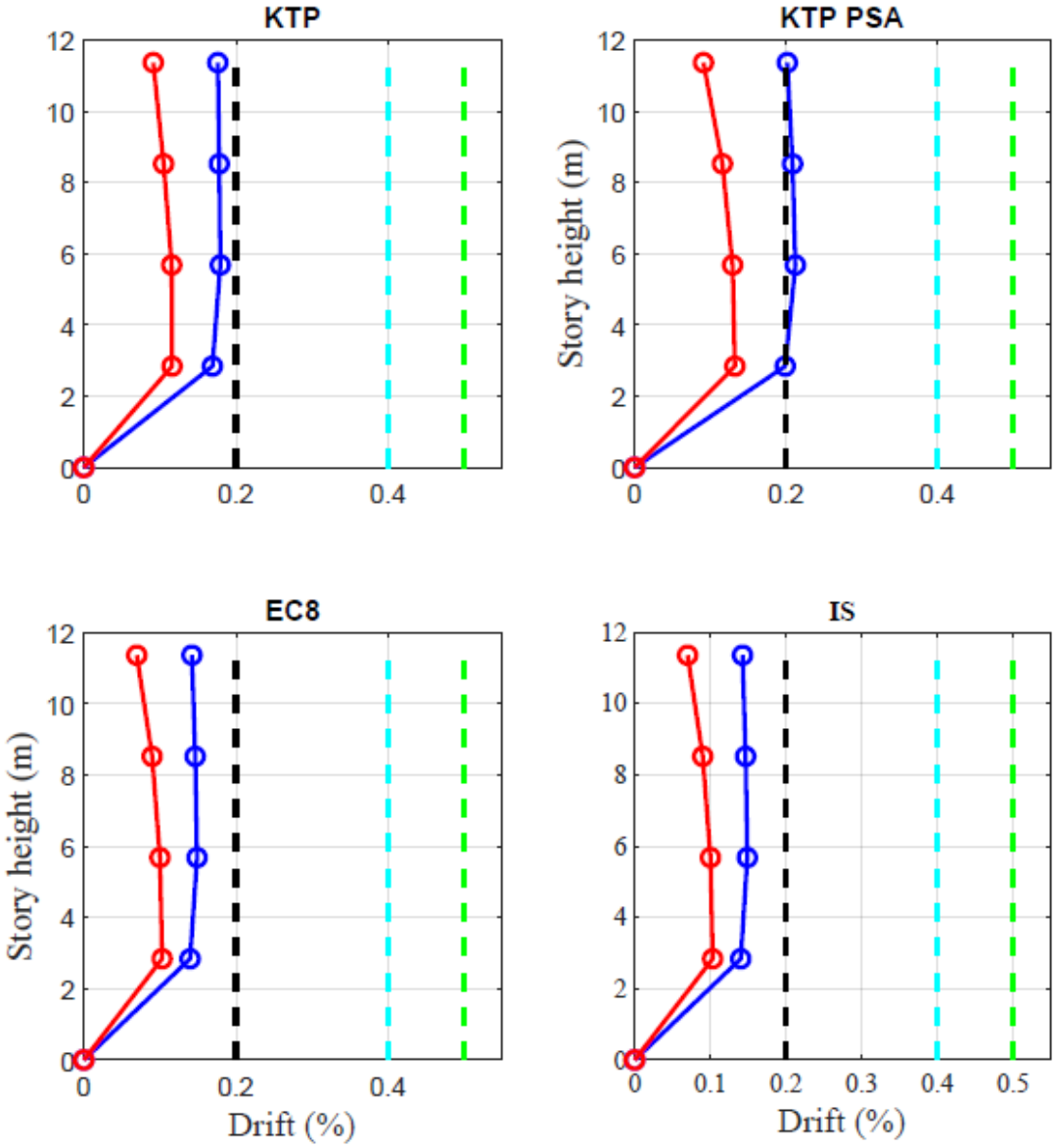

Figure 6.7 Story drift for case study building estimated from earthquake actions categorized as rock site. Figure on first row shows the story drift obtained from response spectra and time history analysis using ground motion recorded at KTP station. Figure on second row shows the story drift obtained from elastic scaled EC8 response spectra and scaled IS 1893 (part 1): 2002(2002) response spectra respectively. (See Figure 6.6 for definition of lines).

6.3.3 Structural integrity of building

The structural configuration of the case study building consists of moment resisting frame as the primary structure. Infill masonry walls in the building provides some additional stiffness to the building and contributes to the lateral load resistance for seismic actions. Hence contribution of the masonry walls for lateral load resistance cannot be ignored. However, as the lateral deformations increases, the brittle and weak masonry infill is no longer capable of carrying the increased load. This leads to increased demands on the frame elements. Structural integrity of the building when subjected to the ground motions

of the 2015 Gorkha Earthquake recorded in Kathmandu Valley is investigated in this section.

Moment curvature analysis of beams

To study the performance of beams under various earthquake actions moment curvature (M-ϕ) analysis is performed. Moment curvature analysis derives the curvature of beam associated with different values of moments for a cross section based on strain analysis and principle of equilibrium of forces. Figure 6.8 shows the plot of moment curvature diagram for beam specified in section 3.2 (Beam of size H355xB230 of M15 concrete). Accurate plot of bending moment and section curvature relationship of reinforced beam is a reliable indicator to access the performance of structure under seismic load. The failure behavior of concrete beam can be divided into stages based on bending moments. At first stage concrete beam behaves as elastic material. Increase in bending moment leads to tensile yielding of concrete. After reaching the tensile strength a crack in concrete appears and spreads with increase of bending moment. This leads to reduction of moment of inertia of section and yielding of tension reinforcement of the beam. After this stage concrete beam continuously loses its strength for further increase in bending moment and leads to collapse. Notable feature of the moment curvature diagram is that it depends upon axial force on the beam which provides additional compression or tension to the cross-section. Moment curvature diagram in Figure 6.8 was estimated for axial compression force 40kN obtained from load combination 1.5DL+1.5EL (DL= dead load and EL= Earthquake load) for the highlighted beam (see red color) on slab above first floor. This beam carries largest internal forces compared to other beams and was thus selected for analysis. Earthquake action selected for resulting axial force is response spectra estimated from IS 1893 (part 1): 2002 which gives highest axial force for predefined load combination. This load combination considers 150% of total dead load of building and 150% of full horizontal earthquake action for both horizontal directions. The results show that that the yielding moment of the beam is ~45kN-m, corresponding to first yielding of reinforcement bars. Similarly, ~51kN-m is moment for which ultimate concrete strain is reached in extreme compressive fiber.

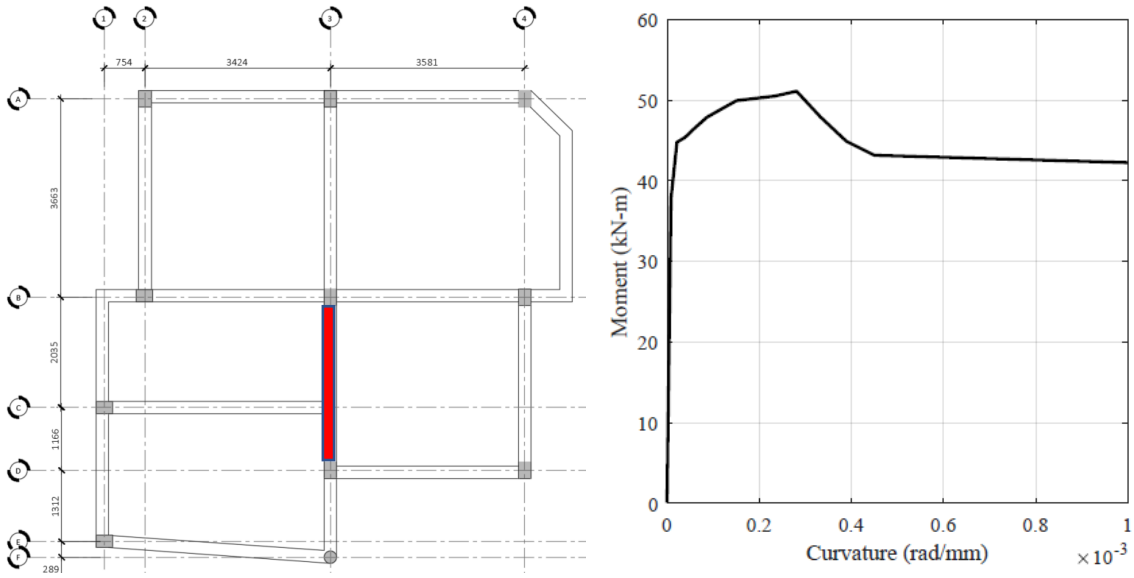

Figure 6.8 Left: the structural layout of case study building with arrowhead pointing to the beam used for integrity check. Right: moment curvature diagram of the selected beam.

Table 6.5 shows the absolute maximum moment on selected beam obtained from different earthquake actions categorized as soft site and rock site. The moment demands on the beam are within its yield capacity for ground motion categorized as soft site. Hence, it can be concluded that the beams of the building remained elastic during the ground shaking.

Rock site earthquake analysis result shows higher bending moment on the selected beam compared to soft site as expected. 5% damped response spectra analysis using recorded ground motion gives highest bending moment on beam compared to other actions. This moment is more than ultimate limit state moment derived from moment curvature diagram. It is also notable that moment curvature diagram is derived for 40kN of axial force which is higher for these earthquake actions. Higher axial force (compression) results less moment capacity in the beam.

Table 6.5 FEM analysis result of maximum bending moment on selected beam from each earthquake action categorized as soft site.

Category	**Load combination 1.5DL+1.5EQ**	**Mmax (kN-m)**
Soft site	IS PSA	42
	EC8 PSA	42
	Mean PSA	36
	THM time history max	21
	KATNP time history max	39
	PTN time history max	43
Rock site	IS PSA	50
	EC8 PSA	50

	KTP PSA	57
	KTP time history max	41

P-M interaction of columns

Structural integrity of the columns can be checked from axial force and bending moment interaction diagram (P-M diagram). Figure 6.9 shows the P-M interaction diagram derived for rectangular column section described in section 3.2 about its strong axis. The formulas used for derivation of interaction diagram is specified in IS 456: 2000 under section 38 and 39. If the combination of axial force and bending moment of a column lies within the interaction envelope, the column capacity is assumed to be adequate; if the point falls outside the interaction envelope, the column is overstressed. This interaction diagram is developed considering the partial safety factor on material properties. Hence, this can be taken as a design envelope for column. The column being analyzed is marked with an arrow in Figure 6.9.

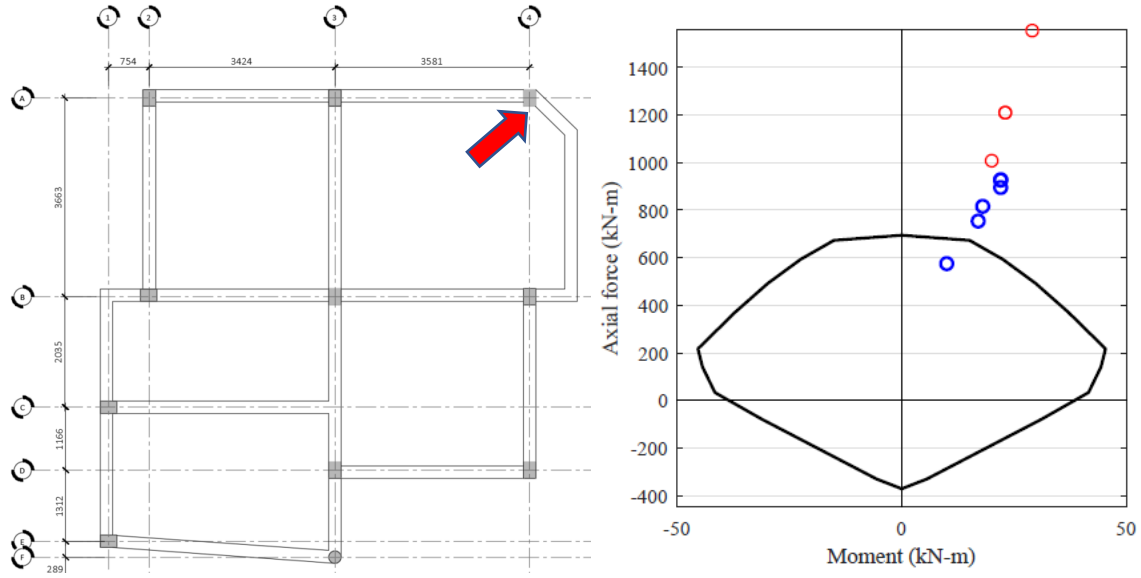

Figure 6.9 Leftt: structural layout of the case study building with arrowhead pointing to the column selected for P-M interaction analysis. Right: P-M interaction curve of the selected column considering partial safety factors on material properties. Blue and red marker represents moment and axial force demand from earthquake actions categorized as soft site and rock site respectively for selected load combination.

Among different load combinations, combination 1.5DL+1.5EL results are tabulated in Table 6.6 for different earthquake actions. Result shows that axial force and moment obtained from response spectra analysis for ground motion categorized as soft site falls outside of the interaction envelope. Result obtained from time history analysis shows similar behavior except at the THM station. Hence, it can be concluded that the columns in the building do not confirm to design standards for the level of PGA recorded at soft soil sites during the Gorkha Earthquake.

For earthquake action at rock sites, the results lie well outside the interaction envelope.

Table 6.6 Maximum moment and maximum axial force on selected column for different earthquake actions.

Category	Load combination 1.5DL+1.5EQ	Mmax (kN-m)	Pmax (kN)
Soft site	IS PSA	22	927
	EC8 PSA	22	927
	Mean PSA	17	754
	THM time history max	10	575
	KATNP time history max	18	816
	PTN time history max	22	895
Rock site	IS PSA	23	1210
	EC8 PSA	23	1210
	KTP PSA	29	1555
	KTP time history max	20	1008

Seismic conceptual design of RC framed building requires frame structures to have certain properties in structural configuration for seismic resistance. One of these requirements can be stated as strong column- weak beam concept. Such a design allows yielding of beams while the columns remain elastic thereby providing stability and strength. Such a configuration results in, even in extreme shaking, more favorable failure mechanism than when columns fail before beams. The design of beams and columns in the case study building seems to violate this principle of strong column and weak beam. Analysis of beam and columns from above shows that for the same earthquake action, columns are overstressed while beam remains elastic (result for soft soil site analysis). This result matches with damage and failure modes found in RC framed building in Kathmandu valley during the 25 April Gorkha Earthquake (for example see Varum et al. 2018). Many buildings suffered from column damage with development of plastic hinge to complete collapse. The columns of the case study building should have, in theory, suffered minor damage if the action was as strong as would be implied by the response spectra of IS. However, the results from time history analysis showed lower demands that from the response spectral analysis. Even in this case, some of the recorded ground motions would cause the columns to be over-stressed. However, no visible damage was observed in the columns of the building after the earthquake

7 Discussion and conclusions

7.1 Synopsis of the study

This thesis starts with a brief introduction to structural health monitoring with importance of structural system identification. The focus of the first part of thesis is on system identification, which is the process of identifying the dynamic properties of a structure by using recorded ambient vibration. Brief introduction to two types of system identification namely parametric and non-parametric methods with different models on each type are discussed. These models are then applied in a simulated example of SDOF system and MDOF system with known inputs and known output. System identification methods are then used to identify the vibration period and damping ratios which are compared with their actual values. These exercises provided illustrative background of the methodology used in this thesis and helped establish and verify algorithms to be used in the case study.

Practical implication of different models of system identification are presented in later part of thesis with the help of a case study building. The case study building is a four-story RC framed residential building located in Kathmandu, Nepal. Structural configuration of the building, characteristics of infill masonry and soil conditions at the site are examined and presented. Three accelerometers were installed in the building in order to record ambient vibration of the three floors. These ambient vibrations recorded in building were used to evaluate natural periods and critical damping ratios of the fundamental modes of vibration of the building.

Finite element model of the building was created on ETABS 2017 and updated with the periods identified from ambient measurements. The main update was in regard to modelling the flexibility of the soil. Based on available geotechnical data from nearby sites, properties of springs to model soil flexibility were calibrated. These soil springs were incorporated in the finite element model. Eigen analysis of the finite element models with and without soil flexibility were conducted and the periods of vibration were compared with those obtained from system identification. It was found that the model with the soil springs had the same vibration frequencies as those obtained from system identification.

Finally, earthquake analysis of the case study building was carried out using the finite element model with soil springs. Ground motion recorded at different sites on Kathmandu valley for 25 April Gorkha earthquake were selected for analysis. In addition to recorded ground motion, PGA scaled elastic response spectra from EC8 and response spectra defined on IS 1893 (part 1): 2002 were used. Results of earthquake analysis in terms of base shear, story drift and structural integrity were presented and discussed.

7.2 Interpretation of the results

Welch spectral method and sub state space model N4SID method was used to estimate the natural period and damping of the case study building. Natural vibration period of the building estimated from non-parametric Welch spectral method is 0.292s and 0.289s the two orthogonal directions. These estimated values are slightly larger than vibration periods estimated from parametric state space N4SID method which are 0.266s and 0.264s. When it comes to damping ratios, the results obtained from N4SID algorithm was much less variable than that obtained from the half-power bandwidth method based on Welch's averaged PSD. Damping ratios estimated from N4SID method was 6.3% and 6.9% for first two modes, which are translations in the two principal horizontal directions of the building. The natural periods estimated from system identification technique were compared with those obtained from the FEM. The results from the system identification showed a good comparison to the modes identified from FEM having soil springs at the base of the model, whereas the FEM without soil flexibility was significantly stiffer than the real building. This shows that pinned support boundary condition for buildings on soft soil site does not fully describe the dynamic behavior of the structure. Also, it shows how important it is to consider structure soil interaction while doing numerical modelling of the structure. Since geotechnical data at nearby site was available, modelling the soil flexibility was straightforward, and the system identification results served only in verifying the model. In lack of geotechnical data, system identification can be used to calibrate the model, for example, by varying the property of the soil so that the eigen frequencies of the FEM matches the frequencies identified from experimental data, which in this case is ambient vibration record.

The 25 April Gorkha earthquake recorded at Kathmandu valley was used for earthquake analysis using FEM. Strong ground motion of the mainshock recorded at different places in Kathmandu valley shows different characteristics. Horizontal ground motion recorded at soft soil site shows two distinct peaks: narrow peak at low period ~0.4s and wider peak at higher period ~ 5s. The peaks were found to be quite different in north-south and east-west directions. However, ground motion recorded at rock site (KTP) shows very high peak at lower period ~ 0.25s with higher PGA. Peak of the response spectra is significantly larger than what is commonly adopted in design codes EC8 and IS 1893 (part 1): 2002 (Mainly for ground motion at rock site and N-S direction ground motion for soft site). That is why, result shows that, for the same levels of PGA, structures in Kathmandu valley mostly at rock site with fundamental period in the range of 0.3-0.4s were exposed to higher base shear demand than code specified response spectra. Similarly, at soft site, code spectra capture the overall shape of the mean recorded spectra for lower period (less than 1s). However, mean recorded spectra shows border and high peak at longer period which is not captured by code spectra. This tells us that taller building having higher periods at soft soil site were exposed to higher base shear demand than code specified response spectra.

A review of capacity and performance of main structural elements (beam and columns) was carried out using recorded ground motion and scaled response spectra from EC8 and IS 1893 (part 1): 2002. Beam and column performance during mainshock motion was checked using moment curvature diagram and P-M interaction diagram. Estimated beam bending moment at critical location of the building was well below yield moment when considering ground motion recorded at soft soil. However, ground motion recorded at rock sites caused much larger moment demand which was larger than yielding moment.

Verification of column using P-M interaction diagram shows that the columns would be overstressed by the ground motion recorded at both rock and soft sites. This shows that the seismic design principle of strong column and weak beam is violated in the design of the building. This is an important principle that ensures a more favorable collapse mechanism during strong shaking and is therefore vital for life safety. It then appears that design practice in Nepal should be improved to incorporate this design philosophy.

7.3 Future research

Further research on this subject could involve study of nonlinear behavior of RC framed structure and masonry walls of the building. As stated, masonry walls in building provides some additional stiffness to the building and contribute to the lateral load resistance for seismic actions. However, as the lateral deformations increases, the brittle and weak masonry infill is no longer capable of carrying the increased load. This effect is not taken into consideration in this study. Inelastic modelling of the building, and other similar buildings along with seismic analysis with different levels of ground shaking should be undertaken to better understand seismic vulnerability of similar buildings in Kathmandu.

8 References

Adhikari S. Structural dynamic analysis with generalized damping models: analysis. John Wiley & Sons; 2013 Dec 11.

Alvin KF, Park KC. Second-order structural identification procedure via state-space-based system identification. AIAA journal. 1994 Feb;32(2):397-406.

Alvin KF, Robertson AN, Reich GW, Park KC. Structural system identification: from reality to models. Computers & structures. 2003 May 1;81(12):1149-76.

Box GE, Jenkins GM, Reinsel GC, Ljung GM. Time series analysis: forecasting and control. John Wiley & Sons; 2015 May 29.

Chaulagain H, Rodrigues H, Jara J, Spacone E, Varum H. Seismic response of current RC buildings in Nepal: a comparative analysis of different design/construction. Engineering Structures. 2013 Apr 1;49:284-94.

Chopra AK. Dynamics of structures: theory and applications to earthquake engineering. Prentice-Hall; 2001.

Crisafulli FJ, Carr AJ. Proposed macro-model for the analysis of infilled frame structures. Bulletin of the New Zealand Society for Earthquake Engineering. 2007 Jun 1;40(2):69-77.

Crisafulli, F.J. (1997). Seismic Behaviour of Reinforced Concrete Structures with Masonry Infills, PhD Thesis, University of Canterbury, New Zealand.

Datta TK. Seismic analysis of structures. John Wiley & Sons; 2010 Mar 16.

De Luca F, Verderame GM, Gómez-Martínez F, Pérez-García A. The structural role played by masonry infills on RC building performances after the 2011 Lorca, Spain, earthquake. Bulletin of Earthquake Engineering. 2014 Oct 1;12(5):1999-2026.

Eurocode 8: Design of structures for earthquake resistance-part 1: general rules, seismic actions and rules for buildings. Brussels: European Committee for Standardization. 2005 Aug 14. Eurocode 8: Design of structures for earthquake resistance. Part. 2005 Apr 8;1:1998-.

Furtado A, Vila-Pouca N, Varum H, Arêde A. Study of the Seismic Response on the Infill Masonry Walls of a 15-Storey Reinforced Concrete Structure in Nepal. Buildings. 2019 Feb;9(2):39.

G Asteris P, P Giannopoulos I, Z Chrysostomou C. Modeling of infilled frames with openings. The Open Construction and Building Technology Journal. 2012 Oct 31;6(1).

Gautam D. Empirical correlation between uncorrected standard penetration resistance (N) and shear wave velocity (VS) for Kathmandu Valley, Nepal. Geomatics, Natural Hazards and Risk. 2017 Dec 15;8(2):496-508.

Ghobarah A. On drift limits associated with different damage levels. In Performance-Based Seismic Design Concepts and Implementation: Proceedings of the International Workshop, Bled, Slovenia 2004 Jun 28 (Vol. 28, pp. 321-332).

Guler K, Yuksel E, Kocak A. Estimation of the fundamental vibration period of existing RC buildings in Turkey utilizing ambient vibration records. Journal of Earthquake Engineering. 2008 May 14;12(S2):140-50.

Hendry AW, Sinha BP, Davies SR. Design of masonry structures. CRC Press; 2003 Sep 2.

Hermanns L, Fraile A, Alarcón E, Álvarez R. Performance of buildings with masonry infill walls during the 2011 Lorca earthquake. Bulletin of Earthquake Engineering. 2014 Oct 1;12(5):1977-97.

Indian Standard IS. IS 1786 - 1985: Specification for high strength deformed steel bars and wires for concrete reinforcement (3rd revision). New Delhi. 1992.

Indian Standard IS. IS 1893 (part 1): 2002: Criteria for earthquake resistant design of structures (5^{th} revision). New Delhi. 2002.

Indian Standard IS. IS 456: 2000: Plain and Reinforced Concrete. Code of Practice (4th revision). New Delhi. 2000.New Delhi. 2000.

Indian Standard IS. IS 875 (part 1) – 1987: Code of practice for design loads (other than earthquake) for building and structures (2^{nd} revision). New Delhi. 1987.

Indian Standard IS. IS 875 (part 2) – 1987: Code of practice for design loads (other than earthquake) for building and structures (2^{nd} revision). New Delhi. 2010.

Jenkins GM, Watts DG. Spectral Analysis and Its Applications, San Francisco: HoldenMDay; 1969

Ministry of Physical Planning and Works (1994). Nepal National Building Code (NBC 201): Mandatory Rules of Thumb Reinforced Concrete Buildings with Masonry Infill. Kathmandu. 2007.

Ministry of Physical Planning and Works (1994). Nepal National Building Code (NBC 109): Masonry-unreinforced. Kathmandu. 2007.

Murty CV, Jain SK. Beneficial influence of masonry infill walls on seismic performance of RC frame buildings. In 12th world conference on earthquake engineering 2000 Jan 30.

National Seismological Centre (NSC) (2015). http://www.seismonepal.gov.np/

Nepal disaster report 2017. Ministry of Home affairs (MOHA). Government of Nepal. 2017.

Papagiannopoulos GA, Hatzigeorgiou GD. On the use of the half-power bandwidth method to estimate damping in building structures. Soil Dynamics and Earthquake Engineering. 2011 Jul 1;31(7):1075-9.

Peeters B, De Roeck G. Stochastic system identification for operational modal analysis: a review. Journal of Dynamic Systems, Measurement, and Control. 2001 Dec 1;123(4):659-67.

Phaiju S, Pradhan PM. Experimental work for mechanical properties of brick and masonry panel. Journal of Science and Engineering. 2018 Aug 31; 5:51-7.

Rupakhety R, Halldorsson B, Sigbjörnsson R. Estimating coseismic deformations from near source strong motion records: methods and case studies. Bulletin of Earthquake Engineering. 2010 Aug 1;8(4):787-811.

Rupakhety R, Olafsson S, Halldorsson B. The 2015 Mw 7.8 Gorkha Earthquake in Nepal and its aftershocks: analysis of strong ground motion. Bulletin of Earthquake Engineering. 2017 Jul 1;15(7):2587-616. Söderström T, Stoica P (1989). System identification, Prentice Hall International, Cambridge.

Takai N, Shigefuji M, Rajaure S, Bijukchhen S, Ichiyanagi M, Dhital MR, Sasatani T. Strong ground motion in the Kathmandu Valley during the 2015 Gorkha, Nepal, earthquake. Earth, Planets and Space. 2016 Dec;68(1):10

United States Geological Survey (USGD) (2015). http://earthquake.usgs.gov/earthquakes/eventpage/us20002926#general_summary

Varum H, Dumaru R, Furtado A, Barbosa AR, Gautam D, Rodrigues H. Seismic performance of buildings in Nepal after the Gorkha earthquake. Impacts and insights of the Gorkha earthquake 2018 Jan 1 (pp. 47-63). Elsevier.

Varum H, Furtado A, Rodrigues H, Dias-Oliveira J, Vila-Pouca N, Arêde A. Seismic performance of the infill masonry walls and ambient vibration tests after the Ghorka 2015, Nepal earthquake. Bulletin of Earthquake Engineering. 2017 Mar 1;15(3):1185-212.

Welcome to Etabs2016. Computers and structures, Inc., 1978-20186. 2018,

Appendix A: SPT test result

Test results obtained from SPT tests are included here.

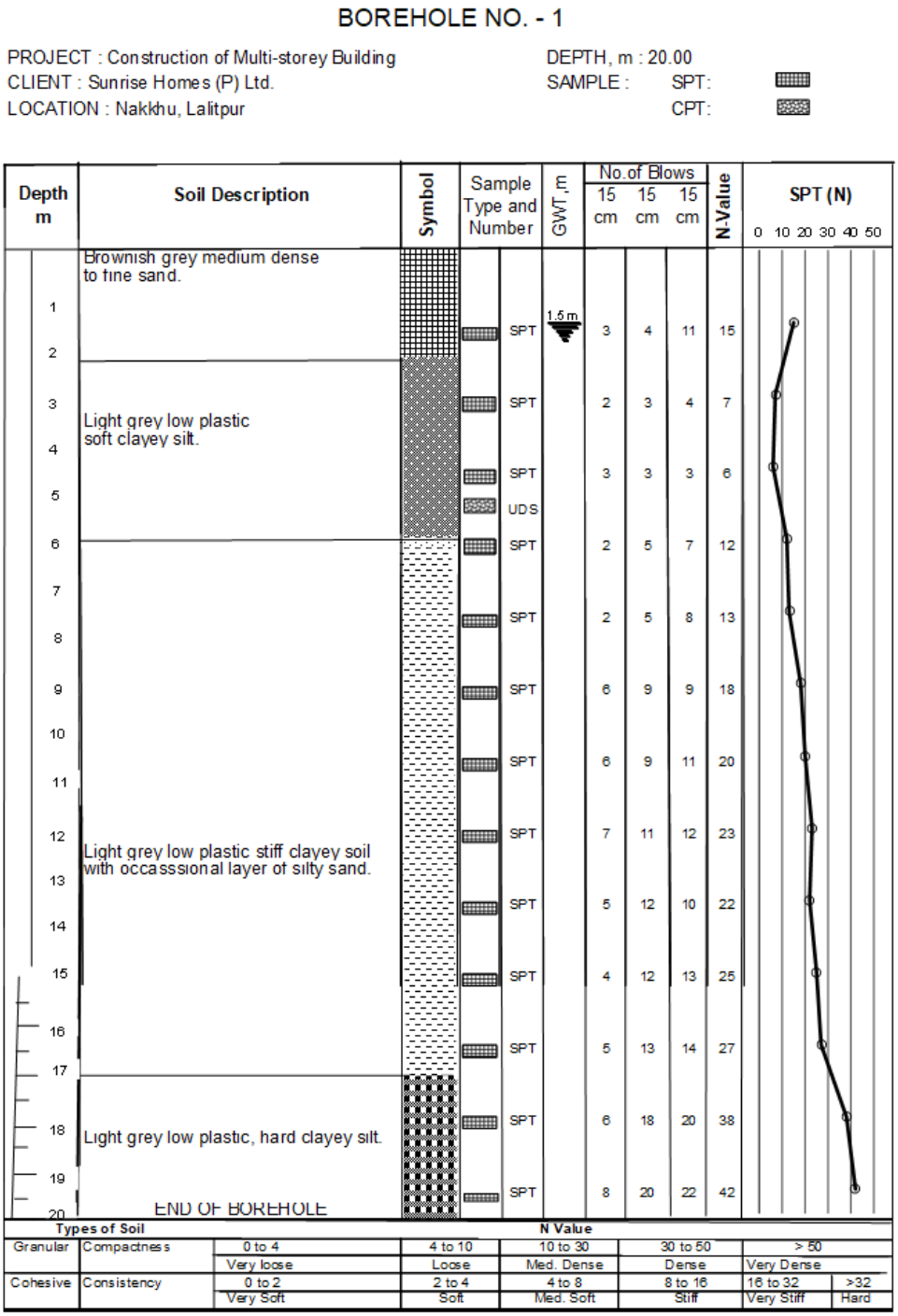

Figure A. 1 SPT test result conducted at borehole number 1.

BOREHOLE NO. - 2

PROJECT : Construction of Multi-storey Building
CLIENT : Sunrise Homes (P) Ltd.
LOCATION : Nakkhu, Lalitpur

DEPTH, m : 20.00
SAMPLE : SPT:
CPT:

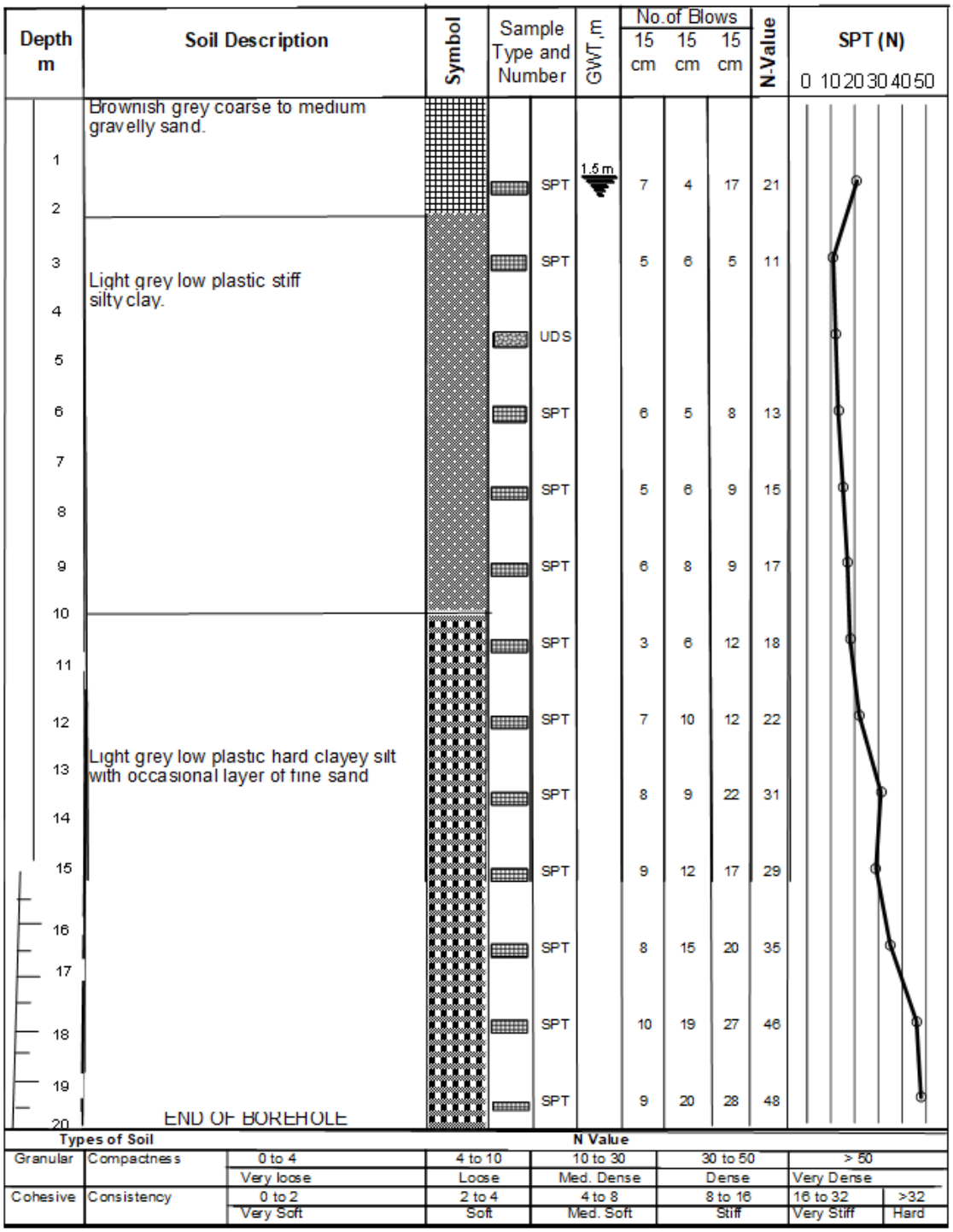

Figure A. 2 SPT test result conducted at borehole number 2.

BOREHOLE NO. - 3

PROJECT : Construction of Multi-storey Building
CLIENT : Sunrise Homes (P) Ltd.
LOCATION : Nakkhu, Lalitpur

DEPTH, m : 20.00
SAMPLE : SPT:
CPT:

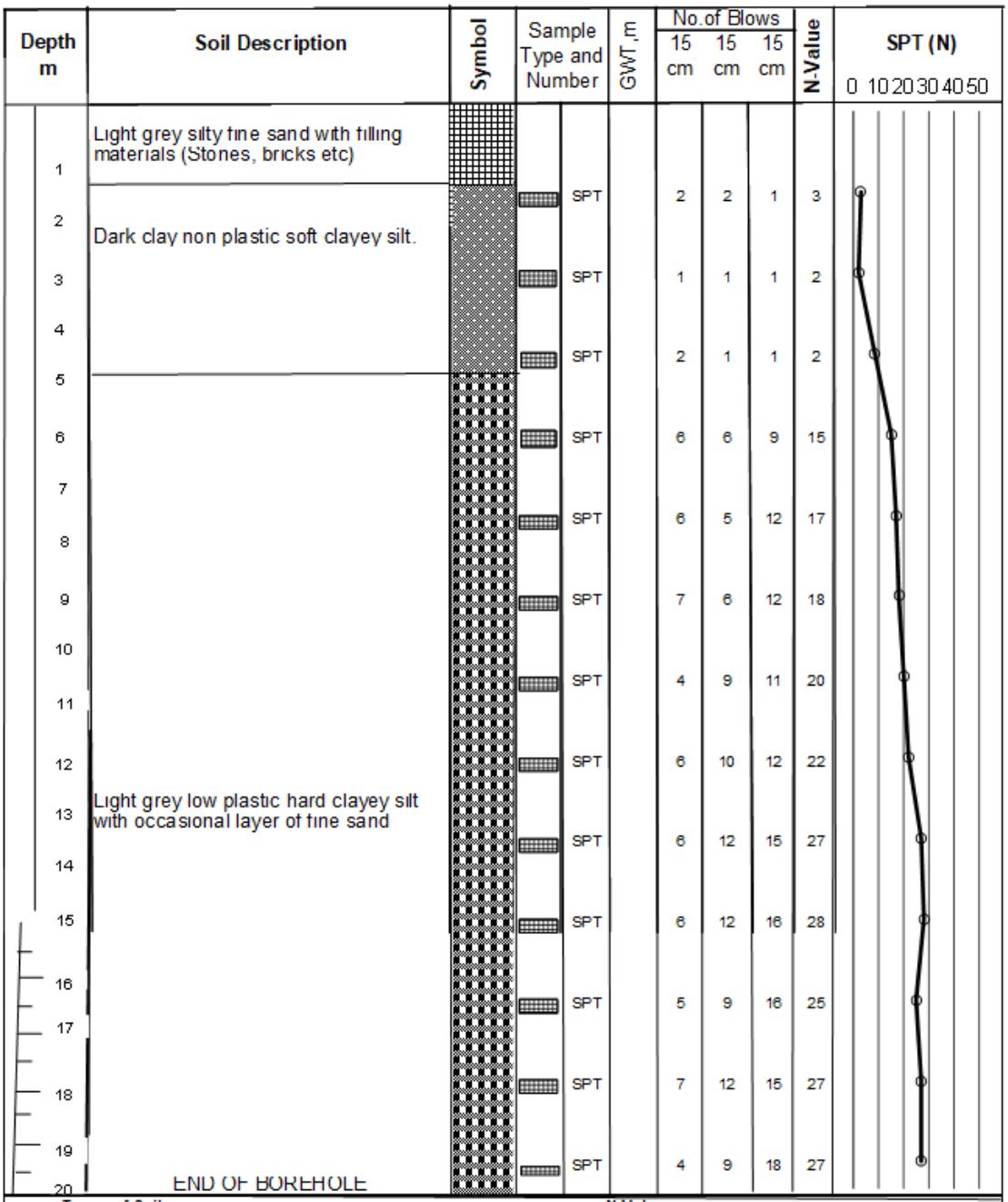

Types of Soil		N Value					
Granular	Compactness	0 to 4	4 to 10	10 to 30	30 to 50	> 50	
		Very loose	Loose	Med. Dense	Dense	Very Dense	
Cohesive	Consistency	0 to 2	2 to 4	4 to 8	8 to 16	16 to 32	>32
		Very Soft	Soft	Med. Soft	Stiff	Very Stiff	Hard

Figure A. 3 SPT test result conducted at borehole number 3.

Appendix B: Ambient vibration measurement

In this appendix ambient vibration measured on each floor are presented.

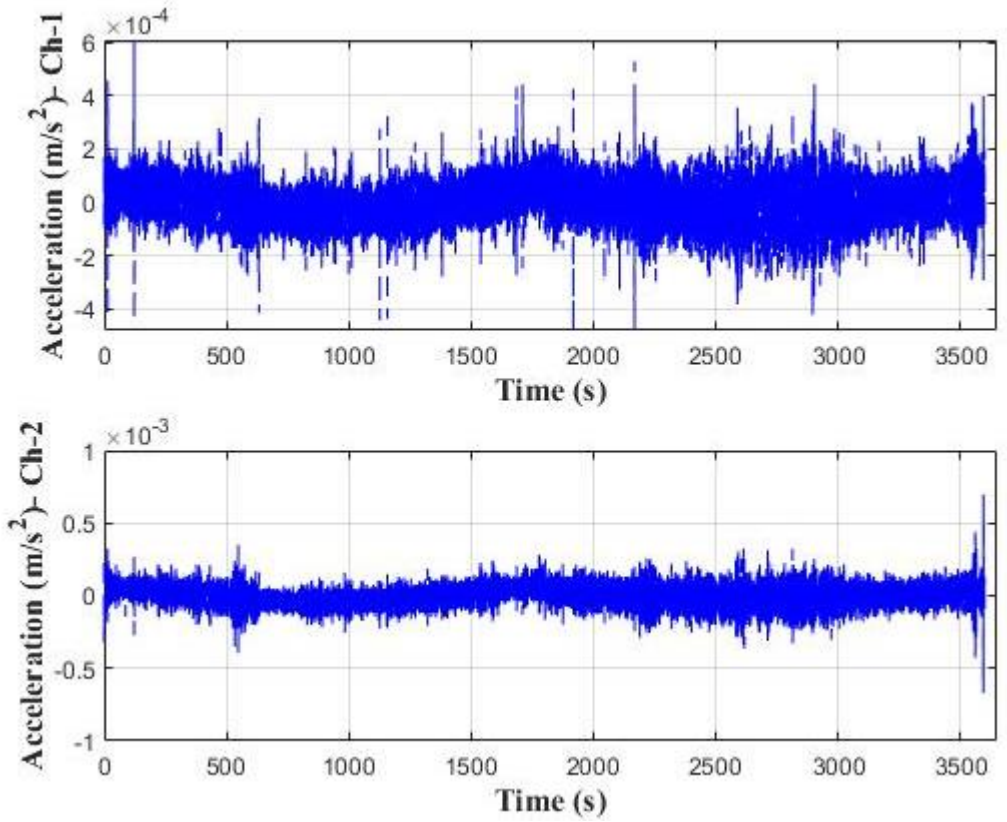

Figure B. 1 Ambient vibration recorded on first floor along channel 1 and 2.

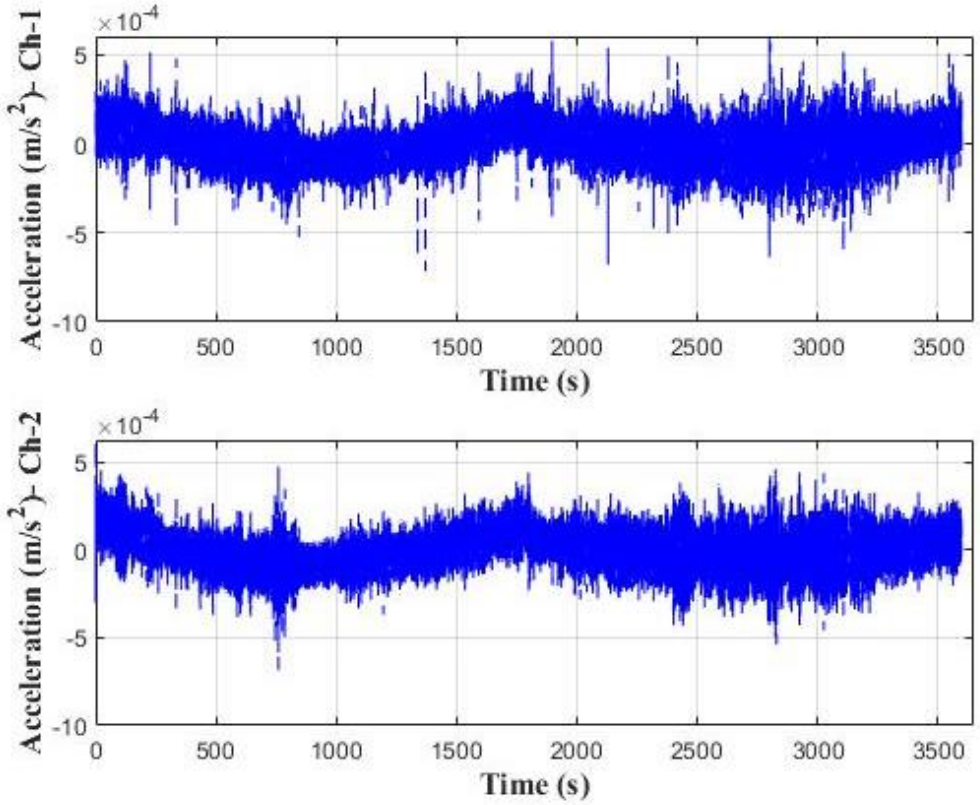

Figure B. 2 Ambient vibration recorded on second floor along channel 1 and 2.

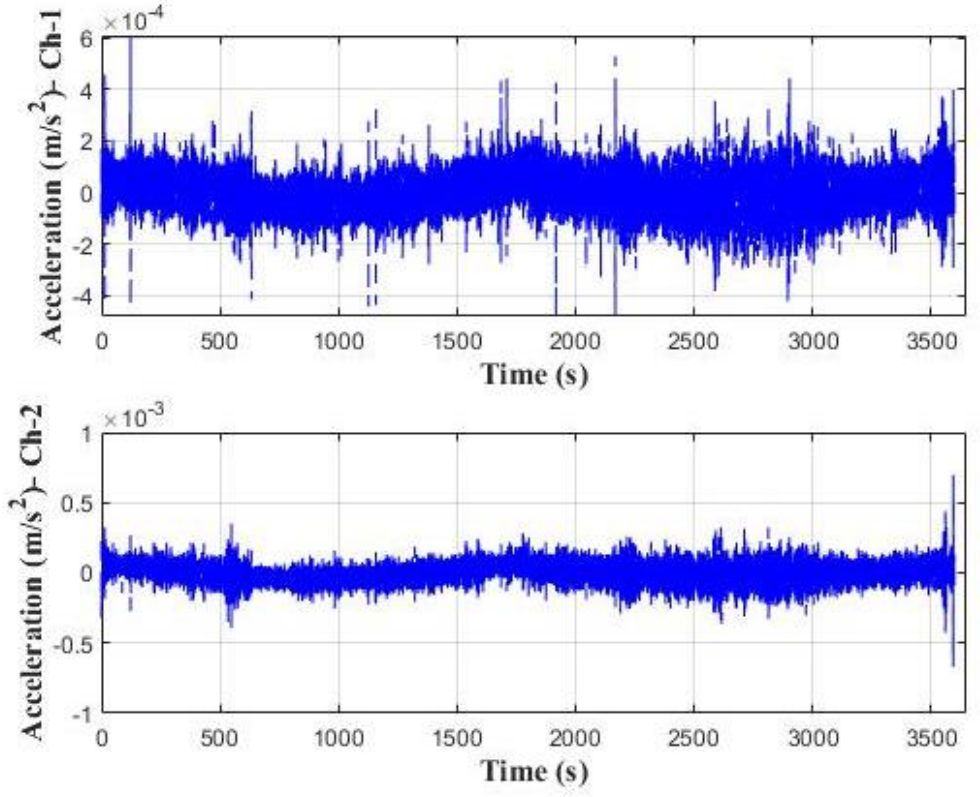

Figure B. 3 Ambient vibration recorded on third floor along channel 1 and 2.

Appendix C: Strong ground motion records

Acceleration time history of ground motion recorded for 25 April Gorkha earthquake at five different stations mentioned on chapter 6 are included here.

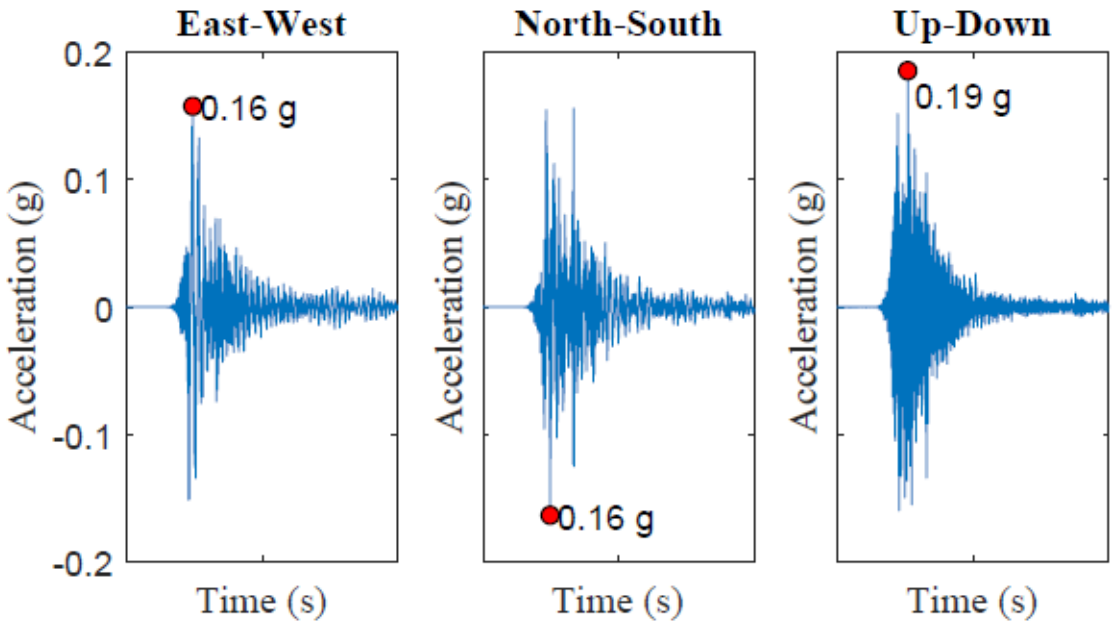

Figure C. 1 Acceleration time histories of mainshock ground motion recorded at KATNP station for 25 April Gorkha Earthquake. Red circle with text on each figure shows PGA.

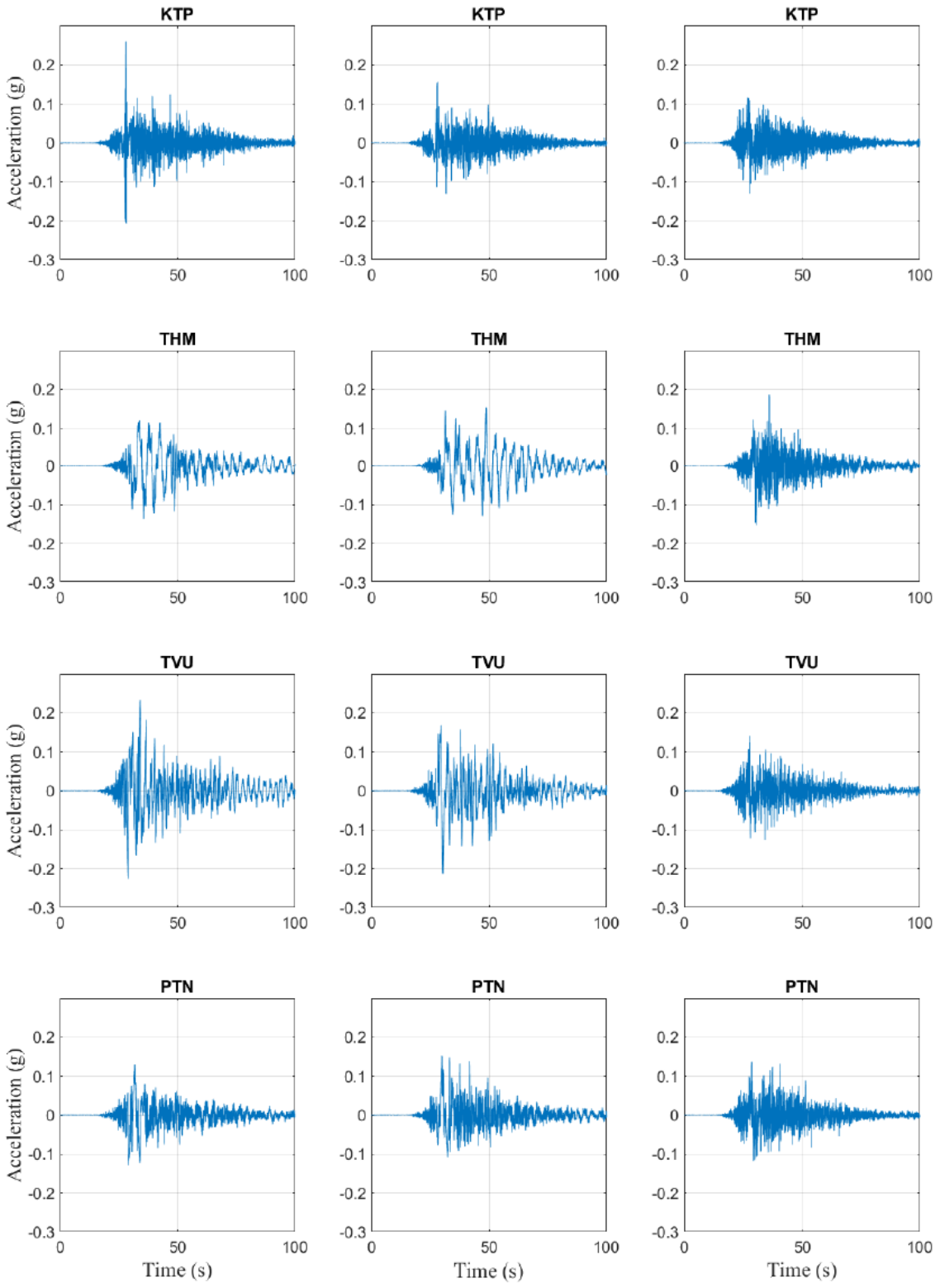

Figure C. 2 Acceleration time histories of mainshock ground motion recorded at five different stations KTP, THM, TVU and PTN for 25 April Gorkha Earthquake. Four figures on first column represents ground acceleration on East-west direction at each station respectively. Similarly, figures on second columns and third columns represents ground acceleration on north-south and vertical directions respectively.